Polymer Stabilized Magnetite Nanoparticles and Poly(propylene oxide) Modified Styrene-Dimethacrylate Networks

Linda A. Harris

Dissertation Submitted to the Faculty of the Virginia Polytechnic Institute and State University in partial fulfillment of the requirements for the degree of

DOCTOR of PHILOSOPHY

in

CHEMISTRY

Approved by:

Judy S. Riffle, Chair

John G. Dillard

John J. Lesko

James E. McGrath

Thomas C. Ward

April 19, 2002
Blacksburg, Virginia

Keywords: magnetite, nanoparticles, superparamagnetic, poly(ethylene oxide), carboxylic acid, ferrofluid, colloidal dispersion, structural adhesive, vinyl ester, poly(propylene oxide) dimethacrylate, network

Copyright 2002, Harris

Polymer Stabilized Magnetite Nanoparticles

Linda A. Harris

(ABSTRACT)

Magnetic nanoparticles that display high saturation magnetization and high magnetic susceptibility are of great interest for medical applications. Nanomagnetite is particularly desirable because it displays strong ferrimagnetic behavior, and is less sensitive to oxidation than magnetic transition metals such as cobalt, iron, and nickel. For *in-vivo* applications, it is important that well-defined organic coatings surround the nanomagnetite particles. It is rationalized that this will prevent any aggregation of the nanoparticles *in-vivo*, and may also enable efficient excretion and protection of the body from toxicity.

Magnetite nanoparticles can be prepared by co-precipitating iron (II) and iron (III) chloride salts in the presence of ammonium hydroxide at pH 9-10. Oleic acid is known to effectively stabilize dispersions of nanomagnetite in nonpolar solvent. Stabilization occurs because the carboxylic acid group covalently reacts with the surface of the magnetite and the aliphatic chain extends out into the nonpolar solvent, preventing aggregation of the particles by a steric (entropic) mechanism. One goal of this work has been to develop a generalized methodology for stabilizing nanomagnetite dispersions using well-defined, non-toxic, block copolymers, so that the resultant magnetite-polymer complexes can be used in a range of biomedical materials. My objectives have included: (1) Understanding what types of polymer structures bind irreversibly to

magnetite at the physiological pH and what block lengths are desirable, (2) Tailoring polymer block lengths to maximize the concentration of bound magnetite, yet preserve good dispersion and (3) Designing copolymers with both hydrophilic and hydrophobic tail blocks to enable dispersion in different types of carrier fluids.

Hydrophilic triblock copolymers with controlled concentrations of pendent carboxylic acids were designed as steric stabilizers for magnetite nanoparticles. The triblock copolymers contain carboxylic acids in the central anchor block and controlled molecular weight poly(ethylene oxide) tail blocks. They were utilized to prepare hydrophilic-coated iron oxide nanoparticles with biocompatible materials for magnetic field guidable drug delivery vehicles. The triblock copolymers synthesized contain 3, 5, or 10 carboxylic acids in the central segments with M_n values of 2000, 5000 or 15000 g/mol poly(ethylene oxide) tail blocks. A method was developed for preparing ≈10 nm diameter magnetite surfaces stabilized with the triblock polymers. The carboxylic acid is proposed to covalently bind to the surface of the magnetite and form stable dispersions at neutral pH. Stable dispersions were prepared with all triblock copolymers investigated. The polymer-nanomagnetite conjugates described in this thesis have a maximum of 35 wt. % magnetite and the nano-magnetite particles have an excellent saturation magnetization of ~66 - 78 emu/g Fe_3O_4. Magnetization curves show minimal hysteresis. Powder X-ray diffraction (XRD) confirms the magnetite crystal structure, which appears to be approximately single crystalline structures via electron diffraction spectroscopy analysis (EDS). These materials form stable magnetic dispersions in both water and organic solvents. Transmission electron microscopy (TEM) photomicrographs show that the dispersions contain ≈ 10 nm diameter magnetite coated with the polymeric coatings.

Poly(propylene oxide) Modified Styrene-Dimethacrylate Networks

Linda A. Harris

(ABSTRACT)

A series of terminally dimethacrylated poly(propylene oxide) oligomers/styrene/ dimethacrylate oligomer resins have been prepared and cured. These modified "vinyl ester" systems may be ideal for coatings, toughened matrix resins for fiber reinforced composites, bridge deck wear surface resins and structural adhesive applications, partially because lower styrene contents were possible, which alleviates environmental concerns with currents systems. In contrast, the resins were cured either at 25 °C followed by a postcure at 100 °C or cured at 150 °C with free radical initiators. The two methods produced networks with extremely different phase morphologies, which was interpreted as being due to a lower critical solution transition behavior (LCST). The resins cured at elevated temperatures were observed to phase separate either prior to, or during early stages of cure. The 25 °C cured (postcure 100 °C for 1 hr) network remained single phase, and achieved a significant conversion of the styrene and methacrylate units, as monitored by FT-IR and swelling experiments, which indicated high gel fractions. The single phase networks showed higher fracture toughness then the resins cured at elevated temperature. Adhesive strengths measured of both types of networks to aluminum, steel, and a vinyl ester/E-glass composite were measured by lap shear analyses. It could be demonstrated that adhesives with the appropriate initial viscosities exhibited good structural strength on all of these substrates.

Acknowledgements

First and foremost I would like to thank my principal research advisor, **Dr. Judy Riffle**. Judy Riffle's mentorship provided me with the perfect balance of research independence and support. Her belief me and my unconventional decision to switch research projects at the end of my third year of graduate school provided incentive to achieve goals I would not have imaged possible. I will continue to look to her as a role model regardless of my geographical location (which is literally the other side of the world). In addition, it was an honor to have **Dr. John Dillard, Dr. Jack Lesko, Dr. James McGrath** and **Dr. Thomas Ward** serve on my committee.

My graduate education here at Virginia Tech was enriched by the accessibility of research faculty and instrumentation available through collaboration with different departments including: **Dr. G. Wilkes** and **Dr. R. Davis** (Dept. of Chemical Engineering); **Dr. D. Dillard** (Dept. of Engineering Science and Mechanics); **Dr. R. Claus** (Dept. of Electrical and Computer Engineering) and **Dr. Zelazny** and **Dr. Eick** (Dept. of Soil Science). I also appreciate the faculty and graduate students in the Dept. of Chemistry for always taking time for technical discussions and sharing materials when necessary (i.e. middle of the night and the stockroom's closed), particularly the **Deck** and **McGrath research groups**.

The staff at Virginia Tech are excellent at making everything function smoothly and are irreplaceable. **Tom Glass** was a significant contributor to my research. His NMR expertise is an incredible asset to the entire department of chemistry. I also thank **Steve McCartney** for years of microscopy service and training. The administrative assistants (**Millie Ryan, Ester Brann, Laurie Good** and **Angie Flynn**) were always friendly and help with conference attendance details and funding management. I especially would like to thank Angie Flynn. Her

knowledge and skills are superb from designing websites, helping prepare and submit proposals, to organizing parties.

A special thanks goes to my undergraduate research assistant, **Jonathan Goff**, for his dedication to the project, careful work and for allowing me the opportunity to be a mentor to an excellent upcoming scientist. Moreover, I would also like to thank all of the lab mates in the **Riffle group** for friendship, support and helping create a cooperative research environment. Exciting research interactions were developed and maintained working with **Dr. Ellen Burts, Mike Zalich and Metha Rutnakornpituk** together on different components of the same research or similar projects**.** Moreover, it was my great pleasure to serve for several years as social coordinator with **Dr. Maggie Bobbitt Bump** organizing "extracurricular" activities for the Riffle group. I would also like to thank the girls (**Jen Hoyt, Dr. Sheng Lin-Gibson, Kristen Wilson, Astrid Rosario, Shauntrece Hardict, Dr. Maggie Bump** and **Amy Eichstadt**) that participated in Chick Night events. I will miss the margaritas, pumpkin carving (and painting) and movie-clip making nights. I also thank the **Materials Response Group** (MRG) for providing insight into the engineering world, which served to enhance my educational development. However, I did not appreciate the lesson, provided by **Dr. Tozer Bandorawalla,** on the viscoelastic response my head displays upon impact with a tabletop at Sharkey's.

I would also like to acknowledge all of friends that I have made prior to and during my years here at Virginia Tech who helped remind me that a full life requires a good balance between scientific discovery and friends, travel and life experiences. A few of these include (in the ~ order of meeting): **Jenny Halverson, Brenda Dunn, Adrienne Rice, Kyle Garcia, Dr. Hari Reddy, Dr. Celine Mahieux, Blair Russell, Shannon Proctor, Mark Meier, Minh-Chau**

Huynh, Dr. Nikhil Verghese, Dr. Tozer Bandorawalla, Dr. Rob Carter, Jolyn Senne, Dr. Marie-pierre Laborie, Dr. Balazs Zombori, Kai Dietze, John Bausano, Amy Gershoff, Sandrine Bresard, Sylvie Jamin, Dr. Alessandro Sannino and Dr. Luigi Ambrosio.

Finally and certainly not least, I would like to thank my family for their support of all my life choices and their love, which is a constant source of strength for everything I do. My parents, **Floyd** and **Carol**, have never limited my dreams. I thank my brother, **Dale**, for helping to begin my interest in science and discovery as children. My sister, **Suzanne (Harris) Maggard**, has and will always be a significant source of moral support. I enjoy our scientific discussions. My younger sister, **Laura**, your faith in me is cherished.

"There is a single light of science, and to brighten it anywhere is to brighten it everywhere."

- *Isaac Asimov*

Table of Contents

Abstract I: Polymer Stabilized Magnetite Nanoparticles……i

Abstract II: Rubber Modified Dimethacrylate Networks……iii

Acknowledgements……iv

List of Figures:……ix

List of Tables:……xi

Chapter 1: Introduction……1
1.1 Introduction to polymer stabilized magnetite nanoparticles**……**1
1.2 Dissertation overview**……**5

Chapter 2: Literature Review of Iron Oxide Magnetic Nanoparticle Systems……7
2.1 Introduction to magnetism……7
2.2 Theory of ferromagnetism and ferrimagnetism 12
2.3 Magnetic properties of small particles 17
2.4 Ferrofluids 25
2.4.1 Magnetic nanoparticles classifications 28
2.5 The iron oxides 29
2.5.1 Magnetite 31
2.6 Magnetite nanoparticle formation 34
2.6.1 Iron oxide nanoparticles formed in constrained environments 37
2.7 General aqueous coprecipitation of Fe^{2+} and Fe^{3+} salts 40
2.8 Magnetite formation parameters of coprecipitation method……..41
2.9 Magnetite nanoparticle stabilization 44
2.9.1 Steric or entropic repulsion 48
2.10 Steric stabilization methods and materials for iron oxide nanoparticles 50
2.11 Polymer composites: μm and submicron particle systems 65
2.12 Silica coating of iron oxide nanoparticles 68
2.13 Effect of COOH on iron oxide nanoparticle formation and magnetic properties 68
2.14 Characterization of magnetic nanoparticle systems 72
2.15 Magnetic nanoparticle applications 77
2.16 Magnetite toxicity 80

Chapter 3: Polymer Stabilized Magnetite Nanoparticles……82
3.1 Introduction 82
3.2 Experimental**……**..85
3.2.1 Materials**……**85
3.2.2 Synthesis of polymer precursor and carboxylic acid containing triblock polymer stabilizers**……**...86

3.2.3 Magnetite formation and steric stabilization……..88
3.2.4 Polymer precursor and triblock stabilizer characterization……89
3.2.5 Characterization of the polymer-stabilized magnetite……90
3.3 Results and discussion……91
3.4 Conclusions……...108

Chapter 4: Polymer Stabilized Magnetite Future Directions……...110
4.1 Conclusions and suggested future work……...110
4.2 Generalized stabilizer methods: Carboxylic acid containing triblock polymers……..111
4.3 Acknowledgements……...113

List of Abbreviations Part I:……114

References Part I:……..……...115

Chapter 5: Background to Rubber Modified Dimethacrylate Networks……121
5.1 Brief history of toughened thermosets……121
5.2 Rubber modified vinyl ester resins……..124

Chapter 6: Poly(propylene oxide) Modified Dimethacrylate Networks……..128
6.1 Introduction……..128
6.2 Experimental……131
6.2.1 Materials……131
6.2.2 Methods..... 135
6.3 Results and discussion……..137
6.4 Conclusions..... 156
6.5 Acknowledgements..... 157

List of Abbreviations Part II:……..121

References Part II:……159

Vita……...161

List of Figures

Figure 1. 1 New innovations in drug delivery systems using magnetic field directable microspheres. 3
Figure 1. 2 Oleic acid stabilization of magnetite nanoparticle surface 4
Figure 2. 1 Magnetic field lines in a bar magnet.....7
Figure 2. 2 The different types of magnetic behavior. 10
Figure 2. 3 Domain wall 14
Figure 2. 4 Magnetization versus applied magnetic field strength curve 16
Figure 2. 5 Coercivity as a function of particle size 18
Figure 2. 6 Domain structures observed in magnetic particles 19
Figure 2. 7 Linear dependence of the saturation magnetization on iron oxide nanoparticles size 23
Figure 2. 8 The inverse spinel crystalline structure of magnetite. 32
Figure 2. 9 Spin arrangements in magnetite and double exchange interaction. 32
Figure 2. 10 Transformation observed in iron oxides 33
Figure 2. 11 Size reduction of magnetite powders via ball mill grinding. 35
Figure 2. 12 Water-in-oil microemulsion method to form iron oxide nanoparticles. 38
Figure 2. 13 Magnetoferritin protein cage 40
Figure 2. 14 Magnetite output (α) versus time (τ) at 268, 283, 290, 307, 316 K. 44
Figure 2. 15 Surface charge density of magnetite particles versus pH of the media 45
Figure 2. 16 Thickness of adsorbed surfactant layers on two magnetic nanoparticles. 48
Figure 2. 17 Potential energy diagram for steric stabilization of nanoparticles. 49
Figure 2. 18 Schematic of dispersion states of (a) magnetite core in oil based (b) and water based (c) magnetic fluids. 50
Figure 2. 19 Carboxylic acid chemisorption on the surface of magnetite particle. 52
Figure 2. 20 Bilayer method depicting formation to achieve aqueous dispersions. 54
Figure 2. 21 α, ω-Dicarboxymethyl poly(oxyethylene) (DCPEG)..... 59
Figure 2. 22 Synthesis of a magnetic enzyme by coupling DCPEG-coated magnetite 61
Figure 2. 23 Triblock nanosphere template for maghemite formation 62
Figure 2. 24 Polymer template design and maghemite formation. 63
Figure 2. 25 Binding modes of carboxylates on the surface of magnetite. 72
Figure 2. 26 X-ray diffraction pattern of pure magnetite. 73
Figure 2. 27 Flow diagram of magnetic capture cell 78
Figure 3. 1 Controlled molecular weight triblock polymer stabilizers.....84
Figure 3. 2 Synthesis of hydrophilic carboxylic acid-containing triblock copolymers 92
Figure 3. 3 Reaction conversion monitored by the disappearance of NCO via FT-IR.....94
Figure 3. 4 Quantitative ^{13}C NMR used to assess the concentration of COOH 96
Figure 3. 5. The central segment of the stabilizer anchors to the magnetite surface 98
Figure 3. 6 XRD analysis of PEO-COOH-PEO coated Fe_3O_4 and neat polymer..... 102
Figure 3. 7 TEM of PEO-COOH-PEO polymer stabilized magnetite nanoparticles.....103
Figure 3. 8 Electron diffraction pattern of magnetite nanoparticles coated with polymer stabilizer via HRTEM 105
Figure 3. 9 Magnetization curve of a magnetite-triblock copolymer. 106

Figure 4. 1 Hydrophobic triblock polymer stabilizer containing carboxylic acid central segments and poly(propylene oxide) tail blocks. 112
Figure 4. 2 ^{13}C NMR spectrum of PPO-COOH-PPO triblock polymer stabilizer 113
Figure 5. 1 Transmission electron microphotograph of rubber modified epoxy……121
Figure 5. 2 Carboxyl terminated butadiene-acrylonitrile rubber copolymer 122
Figure 5. 3 Toughening of epoxy resins with a reactive thermoplastic polysulfone 123
Figure 6. 1 Rubber modified dimethacrylate network formation……...130
Figure 6. 2 Components for room temperature network formation 133
Figure 6. 3 High temperature cure of rubber modified dimethacrylates 134
Figure 6. 4 Methacrylate termination of poly(propylene oxide) 138
Figure 6. 5 Room temperature conversion monitored via FT-IR with a 100 °C postcure 141
Figure 6. 6 Swelling index of an unmodified network and rubber modified networks. 143
Figure 6. 7 TEM images of rubber modified networks 146
Figure 6. 8 Cloud point analysis of rubber modified resin via optical microscopy 147
Figure 6. 9 Phase separation of rubber modified resin as a function of time indicating spinodal decomposition via small angle light scattering. 149
Figure 6. 10 Fracture toughness of networks by 3-point bend 150
Figure 6. 11 Fracture toughness results of rubber modified networks 152
Figure 6. 12 SEM imaging the fracture surface of the 3 point bend samples 153
Figure 6. 13 Lap shear strength of resins bonded aluminum-to-aluminum, steel-to-steel and composite-to-composite structures 155

List of Tables

Table 2. 1 Magnetic units and conversions. 9
Table 2. 2 Estimated maximum single-domain size for spherical particles. 18
Table 2. 3 Magnetic data for transition metals and metal oxides. 28
Table 2. 4 Iron oxyhydroxide and iron oxide species. 29
Table 2. 5 Physical properties of magnetite and maghemite 30
Table 2. 6 Effect of chain length of a series of fatty acids on the formation of water dispersible magnetite solutions 53
Table 2. 7 Some magnetite nanoparticle characterization techniques. 76
Table 3. 1 Chemical compositions and theoretical M_ns of carboxylate containing triblock copolymer stabilizers. 87
Table 3. 2 Concentration of carboxylic acids/chain by ^{13}C NMR and titration……95
Table 3. 3 Theoretical mean square end-to-end distance of PEO tail block segments…..…101
Table 3. 4 Magnetic properties of nanomagnetite stabilized with poly(ethylene oxide) containing triblock stabilizers. 107
Table 5. 1 Fracture toughness values of some vinyl ester materials……...125
Table 6. 1 Chemical composition of series of resin mixtures…….132
Table 6. 2 Complex viscosities of resin mixtures at expected application temperatures. 139
Table 6. 3 Gel fractions of rubber modified vinyl ester networks 144
Table 6. 4 T_g values determined by DMA for rubber modified vinyl ester networks 145

Chapter 1: Introduction

1.1 Introduction to polymer stabilized magnetite nanoparticles

Nano-scale magnetic structures offer great potential for advancements in electronics, optio-electronics, magnetic storage, and biomedical applications. Currently, there is a great desire to prepare well-defined, discrete magnetic nanoparticles for both fundamental and societal benefit. These nano-sized magnetic materials display properties that differ from their respective bulk material counterparts. Size and surface effects dominate the magnetic behavior of nanomagnetic particles. The details of the relationships between shape, surface structure, composition and the resulting magnetic properties of magnetic nanoparticles are currently unclear. A major hurdle to understanding the relationship between structure and magnetic behavior is the availability of magnetic nanoparticles with well-defined structural features.

Current research in the area of magnetic nanoparticles is focusing on applications were their unique properties will allow for significant advances in scientific technology. In the electronics field researchers are investigating the design of superstructures comprised of magnetic ordered arrays to enhance sensitivity in magnetic sensors [1]. The concept of tailoring the sheath thickness of magnetic nanoparticles to control the interparticle interactions is currently studied to attempt to prevent defects in layered magnetic films and enable packing efficiencies leading to both high magnetizations and high susceptibilities [2]. Additionally, scientists are interested in creating well-defined superstructures, which could surpass the current electronics technology in magnetic storage and overcome the currently observed superparamagnetic limit [1, 2].

Furthermore, magnetic nanoparticles that display high saturation magnetization values and magnetic susceptibility are of great interest in biotechnology. Nanoscale magnetic particles prepared with surface stabilizers constitute magnetic fluids, also known as ferrofluids. These magnetic fluids display superparamagnetic properties. The significance of these materials is that they are single domain particles with discrete randomly oriented magnetic moments. When placed in an external magnetic field their moments rapidly rotate into the direction of the magnetic field and enhance the magnetic flux. When the external magnetic field is removed Brownian motion is sufficient to cause the moments and particles themselves to randomize and have no magnetic remanence [3]. The benefit of such materials is that they could be designed with biocompatible surface stabilizers for new biomedical applications which include retinal detachment therapy [4, 5], cell separation methods [6, 7], tumor hyperthermia [8], improved MRI diagnostic contrast agents [9-12] and as magnetic field-guided carriers for localizing drugs or radioactive therapies [13-15].

The goal of this research is to design hydrophilic, carboxylic acid containing polymers to serve as biocompatible, water dispersible steric stabilizers for magnetite nanoparticles. It will be desirable for these polymers to covalently bind to the surface of the magnetite nanoparticles and create a stable dispersion at neutral pH. The research described herein is just one component of a synergistic effort to create magnetic field directable drug delivery vehicles for interarterial transport to a tumor or cancer site using an external magnetic guidance system (Figure 1.1).

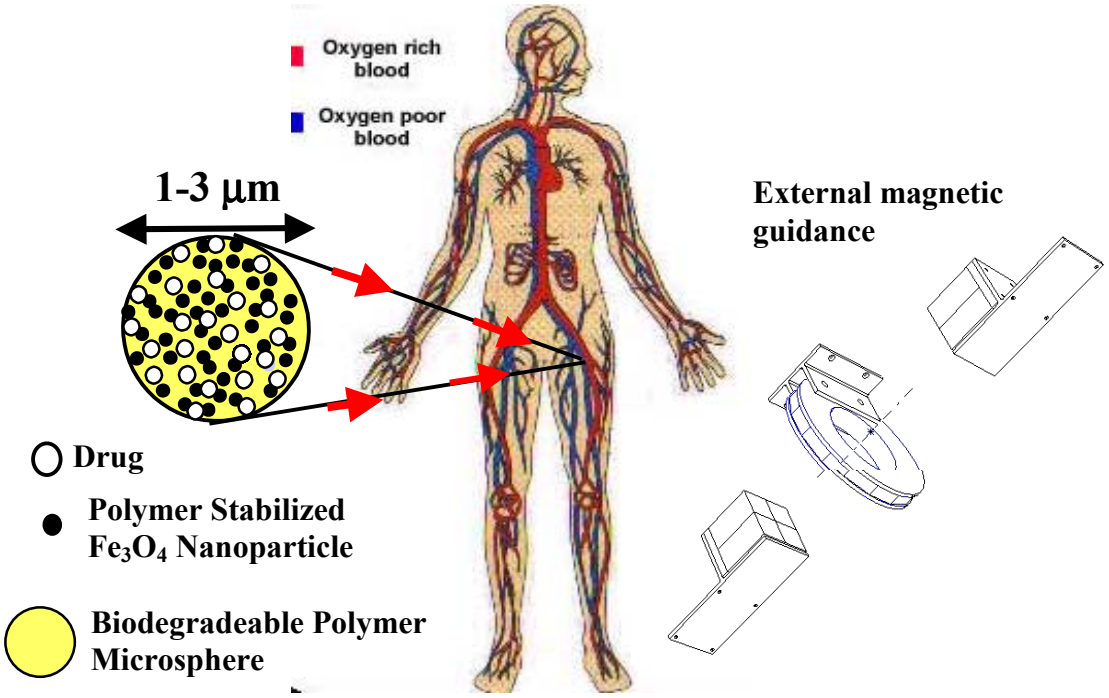

Figure 1. 1 New innovations in drug delivery systems using magnetic field directable microspheres to target drug at cancer or tumor site.

Advancements in these areas may lead to the ability to magnetically delivery higher concentrations of drugs to a tumor located in a region, which is not easily accessible. These technologies could reduce the extreme side effects that occur with systemic cancer therapies. The nanosize of the magnetic particles is sufficiently small to minimize toxicity [16]. In these biomedical endeavors, the organic component's structure is important since it will isolate the nanoparticles from biological tissues and will also ensure dispersion stability in aqueous

biological fluids. Both of these aspects may be key to minimizing long-term toxicity of magnetic particles as delivery vehicles. Thus, this research has focused on the creation of biocompatible surface stabilization of nanoscale magnetic particles with high magnetic susceptibility. The success of this research and its milestones has been attributable to the interdisciplinary collaborations between organic polymer chemists, inorganic chemists and physicists and may lead to great intellectual and societal advancements.

Magnetite nanoparticles were investigated for this application because they are less sensitive to oxidation than nanoparticles of transition metals and display the desirable magnetic properties. The steric stabilizers synthesized contain functional groups capable of binding covalently to the surface of the magnetite nanoparticle and to create stable, biocompatible, irreversibly bound sheaths at the physiological pH. Carboxylic acid groups to bind covalently to the surface of iron oxides. Oleic acid, a C_{18} fatty acid, is one example of a surfactant that covalently binds to the surface of iron oxides and creates magnetic dispersion in nonpolar hydrocarbon solvents (Figure 1.2).

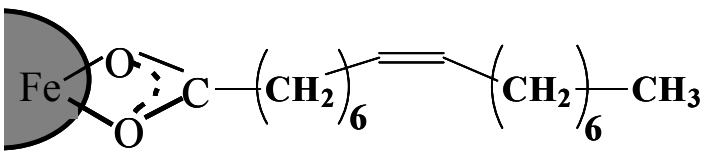

Figure 1. 2 Oleic acid stabilization of magnetite nanoparticle surface [17].

The approach was to model the stabilization achieved with oleic acid in a polymeric system and create surface stabilized iron oxide nanoparticle colloidal dispersions in aqueous media. The concept adopted in this research was to prepare a hydrophilic polymer with controlled amounts of carboxyl groups in the central urethane segments of poly(ethylene oxide) triblock polymers The carboxylic acids are coupled into the polymer via urethane chemistry using isophorone diisocyanate and 1,3-bis(hydroxymethyl) propionic acid (DMPA). Isophorone diisocyanate was chosen because any potential hydrolysis of this species would lead to aliphatic amines, which are less toxic and less reactive than an aromatic amine. The poly(ethylene oxide) may be ideal as the steric stabilizing tail blocks because it is biocompatible; hydrolytically stable; well-known to resist protein adsorption; M_n below 50k g/mol are capable of being eliminated [18]. They are also easy to prepare and functionalize. Magnetite nanoparticles were prepared by aqueous coprecipitation of hydrated di- and trivalent iron chloride salts in the presence of a strong base.

1.2 Dissertation overview

The second chapter is a review of the fundamentals of magnetism and a description of the magnetic behavior observed in nanoparticles. It focuses on iron oxide nanoparticles that display ferrimagnetism, a magnetic behavior of interest in systems for external guidance using an applied magnetic field. It includes the fundamentals of magnetism, magnetism of small particles, classification of magnetic nanoparticles, stabilization of nanomagnetic particles, a detailed review of magnetite, steric stabilization of magnetite and a discussion of applications and the characterization of such materials.

Chapter three describes the research approach taken in the design of hydrophilic polymers as steric stabilizers for magnetite nanoparticles; magnetite formation; and the subsequent

stabilization of these materials. Characterization of the polymers and the stabilized magnetite nanoparticles is also provided in terms of concentration of carboxylic acids/chain, crystalline structure of magnetite, dispersion quality, dispersion stability at neutral pH, iron content and magnetic properties.

The fourth chapter presents a summary of the results of this research, the current work underway and the future directions to be taken. This section also includes a discussion regarding the design of different carboxylic acid containing triblock polymer stabilizers for magnetite surface stabilization by the generalized synthetic approach described herein.

Chapter five begins the second part of the dissertation regarding the toughening of dimethacrylate networks with dimethacrylate terminated poly(propylene oxide) oliogomers. This chapter is an introduction to the rubber toughening of network systems. It provides a brief description of methods developments by other to toughen networks with a focus on vinyl ester systems.

The sixth chapter presents the research approach taken to increase the toughness of cured styrene-dimethacrylate resins. These materials were designed as structural adhesives for civil infrastructure applications. The complex viscosity of the resins was investigated. The resins were cured by two different cure methods. The resulting cured networks were characterized in terms of dynamic mechanical analysis, solvent resistance, fracture toughness and adhesive strength.

Chapter 2: Literature Review of Iron Oxide Magnetic Nanoparticle Systems

An understanding of the magnetic behavior of nanoparticles needs to begin with the fundamentals of magnetism. These foundations will allow an in-depth appreciation of the unique behavior of magnetic nanoparticles and their deviations from respective bulk properties.

2.1 Introduction to magnetism

Magnetism originates from the movement of electric charges. All materials display some magnetic response, however most effects are very small. The electrons in an atom govern magnetic properties of matter in two different ways. The first is the electron acting as a spinning charged sphere, where the spin resembles the magnetic field of a tiny bar magnet. The spin is a quantum mechanical property and can be oriented in one of two directions, in the "up" (↑) direction or the "down" (↓) direction [19]. The second is the effect of the electron circulating around the nucleus of the atom, which resembles a current loop [19]. The flow of charge in a circular current loop produces magnetic lines of force known as a dipole [20]. In a bar magnet the magnetic force lines flow around the dipole from north to south as depicted in Figure 2.1.

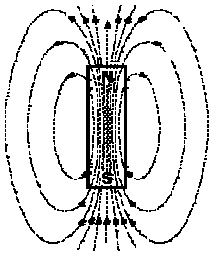

Figure 2. 1 Magnetic field lines in a bar magnet [21].

The magnetic moment of a material is the measure of the strength of the dipole. An electron in an atom has a magnetic moment due to its spin or spin and orbital motion.

An orbiting electron's response to an applied magnetic field is governed by the spin configuration of the material. The orbital motions of electrons create atomic current loops, which generate the magnetic field. Therefore, all materials inherently possess magnetic fields generated by the orbital motions of their electrons.

Magnetization terms

The quantities of magnetism are defined by fundamental concepts of magnetic dipoles consisting of equal and opposite moments. Free currents generate fields classified in terms of magnetic field strength or intensity (H) [22]. The magnetic induction (B) of a material is a function of H and the magnetization or polarization (M) (Equation 2.1).

$$B = H + 4\pi M \tag{2.1}$$

The magnetization (M) can be understood as the density of net magnetic dipole moments (μ) in a material (Equation 2.2).

$$M = \frac{\mu_{total}}{V} \tag{2.2}$$

The 4π factor in Equation 2.1 originates from the unit field created by a unit polar on the surface of a sphere of 1 cm radius, which encloses the pole with a surface area of 4π cm^2 [23, 24].

The magnetic susceptibility (κ) is a measure of the effectiveness of an applied magnetic field for inducing a magnetic dipole in the material. Magnetic permeability (μ) is a ratio of the magnetic induction and magnetic field strength (Equation 2.3).

$$\kappa = \frac{M}{H} \qquad \mu = \frac{B}{H} \qquad (2.3)$$

If a material does not respond to an applied magnetic field the magnetic permeability is simply the magnetic permeability of space (μ_0), where $\mu_0 = 4\pi \times 10^{-7}$ Tesla-m/A [19].

Magnetic units

Magnetism measurements were first defined in the cgs (centimeters, grams, seconds) or Gaussian system. The cgs system is used for fundamental and primarily theoretical discussions.

Table 2. 1 Magnetic units and conversions [23].

Quantity	Symbol	cgs unit	SI-1 unit	cgs equiv.	SI-2 Unit	cgs equiv.	SI-3 Unit	cgs equiv.
Field strength	H	Oe G Emu	A/m	$4\pi 10^{-3}$Oe	A/m	$4\pi 10^{-3}$Oe	T	10^4 Oe
Induction = total flux density	B	G Emu	T	10^4 G	T	10^4 G	T	10^4 G
Magnetization $= \frac{dipole\ moment}{volume}$ Magnetization = flux density due to the material	I J M 4πI M	emu/cm^3 emu G $\uparrow 4\pi$ G	T T	$10^4/4\pi$ G 10^4 G	kA/m	1 G	kA/m	1 G
Mass-magnetization	σ I M	G cm^3/g emu/g emu cm^3/g emu	Wb m/kg	$10^7/4\pi$ emu/g	A m^2/kg	1 emu/g	A m^2/kg	1 emu/g
(Dipole) moment	M	G cm^3 erg/Oe emu	Wb m	$10^{10}/4\pi$ G cm^3	A m^2	1 kG cm^3	A m^2	1 kG cm^3
Basic Equation		B = H +4πI B = H + M	B = μ_0H + M		B = μ_0(H + M)		B = H + μ_0M	

In the cgs system magnetization (M) is reported in electromagnetic units per volume (emu/cm^3) or mass (emu/g), magnetic field strength (H) is measured in Oersted (Oe) and permeability of vacuum is given the value of unity [25]. More recently, three different versions of the SI (Systems International) units were introduced (units of tesla and amperemeters [22, 23]. Unfortunately, the vast range of reporting options has resulted in inconsistencies in the literature and subsequent confusion. Therefore, a unit conversion table is indispensable (Table 2.1) [23].

Magnetism in materials

Materials are classified by their response to an externally applied magnetic field. Descriptions of orientations of the magnetic moments in a material help to identify different forms of magnetism observed in nature (Figure 2.2). Five basic types of magnetism can be described: diamagnetism, paramagnetism, ferromagnetism, antiferromagnetism and ferrimagnetism.

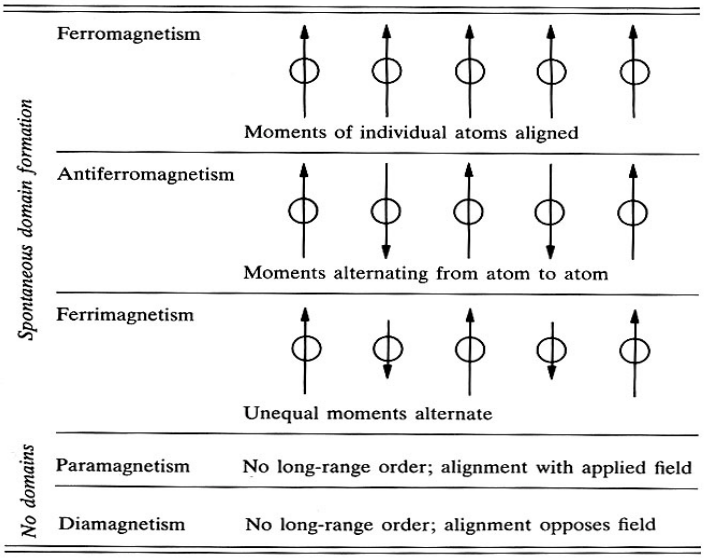

Figure 2. 2 The different types of magnetic behavior [3].

In the presence of an externally applied magnetic field the atomic current loops created by the orbital motion of electrons respond to oppose the applied field. All materials display this type of weak repulsion to a magnetic field known as *diamagnetism*. However, diamagnetism is very weak and therefore any other form of magnetic behavior that a material may possess usually over-powers the effects of the current loops. In terms of electronic configurations of materials, diamagnetism is observed in materials with filled electronic sub-shells where the magnetic moments are paired and overall cancel each other. Diamagnetic materials have a negative susceptibility ($\chi < 0$) and weakly repel an applied magnetic field. The effect of these atomic current loops are overcome if the material displays a net magnetic moment or has long-range ordering of magnetic moments [21].

All of the other types of magnetic behavior observed in materials are at least partially attributed to unpaired electrons in atomic shells, often in the 3d or 4f shells of each atom. Materials whose atomic magnetic moments are uncoupled display *paramagnetism.* Therefore, paramagnetic materials' moments have no long-range order. A generalized description of paramagnetism is when each atom carries a magnetic moment, which partially aligns in an applied magnetic field and hence enhances the magnetic flux density. The field acts independently on each atomic dipole. Hence, there is no long-range order and there is a small positive magnetic susceptibility ($\chi \approx 0$) [24]. Materials that possess f*erromagnetism* have aligned atomic magnetic moments of equal magnitude and their crystalline structure allows for direct coupling interactions between the moments which may strongly enhance the flux density. Furthermore, the aligned moments in ferromagnetic materials can confer a spontaneous

magnetization in the absence of an applied magnetic field Materials that retain permanent magnetization in the absence of an applied field are known as hard magnets.

Materials having atomic magnetic moments of equal magnitude arranged in a antiparallel fashion display *antiferromagnetism*. The exchange interaction couples the moments such that they are antiparallel hence leaving a zero net magnetization [22]. Above the **Néel temperature** (T_N) thermal energy is sufficient to cause the equal and oppositely aligned atomic moments to randomly fluctuate leading to a disappearance of their long-range order. In this state the material exhibits paramagnetic behavior. *Ferrimagnetism* is similar to antiferromagnetism in that two different sub-lattices exist and antiferromagnetic exchange interactions occur. However, the magnitudes of the two different types of moments, arranged antiparallel, are not equal in magnitude and hence a net magnetization is produced.

2.2 Theory of ferromagnetism and ferrimagnetism

A complete discussion of the theory of ferromagnetism is beyond the scope of this introduction. However, the fundamentals will be provided to address the magnetization processes in ferrimagnetic nanoparticles and their dispersions. Weiss first developed the molecular theory of ferromagnetism in the early 1900s, which sufficed as a semi-quantitative description. The theory is based on the assumption that each atomic dipole is subject to a local field that is proportional to the magnetization summed over all the other dipoles in the material [20-22, 25].

Later, the development of quantum mechanics led to the concept of exchange interactions between two atoms and spin-dependent Coulombic interactions. The spin exchange interaction is derived from the Pauli exclusion principle, where antiparallel spin arrangements in an atomic

shell are forbidden [26]. The exchange interaction is essentially the difference in Coulombic energies for different spin configurations in a sample [25]. Above a certain temperature, known as the **Curie temperature** (T_C), the alignment of the moments in ferromagnetic and ferrimagnetic materials is lost due to thermal energy and the material displays paramagnetic behavior.

Ferrimagnetism is similar to antiferromagnetism since the spin arrangements are antiparallel; however the sub-lattice magnetic moments are of unequal magnitude and therefore produce a net magnetization in an applied field. The net magnetization observed in ferrimagnetic materials is typically lower than that of ferromagnetic materials primarily because of the antiparallel spin arrangement in the former. Despite the differences in moment alignments, the theories that describe ferromagnetism can be applied to ferrimagnetism with modifications to account for the existence of the sub-lattice interactions and antiparallel orientations of spins.

The ferrimagnetic crystalline structure is comprised of two different magnetic ions occupying two kinds of lattice sites, tetrahedral (A) and octahedral (B) [20, 25, 27]. For spinel crystalline structures, such as magnetite, surprisingly all of the exchange interactions (AA, AB and BB) favor antiparallel alignment. The ferrimagnetic behavior is due to the strong AB interaction. The favorable A antiparallel B interaction induces all of the A spins to parallel arrangements and all of the B spins parallel with each other [20]. More detail of the ferrimagnetic behavior of magnetite nanoparticles will be provided in Section 2.5.1.

Some ferromagnetic and ferrimagnetic materials possess spontaneous magnetization and are referred to as permanent magnets. However, most ferromagnetic and ferrimagnetic materials are unmagnetized until an external magnetic field is applied. In the early 1900s, Weiss developed

the theory of magnetic domains to explain the lack of large demagnetization forces, which result if the entire ferromagnetic material is uniformly magnetized throughout [3].

Magnetic domains

The aligned spin arrangements in ferromagnetic, antiferromagnetic and ferrimagnetic materials are subdivided into regions (domains) throughout the bulk material. Weiss proposed that the driving force for formation of magnetic domains is to minimize the field energy of a magnetized material. The balance of the energy necessary to form a domain wall and the energy conserved by the existence of domains defines the lower limit of a domain size and therefore domain formation is a finite process. The size of a domain is approximately 0.05 to 0.5 μm and is dependent on the intrinsic properties of each material [28]. The boundary between two neighboring domains is a domain wall, which consists of a rotation of the direction of the magnetic moment between discrete domains (Figure 2.3) [20].

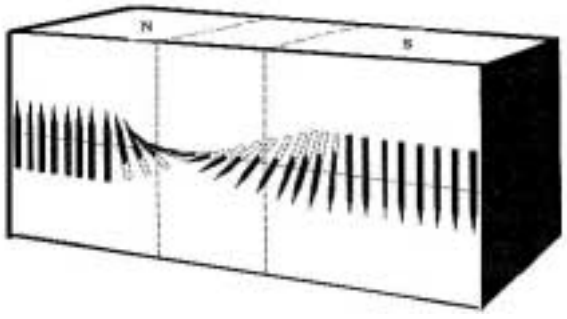

Figure 2. 3 Domain wall [20].

The visual conception of domain wall rotation shown in Figure 2.3 suggests a smooth gradual rotation of the vector moment between domains in the absence of an applied magnetic field, the unmagnetized state.

Hysteresis

In an unmagnetized ferromagnetic or ferrimagnetic material the collections of parallel spins in a domain are randomly oriented throughout the material and therefore collectively self-cancel resulting in a minimal to zero net magnetization (Figure 2.4 at M = 0). When placed in the presence of a sufficiently large external magnetic field, the spins in each domain rotate parallel to the direction of the applied magnetic field until all the dipoles are aligned. The plateau region of the magnetization curve is the saturation magnetization (M_s) (Figure 2.4). M_s is a measure of the magnetization (M) per gram basis and is given by

$$M_S = \frac{M}{\rho} \qquad \left(\frac{emu}{g}\right), \tag{2.4}$$

where ρ is the density of the material (Equation 2.4). The smooth curve in Figure 2.4, which depicts the rotation of the vector moment in the domain wall as the magnetic field strength (H) is varied, actually occurs in very small jumps and is referred to as the Barkhausen effect [22].

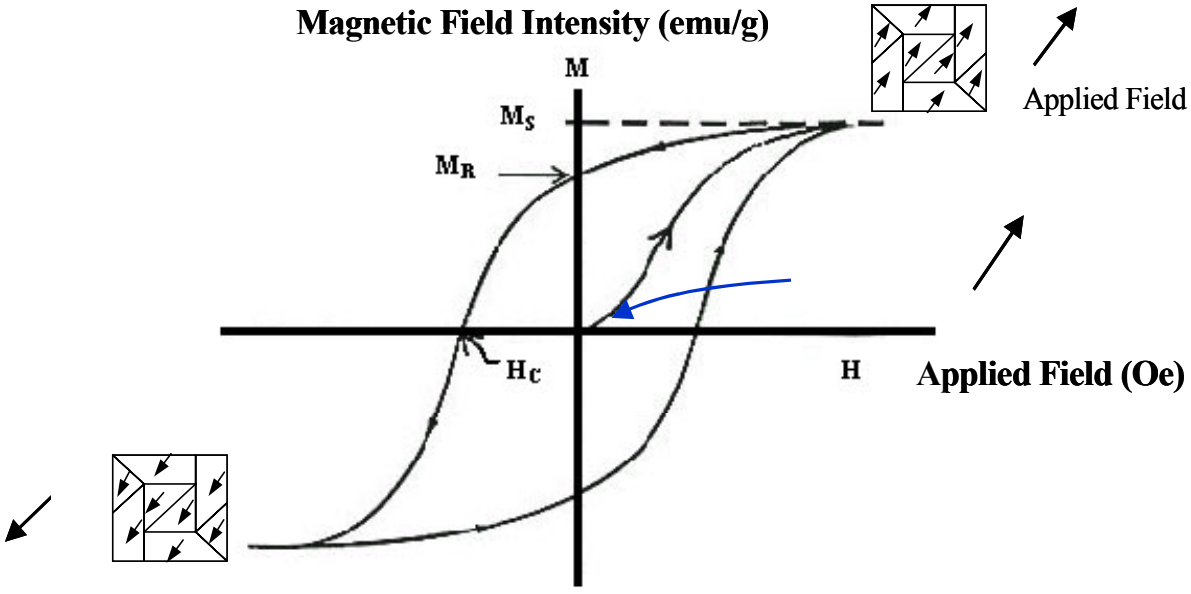

Figure 2. 4 Magnetization (M) versus magnetic field strength (H) where M_s is the saturation magnetization (M_R) is the remanence magnetization, and H_C is the coercivity.

When the applied field is decreased magnetization decreases. In multi-domain bulk materials, demagnetization occurs primarily via spin rotation through the domain walls [20, 25, 29]. If the demagnetization curve, during the removal of the applied field, does not follow the initial magnetization curve, the material displays hysteresis, which is the lag observed in Figure 2.4. Remanence magnetization (M_r) is the magnetization remaining at zero applied field (H = 0, Figure 2.4). The magnetic field applied in the negative direction required to return the magnetization to zero is the coercive force (H_c) [29].

Magnetic anisotropy

A dependence on the direction of measured magnetization was experimentally observed, which indicates the existence of magnetic anisotropy. The energy associated with the alignment of spins is described in its simplest form as a uniaxial system (Equation 2.5) defined by

$$E_a = K \sin^2 \theta \tag{2.5}$$

where K is the magnetic anisotropy energy constant and θ is the angle between M_S and the easy axis [22]. The easy axis of a crystalline specimen is the preferred direction of the total magnetization of the dipoles of a given material [22].

Magnetocrystalline anisotropy is derived from spin-orbit coupling, which is an intrinsic property dependent on the crystallographic orientation of the sample and is independent of particle shape [29]. The magnetic susceptibility is greatest when the saturation magnetization is induced along the easy axis of a material. Shape anisotropy is the effect of the induced magnetization on the physical shape of the specimen and is a significant factor for nonspherical materials [22].

2.3 Magnetic properties of small particles

Single domain particles

The width of a domain wall is a function of the magnetocrystalline anisotropy, the exchange energy and lattice spacing of the crystal structure. The domain wall is approximately a few hundred angstroms thick [22, 30, 31]. As the particle size decreases, the number of magnetic domains per particle decreases down to the limit where it is energetically unfavorable for a domain wall to exist [32, 33].

Table 2. 2 Estimated maximum single-domain size for spherical particles [22, 29, 35].

Material	D_S (nm)
Fe	14
Co	70
Ni	55
Fe_3O_4	128
γ- Fe_2O_3	166

In 1930 Frenkel and Dorfman first formulated theorizes regarding the single domain nature of particles below a critical diameter in 1930 [34]. In this critical size range the nanoparticles are single domain materials (Table 2.2). In the presence of an applied magnetic field, the spin's orientation and subsequent magnetic saturation is achieved with lower field strengths than with the analogous bulk materials. The magnetic moment of each particle is ~10^5 times larger than for transition metal ions and saturation magnetization is reached at applied magnetic fields as low as 1 kOe [36]. When the field is decreased, demagnetization is dependent on coherent rotation of the spins, which results in large coercive forces [29]. The large coercive force in single domain particles is due to magnetocrystalline and shape anisotropies for nonspherical particles. The coercive force is also dependent on particle size as shown in Figure 2.5.

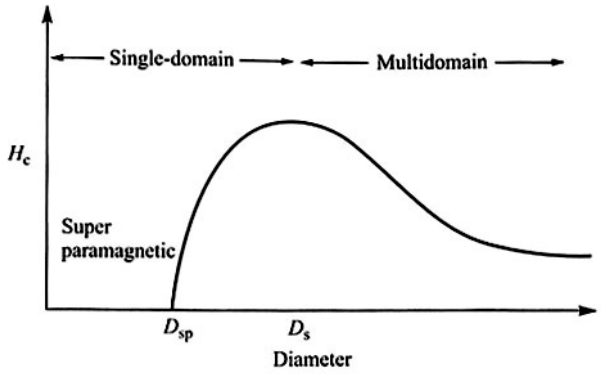

Figure 2. 5 Coercivity as a function of particle sized (D_{sp} is the superparamagnetic size and D_s is the single domain particle size) [22].

As particles the size of these single domain particles decreases, the coercive force decreases. Moreover, the shape anisotropy increases as the aspect ratio of a particle increases. Therefore, elongated single-domain particles (Figure 2.6b) can display large coercive forces [32, 33].

Superparamagnetism

The magnetic anisotropy, which keeps a particle magnetized in specific direction, is generally proportional to the volume of a particle [37]. As the size of the particle decreases, the energy associated with the uniaxial anisotropy (K) decreases until thermal energy is sufficient to overcome any preferential orientation of the moment in the particle. A single domain particle that reaches magnetization equilibrium at experimental temperatures in short times relative to the measurement time is commonly referred to as superparamagnetic. (Figure 2.6a) [32].

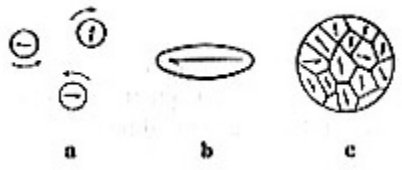

Figure 2. 6 Domain structures observed in magnetic particles: a) superparamagnetic; b) single domain particle; c) multi-domain particle [32].

Magnetic relaxations observed in superparamagnetic particles

When placed in an external magnetic field the magnetic moments of these particles align in the direction of the field via moment and particle rotation. When the field is removed the frequency of thermally activated reversals is given by (Equation 2.6)

$$f = f_0 \, e^{-E/kT} \tag{2.6}$$

where f_0 is the "attempt frequency" which is approximately 10^9 s^{-1}. Conceptually, the frequency is the rate at which the particles approach thermal equilibrium [38]. For relaxation times of ~100 seconds the critical energy barrier is

$$\Delta E_{crit} = \ln(t f_0) kT \; = \; 25\, kT \tag{2.7}$$

for thermal equilibrations (Equation 2.7). The condition for superparamagnetism is observed when a particle with uniaxial anisotropy displays zero coercive force as mathematically defined (Equation 2.8) by

$$KV \; = \; 25\, kT \tag{2.8}$$

where K is the effective magnetic anisotropy energy constant (a function of the magnetocrystalline, shape and surface anisotropies from Equation 2.5), V is the volume of the particle and kT is the thermal energy [22, 38].

Particles with relaxation times greater than 100 seconds or with diameters larger than the critical values (Table 2.2) are called blocked [20, 22, 39]. The **blocking temperature** (T_B) of a material is given by Equation 2.9.

$$T_B = \frac{KV}{25k} \tag{2.9}$$

Below T_B the anisotropy of the particle blocks the free movement of the moment [22]. Above the T_B the moment is free to align in an applied magnetic field and appears superparamagnetic.

In an applied field at temperature T, assuming the particles' moments have achieved some level of thermal equilibrium, there will be a Boltzmann distribution of moments aligned in the direction of the applied field. This relation is essentially the case prescribed for classical paramagnetism, where the degree of orientation is given by the Langevin function (Equation 2.10)

$$m_{av} = m(\coth \alpha - \frac{1}{\alpha}) \qquad where \qquad \alpha = \frac{mH}{kT} \ , \tag{2.10}$$

where m_{av} is the average magnetic moment, k is Boltzmann's constant and T is the absolute temperature [32]. The fundamental difference is that in the paramagnetic case the moment is a single atom, whereas now the moment considered is a single domain particle, which contains more than 10^5 atoms coupled ferro- or ferrimagnetically [40]. The term superparamagnetism originates from this relation. The magnetization of an individual superparamagnetic particle is given by $M = nm_{av}$, where n is the number of particles per volume.

The defining factor between single domain and superparamagnetic particles is essentially the relaxation time relative to the experimental time. The superparamagnetic nature of the nanoparticles is derived from the randomization of aligned spins governed by Brownian motion and Néel rotation when the gradient field is removed. Brownian motion and Néel rotation are magnetic relaxation mechanisms due to particle and spin rotation, respectively. Brownian relaxation is achieved via bulk rotational diffusion of the particles in a fluid. The relaxation time for Brownian motion (Equation 2.11) is given by

$$\tau_B = \frac{3V'\eta}{kT}, \qquad (2.11)$$

where V′ is the hydrodynamic volume of the particle, η is the dynamic viscosity, k is Boltzmann's constant and T is the absolute temperature [39]. Néel relaxation (Equation 2.12) is attributed to the rotation of the magnetization vector or moment in the particle with a relaxation time given by

$$\tau_N = \tau_0 \exp\left(\frac{\Delta E}{kT}\right), \quad where \quad \Delta E = KV\left(1-h\right)^2, \qquad (2.12)$$

τ_0 is typically estimated to be 10^{-9} s, ΔE is the energy barrier assuming uniaxial noninteracting particles, $h = H/H_k$ is the reduced magnetic field and H_k is the internal magnetic field due to anisotropy [39]. Experimental conditions for superparamagnetism are 1) relaxation times faster than the measurement times (commonly ~100 s) [39], 2) the magnetization curve does not display hysteresis.

Dependence of particle size on magnetization

The magnetization of bulk materials is inherently larger than for nanoparticles of the respective materials. Experimental values for the saturation magnetization of magnetite nanoparticles have been reported in the range of 30 – 60 emu/g, whereas bulk magnetite can theoretically be as high as is 92 emu/g [41, 42]. Several researchers using a variety of techniques have investigated the causes for the observed reduction in magnetization in fine magnetic particles. The theories and experimental interpretations conflict and remain debatable. In the late 1960s Coey and Berkowitz state that the observed decrease in magnetization is due to the existence of noncollinear spins and high effective anisotropy fields in the surface and not magnetic "dead" layers [43, 44].

Morales *et al.* investigated the structural effect of magnetic properties on iron oxide nanoparticles formed by 1) coprecipitation of di- and trivalent iron salts with NH_4OH (S-NH); 2) coprecipitation with KOH in the presence of 1 wt. % PVA solution (S-OH); and 3) laser pyrolysis of $Fe(CO)_5$ and subsequent oxidation (Fe4) [45]. The researchers used powder XRD and TEM analyses to determine the size of the particles and measured the magnetic properties with a vibrating sample magnetometer. A plot of the saturation magnetization versus particle size (Figure 2.7) suggests a linear correlation. The deviation from the linear trend observed in the Fe4 particles is assumed to be due to their amorphous nature. The order-disorder characteristic of the particles' structure was investigated with XRD at 10° and 30° (2θ) and FT-IR. Results suggest particle surface defects and order-disorder structural characteristics both influence the magnetic properties [45].

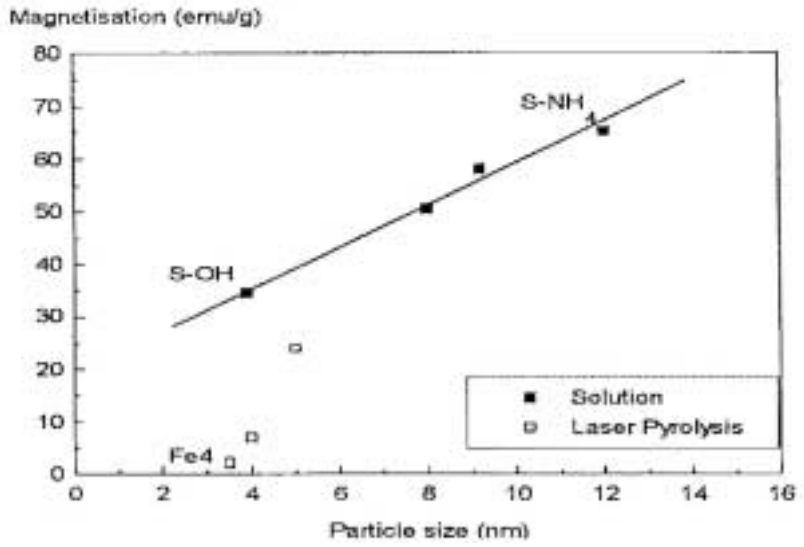

Figure 2. 7 Linear dependence of the saturation magnetization of iron oxide nanoparticles and size [45].

Saturation magnetization studies investigated by Mollard *et al.* also suggest a linear dependence of the magnetic response as a function of particle size or specific surface area [46]. These researchers propose that the observed losses are correlated to an electron transfers with O and OH atoms and possibly some oxidation of Fe^{+3} ions [46]. More recently, Kodama and Berkowitz propose that the surface spin disorder observed in spinel ferrimagnetic nanoparticles is due to broken exchange bonds at the surface [37].

Sato *et al*. suggest that the loss of magnetization as the particle decreases depends largely on the crystalline magnetic anisotropy energy constant, K. Smaller K constants display lower relative magnetization values [41]. Experimental analyses including microscopy, XRD and magnetometry studies suggest that the reduced magnetization is due to surface characteristics of nanoparticles. Specifically, the loss of magnetization may be due to the existence of a "magnetically dead layer" ~1 nm thick caused by an asymmetric environment effect of the surface atoms [41]. Finally, a spin canting surface effect was suggested by investigations using Mössbauer spectroscopy, which appeared to be enhanced as the particle size and temperature were decreased [47].

Popplewell and Sakhnini suggest that the particle size affects the physical and magnetic properties of ferrofluids in complex ways [42]. Experimental investigations using transmission electron microscopy (TEM), magnetic measurements and light scattering analyses indicate that there is a difference between physical and magnetic particle size. The researchers suggest the existence of a nonmagnetic surface layer or a surface anisotropy due to an adsorbed surfactant. The effect of the surfactant on the surface of iron oxide nanoparticles will be discussed in Section 2.13. Nevertheless, it seems that effects of particle size in the nano length scales are

complex and alter relaxation processes and interparticle interactions. The intrinsic nature of these effects makes it difficult to incorporate into generalized theories [42].

2.4 Ferrofluids

Superparamagnetic particles dispersed in a carrier fluid are referred to as ferrofluids. A stable ferrofluid consists of superparamagnetic nanoparticles, a carrier fluid and a surfactant. Ferrofluids are not found in nature and were first introduced in the early 1960s [3].

General theory of ferrofluid dispersion stabilization

Dispersion and the prevention of agglomeration is due to balancing three primary attractive forces: 1) magnetic attractive forces; 2) the gravitational force; and 3) London dispersion or van der Waals forces [3]. The attractive magnetic energy between two magnetic dipoles (U_A^{Mag}) is a function of the dipole moments $\mathbf{m}_1$ and $\mathbf{m}_2$ and the distance between the particles given by Equation 2.13

$$U_A^{Mag} = \frac{1}{4\pi\mu_o r^3} [\mathbf{m}_1 \cdot \mathbf{m}_2 - 3(\mathbf{m}_1 \cdot \mathbf{r}/r)(\mathbf{m}_2 \cdot \mathbf{r}/r)] \qquad (2.13)$$

where $\mathbf{r}$ is the vector between the centers of the two dipoles and μ_0 is the magnetic permeability of space [32]. The magnetic dipole of a single domain particle is described by $m = I_0 V$ where I_0 is the magnetization per unit volume of the particle and V is the volume of the particle. The interaction energy increases as the distance between particles decreases and aggregation may occur unless prevented by a surfactant. In addition, the magnetic dipoles of the particles attract in a magnetic field. When a concentrated magnetic fluid dispersion is placed in a gradient magnetic field, the particles and the fluid move together in the direction of the field [32]. The attraction energy of one of two point dipoles (Equation 2.14) is given by

$$E_d = -\frac{\pi M_S^2}{9\mu_0}\frac{d^3}{(l+2)^3} \qquad (2.14)$$

where M_S is the saturation magnetization and μ_0 is the magnetic permeability, l = 2s/d; s is the distance between the sphere surfaces and d is the diameter of the particles [48]. It is necessary that the particles be sufficiently small and superparamagnetic for the interaction energy of the particles to be overcome and to maintain colloidal stability. Importantly, the magnetic interaction of the system decreases when the particle are superparamagnetic because the thermal energy induces free rotation of the magnetic moments of the particles [32].

The gravitational force pulls the particles down while the Brownian motion works to keep them dispersed. The effect of the gravitational force (Equation 2.15) is given by the ratio of the gravitational energy to the attractive magnetic energy given by

$$\frac{Gravitational\ Energy}{Magnetic\ Energy} = \frac{\Delta\rho\, g\, L}{\mu_0\, M\, H} \qquad (2.15)$$

where $\Delta\rho$ is the difference in density of the solid and the liquid, L is the height of the container and g is the gravitational constant [3]. Using common values in Equation 2.15, Rosensweig determined that the gravitational impact on the nanoparticle stability of a typical ferrofluid is insignificant, indicative of a colloidal dispersion [3].

London dispersion or van der Waals attractive forces of the particles for one another are derived from the spontaneously induced polarizability of fluctuating electric dipole-dipole

forces, independent of magnetic attractive forces. The attractive forces also promote aggregation in an attempt to lower the large surface energy of the nanoparticles (> 100 dyn/cm) that arise from their large surface area to volume ratio [10]. The interfacial tension (γ) is the result of the large surface area of the nanoparticles leads to a negative contribution to the free energy of enthalpy of transformation given by $dG = \gamma dA$ [49]. The van der Waals attractive force describing dipole fluctuation energies for equal sized spheres is given by the Hamaker expression shown in Equation 2.16,

$$E_i = -\frac{A}{6}\left(\frac{2}{l^2+4l} + \frac{2}{(l+2)^2} + \ln\frac{l^2+4l}{(l+2)^2} \right) \qquad (2.16)$$

where A is the Hamaker constant (approximately 10^{-19} N·m for Fe, γ-Fe_2O_3 and Fe_3O_4) [3] ; l = 2s/d; s is the distance between the sphere surfaces and d is the diameter of the particle [48]. The interaction energy increases as the distance between particles decreases ($l \rightarrow 0$) and aggregation occurs. The attractive force decreases as the particles move away from one another proportional to l^{-6} [48]. The van der Waals attractive forces are a significant factor and must be countered with repulsive forces in order to prepare and maintain colloidal dispersions.

Electrostatic or steric repulsion forces are two mechanisms used to balance the attractive forces and prevent particle aggregation. In electrostatic stabilization the surface of the particle is made to carry a charge and the particles repel each other if their proximity goes below a certain distance. The electrostatic stabilization is a pH sensitive method and of limited use, especially in biomedical applications. The steric repulsion method is commonly achieved using long chain

surfactant molecules and will be described in detail in Section 2.9.1, where magnetite stabilization is reviewed.

Further in depth discussions of theory of magnetic fluids and colloidal dispersions will not be provided in this literature review. However, the interested reader will find more theory and detail in the following references for magnetic fluids [3, 26, 33, 36, 38, 48] and colloidal dispersions [50].

2.4.1 Magnetic nanoparticles classifications

Magnetic particles capable of forming superparamagnetic dispersions in a carrier fluid are comprised of metals and metal oxides with length scales from 1 to 100 nm. These metals and metal oxides include Ni, Co, Fe, Fe_3O_4 and γ-Fe_2O_3. The pure metals have the highest magnetic susceptibility (Table 2.3).

Table 2. 3 Magnetic data for transition metals and metal oxides [22, 36].

Substance	Saturation Magnetization (M_s) (emu/cm^{-3}) at 298K	Curie Temperature (K)
Ni	485	631
Co (cubic)	1400 – 1422	1404
Fe (cubic)	1700 – 1714	1043
γ-Fe_2O_3	394[26]	820 – 986
$FeO{\cdot}Fe_2O_3$	480 – 500	858
$MnO{\cdot}Fe_2O_3$	410	573
$CoO{\cdot}Fe_2O_3$	400	793
$NiO{\cdot}Fe_2O_3$	270	858
$CuO{\cdot}Fe_2O_3$	135	728

However, these transition metals are highly toxic and extremely sensitive to oxidation. Under atmospheric conditions Ni, Co and Fe oxidize to NiO, CoO and FeO alloys, which are antiferromagneitc. Presently, there are no synthetic and/or physical methods to prevent the oxidation mechanism, which is a significant problem for nanoparticles due to their large surface area. Currently researchers are investigating synthetic and physical methods to protect Co nanoparticles [5, 51, 52]. Therefore iron oxides, despite their initial lower magnetization, offer great potential as oxidatively stable nanomagnetic particles with diverse application possibilities in oxygen rich environments.

2.5 The iron oxides

Iron oxide exists in a variety of chemical compositions and with different magnetic properties (Figure 2.8 and Table 2.4). Materials of interest to magnetically guidable systems are iron oxides such as γ-Fe_2O_3, Fe_3O_4 and $MO{\cdot}Fe_2O_3$ (where M is Mn, Co, Ni, or Cu) because they display ferrimagnetism. As mentioned above ferrimagnetic iron oxides inherently display a lower magnetic response than ferromagnetic materials, such as the transition metals. However, the iron oxides are also less sensitive to oxidation and therefore maintain stable magnetic responses.

Table 2. 4 Iron oxyhydroxide and iron oxide species [27].

Mineral	Formula	Magnetic response
Goethite	α-FeOOH	antiferromagnetic
Akaganéite	β-FeOOH	antiferromagnetic
Lepidocrocite	γ-FeOOH	antiferromagnetic
Feroxyhyte	δ'-FeOOH	Ferrimagnetic
Ferrihydrite	$Fe_5HO_8{\cdot}4H_2O$	antiferromagnetic
Hematite	α- Fe_2O_3	weakly ferrimagnetic
Maghemite	γ- Fe_2O_3	Ferrimagnetic
Magnetite	Fe_3O_4	Ferrimagnetic

Magnetite (Fe_3O_4) and maghemite (γ-Fe_2O_3) are the most common and intensely researched iron oxides. The mixed metal $MO{\cdot}Fe_2O_3$ ferrites have varying physical and magnetic properties and are commonly developed for electronics applications due to particle shape and subsequent single domain nature. A significant amount of research has been reported regarding the mixed metal ($MO{\cdot}Fe_2O_3$) ferrites and the reader is referred to several excellent references for further information [53-57].

Magnetite and maghemite are similar in physical properties and crystalline structure (Table 2.5). Both display ferrimagnetism, however maghemite has lower saturation magnetization. The difference in their magnetic response is due to sub-lattice interactions. Maghemite is structurally γ-Fe_2O_3 which is comprised solely of Fe^{3+} ions. In the crystalline structure half of the Fe^{3+} ions are tetrahedrally coordinated and the other half are octahedrally coordinated. Magnetite is comprised of Fe^{2+} and Fe^{3+} ions in a 1:2 molar ratio, $FeO{\cdot}Fe_2O_3$, where half of the Fe^{3+} ions are tetrahedrally coordinated and the other half are octahedrally coordinated and all of the Fe^{2+} are octahedrally coordinated.

Table 2. 5 Physical properties of magnetite and maghemite [26, 27].

	Crystal system	**Cell dimensions (nm)**	**Density (g/cm^3)**	**Color**	**Magnetic susceptibility (emu/g)**	**Curie Temperature (K)**
magnetite	cubic	$a_0 = 0.839$	5.26	black	90[58] - 98[26]	850
maghemite	cubic or tetragonal	$a_0 = 0.834$	4.87	reddish-brown	76[58] - 81[26]	820 – 986

Their Curie temperatures (T_C) are sufficiently high so that both are applicable in a variety of magnetically responsive applications. However, maghemite's T_C is difficult to measure because it converts to hematite above 713K [27].

Since both iron oxide forms are ferrimagnetic and stabilized in carrier fluids by similar mechanisms, equal focus has been shown in literature. Specific procedures for the formation of magnetite and maghemite are different; however, in practice mixtures of the two are easily obtained if a high level of care is not taken experimentally. The sensitivity of reagent stoichiometry and a large number of other reaction parameters often complicate the ability to obtain pure magnetite crystalline structures. The focus of this review will be on magnetite formation. However, because the mechanisms of stabilization are similar, maghemite procedures are included when the relevance of the research is justified.

2.5.1 Magnetite

Magnetite crystal structure

Magnetite (Fe_3O_4) has an inverse spinel crystal structure with face centered cubic unit cell where oxygen ions are placed regularly in cubic close packed positions along the [111] axis [27]. Magnetite's oxygen ion array contains holes partially filled with ferric and ferrous ions [27, 59]. The unit cell is comprised of 56 atoms: 32 O^{2-} anions, 16 Fe^{3+} cations and 8 Fe^{2+} cations [24]. Magnetite's chemical formula is Fe_3O_4, however more appropriately it is defined as $FeO{\cdot}Fe_2O_3$. The inverse spinel structure is arranged such that half of the Fe^{3+} ions are tetrahedrally coordinated and the remaining half of Fe^{3+} and all of the Fe^{2+} are octahedrally coordinated (Figure 2.8).

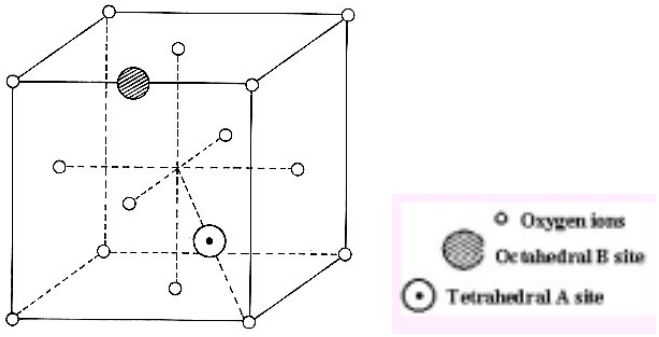

Figure 2. 8 The inverse spinel crystalline structure of magnetite [26].

Magnetic properties of magnetite

Magnetite's electronic configuration consists of unpaired 3d electrons, which impart net magnetic moments. The spins of the tetrahedrally (A) coordinated Fe^{3+} and the spins of the octahedrally (B) coordinated Fe^{3+} and Fe^{2+} are antiparallel and unequal in magnitude (Figure 2.9a) [20]. Below the Curie temperature (850K) these interpenetrating sublattices aligned antiparallel with unequal moments give rise to the observed ferrimagnetism [27]. The spin arrangements of the two interpenetrating sublattices of the octahedrally coordinated Fe^{2+} and Fe^{3+} "are coupled ferromagnetically via a double-exchange mechanism associated with inter-ion electron transfer" (Figure 2.9b) [25, 60].

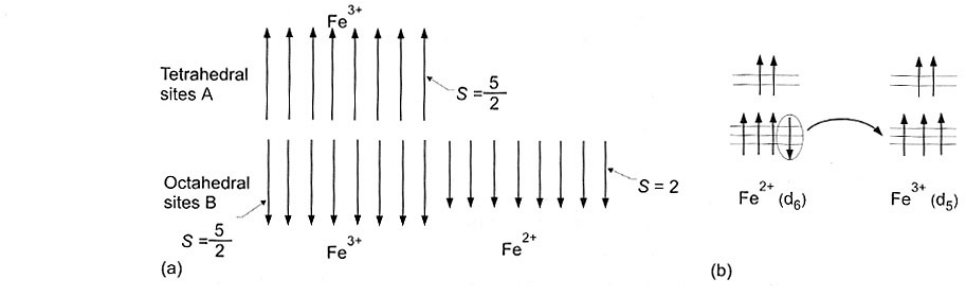

Figure 2. 9 Spin arrangements in magnetite, $FeO{\cdot}Fe_2O_3$, and the double exchange interaction with inter-ion electron transfer [25].

The easy axis of magnetite is the cube edge. The crystalline magnetic anisotropy constant (K) for magnetite is 1.4 x 10^5 erg/cm^3 and the superparamagnetic maximum critical particle size estimated from KV ~25kT is ~25 nm, which is lower than the single domain critical size in Table 2.2 [41].

Magnetite Stability and Transformations

Magnetite readily oxidizes in air to maghemite (Figure 2.11 and Equation 2.17). Importantly, maghemite is ferrimagnetic with only slightly reduced magnetic response. However, at temperatures greater than 300°C magnetite oxidizes to hematite [27].

$$4\,Fe_3O_4 \;+\; O_2 \;\rightarrow\; 6\,Fe_2O_3 \qquad (2.17)$$

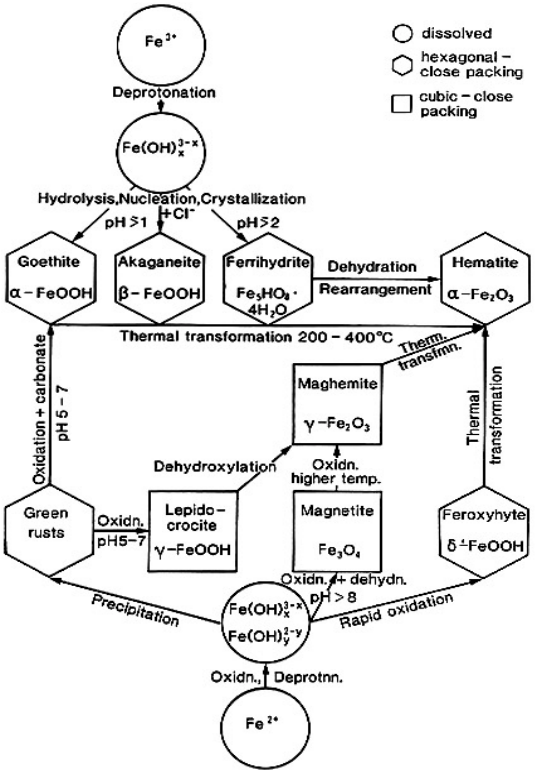

Figure 2. 10 Transformation observed in iron oxides [61].

Hematite is antiferromagnetic, therefore this conversion may be an important consideration in certain applications. A review of magnetite transformation studies can be found in Cornell and Schwertmann's text (Figure 2.11) [27].

Surface chemistry of magnetite

When considering the properties and application of magnetic nanoparticles, the surface properties and chemistry are of great significance. The surface Fe atoms, which were not bound to oxygen atoms at the surface act as Lewis acids and therefore coordinate with molecules that donate lone pair electrons, Lewis bases. Therefore in aqueous systems the Fe atoms coordinate with water, which dissociates readily to leave the iron oxide surface hydroxyl functionalized. Surface hydroxyl groups are amphoteric and may therefore react with either acids or bases [61].

In aqueous dispersions the surface of magnetite will be either positive or negative, depending on the pH of the solution. The isoelectric point is the pH where the surface displays an equal number of negative and positive surface charges. The isoelectric point of magnetite is observed at a pH of 6.8 [61]. Stabilization of magnetite nanoparticles can be achieved by electrostatic double layer, steric stabilization or by modifying the isoelectric point with a citrate or silica coating [61]. The stabilization of the iron oxide nanoparticles is crucial to obtain magnetic colloidal ferrofluids stable against aggregation in an applied magnetic field. The methods of stabilizing iron oxide nanoparticles will be discussed in Section 2.10.

2.6 Magnetite nanoparticle formation

There are several different synthetic methods to form magnetite and maghemite nanoparticles. Procedures offered in literature may not be specific to magnetite and are often comprised of indiscernible mixtures of magnetite and maghemite. The different forms can be

determined by color or using electron diffraction spectroscopy (EDS) and X-ray diffraction spectroscopy (XRD) described in Section 2.17.

Synthetically, magnetite is formed by two fundamental processes: size reduction and aqueous precipitation. Aqueous precipitation methods for magnetite nanoparticle formation include: oxidation of Fe^{2+} [61-63]; formation in: water-in-oil microemulsions [64-68], vesicles [69], apoferritin [70-72]; liposomes [73, 74]; and in the presence of polymers [6, 11, 75-81]. However, the most common synthetic route to magnetite is the coprecipitation of hydrated divalent and trivalent iron salts in the presence of a strong base [36, 41, 53, 58, 82-87].

Size reduction process

Ball mill grinding μm sized magnetite powder was one of the first methods, developed by Papell in the late 1960s, to form ~10 nm in diameter particles [88]. The process, outlined in the flow chart in Figure 2.11 involves grinding in the presence of solvent and surfactant [3].

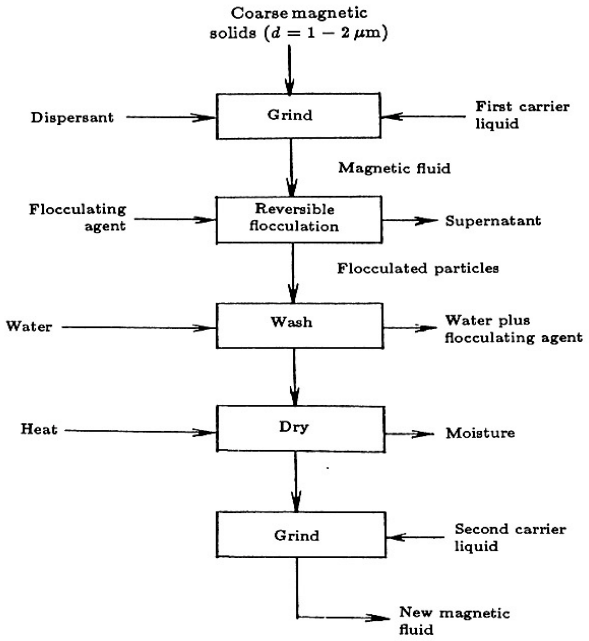

Figure 2. 11 Size reduction of magnetite powders via ball mill grinding [3].

Long grinding periods of 500 – 1000 hours are required to form the nanoparticles, and therefore this method has been essentially replaced by aqueous precipitation methods.

Oxidation of Fe^{2+}

Magnetite prepared by the oxidation of Fe^{2+} species forms through green rust stages at 300°C [61]. Another method for forming iron oxide nanoparticles at a lower temperature (90 – 100°C) utilizes Fe^{2+} iron salts such as $FeSO_4 \cdot 7H_2O$ and KNO_3 at pH 4.5 until the very end of the reagent addition where the pH is increased to 10 using a base (KOH) [72, 89]. Sugimoto and Matijevic suggest that the magnetite formation is achieved via crystallization of amorphous ferrous hydroxide [89]. Gardineer and Sambucetti suggest the oxidation of ferrous hydroxide to $Fe(OH)_3$ followed by thermal aging in the presence of an oxygen purge. During the aging the ferrous and ferric hydroxides react with one another to form Fe_3O_4 [90].

Douglas *et al*. tailored the oxidation method to investigate the effects of a carboxylate functionalized poly(amidoamine) dendrimers on the formation of maghemite. The reaction utilized a mild oxidizing agent, trimethylamine N-oxide, while maintaining a pH of 8.5 at 65°C [63]. The synthetic procedure they report leads to magneto-dendrimer carboxylate-stabilized maghemite nanoparticles. The researchers report that the ability to stabilize the magnetic nanoparticles is limited to a generation-4 carboxyl terminated dendrimer, other generations investigated failed to form stable dispersions. Moreover, the rate of reagent addition is a crucial reaction parameter in the oxidation of ferrous ions to magnetite or maghemite. A slow controlled process prevents the formation of pure Fe^{3+} phases, which may compete and limit the desired iron oxide formation [63, 91].

2.6.1 Iron oxide nanoparticles formed in constrained environments

The aqueous precipitation of hydrated iron ions in bulk solutions creates sphere-like nanoparticles of various sizes and is dependent on reaction conditions. Several attempts have been reported to form well-defined iron oxide nanoparticles of controlled size using synthetic and biological nanoreactors. The constrained environments include: amphoteric surfactants to create water swollen reversed micellar structures in nonpolar solvents [64-68, 92, 93]; apoferritin protein cages [70, 72, 94]; and phospholipid membranes that form vesicles the with iron oxide nanoparticles serving as solid supports [73, 95].

Water-in-oil microemulsions with ionic surfactants

Water-in-oil microemulsions are created using amphotertic surfactants. In nonpolar, hydrocarbon solvents the polar head group self-associates and forms micellar structures. The nonpolar tails extend out into the solvent creating a thermodynamically stable dispersion. With the appropriate surfactant chemical composition and concentration, these micellar cores serve as constrainted nanoreactor environments for the coprecipitation of aqueous iron salts. Literature reports the use of sodium bis(2-ethylhexylsulfosuccinate) (AOT) [64-66, 92, 93] or cetyltrimethyl-ammonium bromide (CTAB) [66] as ionic surfactants. The process for creating iron oxide nanoparticles in the nanoreactor is shown in Figure 2.12. Two solutions containing surfactant concentrations above their critical micelle concentration (cmc) are prepared in a nonpolar solvent such as heptane. It is important that all of the reaction mixtures be carefully deoxygenated prior to reaction to prevent the oxidation of the Fe^{2+} ion species [61].

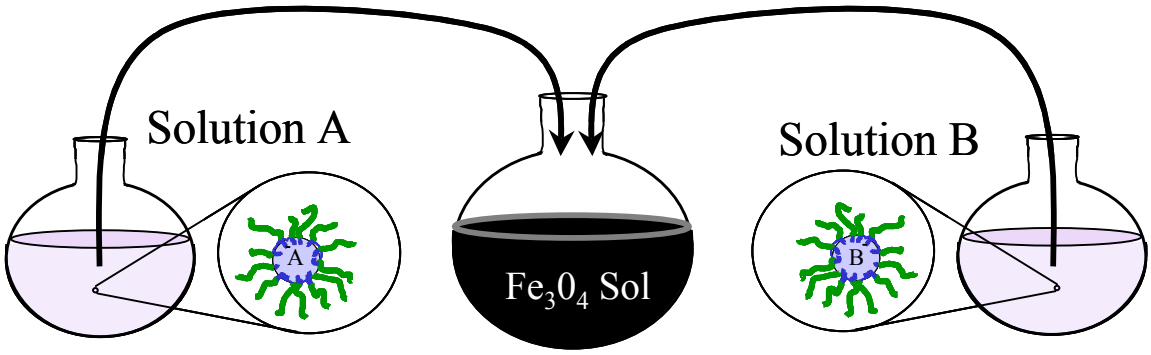

Figure 2. 12 Water-in-oil microemulsion method to form iron oxide nanoparticles in nonpolar solvents (solution A and solution B contains the Fe^{2+}/Fe^{3+} and NH_4OH aqueous inverse microemulsion, respectively).

Then, the aqueous iron salt mixture is added to one of the solutions and a strong base (NH_4OH) is added to the other flask in limited quantities so as to swell the micelles while maintaining a thermodynamically stable emulsion. The clear mixtures are combined and the contents of the inverse micelle cores mix forming the iron oxide nanoparticle.

The approach is novel, however the high concentration of surfactant necessary to create the water solubilized nanoreactor. Moreover, the ionic surfactants functional group in the hydrated core seems to limit the capability of forming highly crystalline magnetite nanoparticles. The presence of functional groups during the formation of magnetite and maghemite has been shown to inhibit crystal formation, as described in Section 2.13 [96, 97]. Furthermore, it is not yet clear how the compositions of the iron oxides and their crystal structures relate to the conditions used in these reactions.

Water-in-oil microemulsions with nonionic surfactants

A reverse micelle nanoreactor approach using nonionic surfactants avoids the complication of the presence of a complexing-functional species and offers great future potential [67, 68]. The

nonionic surfactants consist of hydroxyl terminated poly(ethylene glycol) hydrophilic segments with long hydrophobic hydrocarbon tails, such as Igepal CO-520 {polyoxyethylene(5)nonylphenyl ether, 4-$(C_9H_{19})C_6H_4(OCH_2CH_2)_nOH$, n~5} [67, 68]. These investigations provide fundamental insight into the future design of nanoparticles formed in reverse micelles; however, they appear to be limited by the constraints of commercially available materials and it is unclear how these hydrophobic coated, nonpolar solvent dispersible particles can be transferred into aqueous media for biomedical applications.

Magnetoferritin

A similar concept to the reverse micelle is the use of ferritin protein cages to form the ferrites inside a biological iron storage protein core ~8 nm in diameter [70, 72, 94]. Ferritin is a spherical polypeptide shell, which has an external diameter of ~12 nm with two internal subchannels and an inner chamber (Figure 2.13) [94].

The inner chamber of the protein cage contains ferrihydrite, an antiferromagnetic hydrated iron oxide. Ferrihydrite is removed by reductive dissolution in acidic media by dialysis to leave apoferritin, the empty protein cage. The researchers report the attainment of magnetite by stepwise additions of Fe^{2+} solutions followed by oxidation at 60°C. Modifications were made to optimize the magnetoferritin method by Wong *et al*. in 1998. These modifications include the use of stoichiometric oxidation of the Fe^{2+} using a mild, one electron oxidant in an anaerobic environment [72].

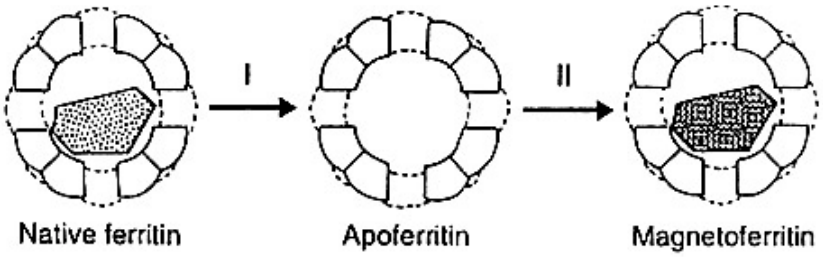

Figure 2. 13 Magnetoferritin protein cage [70].

Magnetoliposomes

Another biological nanoreactor method uses phospholipid membranes called liposomes to produce ~25 nm diameter iron oxide particles [73]. The resulting phospholipid stabilized iron oxide nanoparticles are referred to as magnetoliposomes. These magnetoliposome structures appear to mimic biological membranes and therefore may be of great use in biomedical applications, such as magnetically controllable bioreactors [95].

2.7 General aqueous coprecipitation of Fe^{2+} and Fe^{3+} salts

Mechanism and nature of formation

Magnetite formed by base induced aqueous condensation of hydrated Fe^{2+} and Fe^{3+} salts dates back to the early 1900s [82]. Despite its long history, the exact mechanism of formation is still not well understood. One general mechanistic theory proposes that the Fe^{2+} salt hydrolyzes to $Fe(OH)_2$ and reacts with hydrous oxides to form magnetite [91, 98]. Another perspective offered by Farley *et al*. suggests that the formation occurs via surface adsorption of cations, which leads to a balance between surface complexation reactions and precipitation [99].

Despite the ambiguity of the reactions between the hydrated ferrous and ferric ions, several researchers ascertain that the attainment of the cubic inverse spinel crystal structure is governed

by nucleation and crystal growth mechanisms [61, 86]. Nucleation of the ions in solution must be a discrete first step followed by crystal growth to obtain monodisperse particles [27]. The nucleation step depends on the formation of clusters of ions in solution at the point where the supersaturation of the ions exceeds a critical value. Experimental solution conditions govern the crystal growth step processes [61].

2.8 Magnetite formation parameters of coprecipitation the method

Purity of reagents

The purity of the reagents is an important synthetic parameter in the formation of magnetite. Divalent iron salt reagents reported in the literature for coprecipitation are commonly $FeCl_2 \cdot 4H_2O$ or $FeSO_4 \cdot 7H_2O$. The Fe^{2+} salts are oxidatively unstable [61]. In air they oxidize to akaganeite forms (β-FeOOH) as indicated by color change ($FeSO_4 \cdot 7H_2O$ develops an orange color). Trivalent iron salts may be either $Fe(NO_3)_3$ or $FeCl_3 \cdot 4H_2O$. The chlorinated Fe^{3+} salt is hydroscopic; however, some trivalent iron salts may dehydrate, which alters expected stoichiometries. Storing the reagents under nitrogen and careful deoxygenation of all solutions prior to use prevents these instabilities. Finally, when preparing magnetite by the coprecipitation method the dissolved di- and trivalent iron salts should be used immediately to prevent oxidation or side reactions [61].

Stoichiometric ratio and ionic strength

Magnetite's formula is $FeO \cdot Fe_2O_3$, therefore the reaction requires 1 mole Fe^{2+} and 2 moles of Fe^{3+} for stoichiometric conversion. The oxidative instability of the Fe^{2+} ion has lead some researchers to the use molar ratios of $Fe^{2+}/Fe^{3+} > 0.5$ [75, 100]. The Fe^{2+}/Fe^{3+} is predicted to average out to a stoichiometric reagent mixture, because the hydrated Fe^{2+} salt oxidizes to Fe^{3+}

species. However, with properly deoxygenated solutions, the use of initially stoichiometric molar quantities of the two iron salts is preferred for pure magnetite formation and achievable using careful experimental techniques.

Qui *et al*. investigated the dependence of the ionic strength of the reaction solution on the formation of magnetite. The magnetite prepared with the addition of 1.0 M NaCl aqueous solution created iron oxide nanopartices ~1.5 nm smaller than those formed without its presence. In addition, these smaller nanoparticles formed in the higher ionic strength solutions display lower saturation magnetization (63 emu/g) than those prepared in NaCl free solutions (71 emu/g) [58]. The decrease in magnetization was attributed to the decrease in size of the particle when prepared in the higher ionic strength media. Most of the reaction procedures found in literature do not alter the ionic strength of the reaction media and it is unclear if there is a significance to its use.

Concentration of hydrated iron salt solutions and order of addition

The concentrations of the iron salts used in the coprecipitation of magnetite vary widely in the literature. In laboratory scale preparations the order of addition follows where the base is introduced into the stirring mixed iron salt solution until magnetite is formed at a pH range of 9 – 14. However, in industrial scale procedures the order of addition is reversed and the aqueous iron salts are added to the base. Following the industrial method, Gribanov *et al*. showed that the magnetic response increased as the reagent molar concentration increased to a limit of ~0.1 M based on formed magnetite [86]. The researchers theorize that if the reagents are too concentrated, during magnetite formation, water is not able to participate in the hydrolysis and limits the di- and trivalent iron ion species mobility and hence their ability to polycondense via

the olation mechanism [86]. However, there are no reports investigating where the limiting concentration lies for proper mobility when the base is added to the iron salts. Also, the rate of base addition should be rapid (1 – 2 s) with intense agitation. A slow base addition creates inhomogeneous regions of the hydrated iron species, which leads to nonmagnetic iron compounds [86].

Nature of the cation of the base

The effect of the nature of the cation of hydroxide base used to form magnetite was investigated in terms of magnetic properties and crystal structures [86]. The saturation magnetization increased in order of the following base strengths: KOH > NaOH > LiOH > NH_4OH. X-ray analysis showed of nonmagnetic species when strong alkalines bases such as KOH and NaOH were used. Gribanov *et al.* used the Pourbaix diagrams and theory to suggest that the strong alkalie such as KOH and NaOH shift the pH of the mixture to pH ~14 which creates iron hydrate complexes that are incapable of forming magnetite. These researchers report that magnetite preparations using ammonium hydroxide in the pH range of 8.5 to 10 does not produce any of the nonmagnetic iron oxide forms [86].

Additionally, the effect of a variety of different NH_4OH base concentrations was investigated [12]. The researchers formed magnetite using a series of base concentrations from 0.25 to 2.0 M NH_4OH and suggest that there were no significant effects on the magnetic properties of the particles [12].

Effect of temperature

Several researchers report the use of an elevated reaction temperature and suggest its significance in obtaining the optimal crystal formation.

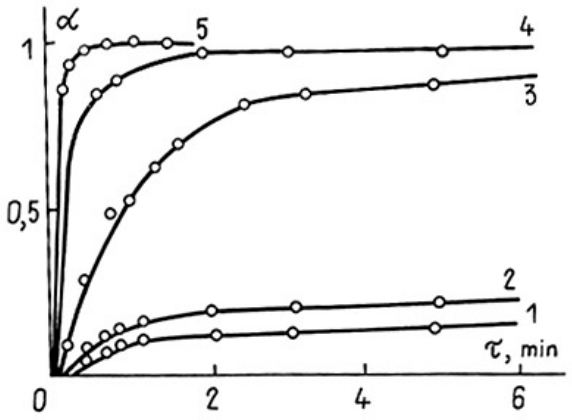

Figure 2. 14 Magnetite output (α) versus time of precipitation (τ) at 268, 283, 290, 307, 316K [86].

Formation kinetics investigated as a function of temperature suggests a time-temperature dependence of the rate of formation of magnetic species (Figure 2.14) [86]. The induction period for the formation of magnetic particles decreases with an increase in temperature. The investigations support the theory of nucleation and growth of the particles. Furthermore, the results indicate that the temperature of formation should not exceed 343K, where the quality of the particle is affected negatively [86].

2.9 Magnetite nanoparticle stabilization

Aggregation due to the attractive forces associated with magnetite nanoparticles are prevented by creating an electrostatic double layer, use of a surfactant functioning as a steric stabilizer, or by modifying the isoelectric point with a citrate or silica coating [61, 83]. Ionic surfactants prevent agglomeration due to the attractive forces described in Section 2.4 by creating repulsive forces originating from the proximity of like charged particles approaching one another.

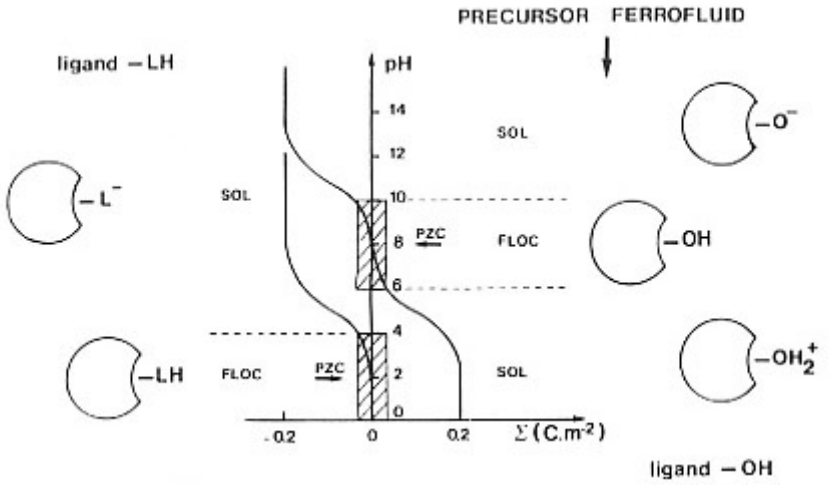

Figure 2. 15 Surface charge density of magnetite particles versus pH of the media [83].

Electrostatic stabilization is a pH sensitive method and of limited use, especially in biomedical applications where the pH is ~7. Therefore, the mechanism and methods of electrostatic stabilization will not be discussed in significant detail. Magnetite's isoelectric point is observed at a pH of 6.8 (Figure 2.15). Near the point of zero charge (PZC) the surface charge density (Σ) is zero and the interparticle electrostatic charge repulsions are not sufficient to keep the particles van der Waals attractive forces from causing flocculation (FLOC). Bare magnetite particles flocculate in the pH range of 6 – 10 as shown on the right side in Figure 2.15. The isoelectric point of magnetite can be shifted to pH 2 using either citrate ligand or a silica coating, thus above pH of 4 the coated magnetite particles are peptizable as shown on the left in Figure 2.15 [83].

Functional groups known to bind to the surface of magnetite include: phosphates, sulfates and carboxylates [27]. The sulfate binding mechanism investigated via adsorption isotherms and infrared spectroscopy suggests that the adsorption to sulfate occurs through a binuclear bridging

Fe—O—$S(O)_2$—O—Fe surface complex [101]. Other investigations using adsorption isotherm analysis indicate that phosphate species adsorb more strongly than sulfate ions [101]; however, PO_4^{3-} is weaker binding group than carboxylate groups [27]. The weak adsorption of the sulfate ion is assumed to be the reason little to no literature was found on magnetite stabilization using sulfate-containing surfactants other than small molecule soil species [102]. These binding functional groups are incorporated into chemical structures used to prepare bound surfactants in attempts to maintain stable dispersions independent of variations in pH as described in Section 2.10.

Electrostatic repulsion

A charge balance of the surface atoms of the iron oxide and an ionic stabilizer defines electrostatic stabilization. Essentially, the surface electric charge attracts ions of opposite charge and creates an electric double layer. At pH values above the isoelectric point magnetite's surface is negatively charged. In 1981 Massart reported that in an alkaline medium of polarizing or highly charged cations, such as ammonium, alkaline, or alkaline-earth ions, gave rise to flocculation [84]. However, low polarizing positively charged ions, such as the $N(CH_3)_4^+$ ion of tetramethylammonium hydroxide (TMAOH) stabilized magnetite. The negative charges of the colloids in alkaline media are assumed to be adsorbed Fe-O^- ions. Washing the alkaline precipitate with water does not favor peptization, which is the formation of a colloidal solution, because this removes the adsorbed – charges (OH^-) as well as the counterions [84]. When the solution is at a pH below the isoelectric point, the particles can be stabilized with cations such as the ClO_4^- ion of perchloric acid. Colloidal dispersion stability of a magnetite via electrostatic stabilization is possible only when the counterion is a weakly polarizing species [83, 84].

Magnetite nanoparticles coalesce in the presence of strong polarizing ions, such as NH_4^+, Na^+ and SO_4^{-2} [36, 84].

Lauric acid was used to stabilize magnetite in chloroform; however, the researchers report that only partially dispersible systems were achieved and precipitates immediately formed in polar solvents such as water, methanol and ethanol [103]. Fauconnier *et al.* investigated citric and gluconic acid adsorption onto maghemite particles for potential medical applications [104]. The citric acid stabilizes the iron oxide particles by electrostatic repulsions. Gluconic acid's "free alcoholic functions" may allow biological molecules to couple to iron oxide nanoparticles [104]. In their study maghemite was coated with varying amounts of citric acid, gluconic acid and citric/gluconic acid mixtures at low pH. Their dispersion stability was investigated as a function of pH. The researchers report that surface complexes of gluconic acid are weaker than citric acid complexes. However, mixtures of citric and gluconic acids create stable dispersions at pH 6 – 8. The researchers state that the citric-gluconic coated maghemite dispersion stability is very dependent on the concentration of citric acid [104].

Denizot *et al.* investigated the stabilization of iron oxide nanoparticles using phosphorlycholine as a water dispersible surfactant for iron oxide nanoparticles [105]. The phosphorylcholine surfactant forms a stable dispersion at pH ~5.5. The researchers attempted to create a stable dispersion at neutral pH by co-addition of negatively charged phosphorylglycerol surfactants. However, the binding of the functional group was reversible, and desorption occurred at pH > 6, which inhibits their intended application as a magnetic resonance contrast agent [105].

2.9.1 Steric or entropic repulsion

Magnetite stabilization by steric repulsive forces is achieved using a surfactant. Commonly, the surfactant is an amphiphilic molecule with a polar head (1) that adsorbs onto the surface of the magnetite nanoparticle chemically or physically and a hydrophobic tail (2) that extends out into the nonpolar carrier fluid to maintain colloidal stabilization (Figure 2.16).

The minimal distance between two particles is 2δ, where δ is the thickness of the surfactant layer (Figure 2.16). The surfactant thickness must be such that the sum of the energy of van der Waals (E_i, Equation 2.16, Section 2.4) and magnetic attractive forces (E_d, Equation 2.14, Section 2.4) is less than or equal to the thermal energy or Brownian motion of the particle system (Equation 2.18) [48].

$$\left|E_i + E_d\right| \leq kT \tag{2.18}$$

The steric stabilization mechanism may be described by two conceptual theories. One theory is that the surfactant acts to disguise the surface of the particle using absorbed surfactant tails that are chemically similar to the carrier fluid. When the particles approach, the chains of the surfactant interpenetrate creating an osmotic pressure and a repulsive force due to an increase in entropy as the surfactant chains begin to compress one another [106].

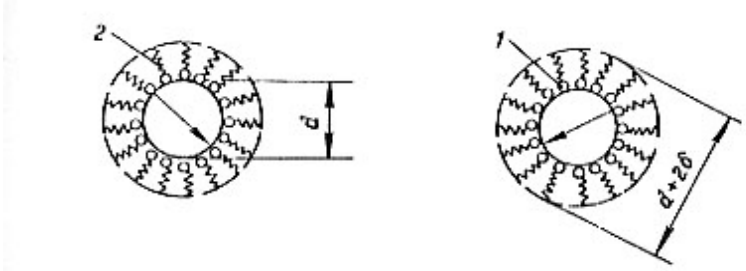

Figure 2. 16 Thickness of adsorbed surfactant layers on two magnetic nanoparticles [48].

In addition, Mackor developed a statistical mechanics approach to steric stabilization using a rigid rod attached to a universal hinge model of the system [3]. During particle-particle collisions the surfactant tails compress and repel one another [3]. The expression for the repulsive forces predicted by Mackor was modified by Rosenswieg *et al.* to convert the flat surface model into an integrated expression for two neighboring spheres

$$\frac{E_r}{kT} = 2\pi d^2 \xi \left[2 - \frac{l+2}{t} \ln\left(\frac{1+t}{1+l/2} \right) - \frac{l}{t} \right] \qquad (2.19)$$

where ξ is the concentration of adsorbed surfactant molecules on the surface of a particle, d is the particle diameter, l = 2s/d, s is the surface to surface separation, t = 2δ/d, k is Boltzmann's constant, T is the absolute temperature [3]. These interactions are visualized by a plot of potential energy versus surfactant coated particle surface-to-surface distance (Figure 2.17).

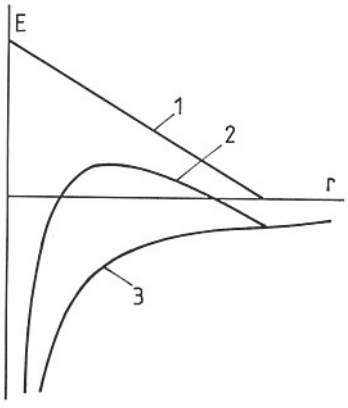

Figure 2. 17 Potential energy diagram for steric stabilization of nanoparticles where 1 = the repulsive forces due to surfactant, 2 = net energy, 3 = attractive energies of magnetic nanoparticles) [36].

The potential energy curves in Figure 2.17 indicate the importance of an adsorbed surfactant achieve steric repulsive forces sufficient to balance magnetic and van der Waals attractive forces. Then net energy is positive and serves as a barrier to particle agglomeration [36]. A sufficiently long surfactant chain creates a potential energy barrier (~25 kT) that is an order of magnitude greater than the thermal energy associated with each nanoparticle, so particle coalescence is minimized [3]. Theory described by Rosensweig's modified Hamaker Equation, suggests that surfactant tails must be greater than 1 – 2 nm to achieve steric stabilization and hence a stable ferrofluid [3]. However, the upper limit of the length of the surfactant tail is less well defined. As the length of the tail increases the magnetite concentration per unit volume decreases and subsequently the magnetic response of the ferrofluid will decrease. Moreover, exceedingly long surfactant tails may lead to agglomeration due to the irreversible collosion of coated particles [50].

2.10 Steric stabilization methods and materials for iron oxide nanoparticles

The steric stabilization of bare magnetite surfaces can be tailored for dispersibility into oil/hydrocarbon carrier fluids or aqueous media using amphoretic surfactants (Figure 2.18).

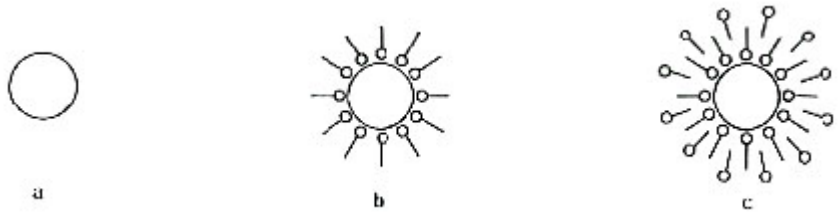

Figure 2. 18 Schematic of dispersion states of (a) magnetite core in oil based (b) and water based (c) magnetic fluids [32].

The polar head group indicated by the circle at the surface of the magnetite particle in Figure 2.18b and 2.18c can be either a phosphate, sulfate or carboxylate group. Oil-based dispersions (Figure 2.18b) are comprised of surfactants with a nonpolar tail segment that extends out into the nonpolar solvent. The water-based system depicted in Figure 2.18c is created using a bilayer method described below.

Phosphate containing surfactants

Phosphate containing surfactants for nonpolar ferrofluids dispersions include: alkyl phosphonates/phosphates such as dodecylphosphonic acid (DDP), hexadecylphosphonic acid (HDP) and dihexadecyl phosphate (DHDP) [103]. The researchers compared these phosphonate and phosphate surfactants to fatty acids such as oleic acid and lauric acid. The phosphonates and phosphates dispersions via TEM analysis show particle coalescence whereas the fatty acid coated magnetite particles appeared more discrete and separated. TGA analysis suggests that the alkyl phosphonate/phosphate strongly binds to the surface of the iron oxide particles; however, these coated systems showed reduced dispersibility in apolar solvents due to what appears to be a bilayer formation [103]. The multi-layered surface coverage of the surfactant species was hypothesized from TGA and DSC analyses.

Fatty Acids

In 1968 Papell was among the first to report the formation of colloid magnetite nanoparticle dispersions with oleic acid [88]. The researchers prepared magnetite by the ball-milled method and added oleic acid to prepare nonpolar hydrocarbon colloidal dispersions (Figure 2.12). Since then, several researchers have investigated the use of oleic acid as a steric

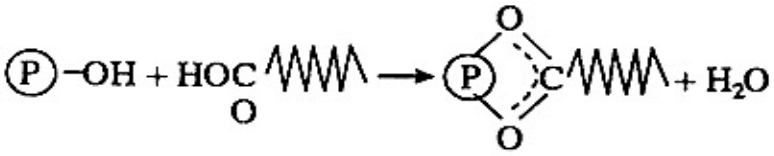

Figure 2. 19 Carboxylic acid chemisorption on the surface of magnetite particle (P) [17].

stabilizer for magnetite and maghemite nanoparticle dispersions in hydrocarbon solvents [17, 107-109].

The general method is to form iron oxides following the aqueous coprecipitation of the iron salts in the presence of oleic acid (C_{18}) dissolved in a nonpolar solvent (Figure 2.19). The adsorption occurs via interface mechanisms and extracts the particles into the nonpolar carrier fluid. The transfer of magnetite into the oil phase is achieved by modifying the high-energy hydrophilic surface to a lower energy hydrophobic surface. The proposed mechanism is via wetting inverse where the water adsorbed onto the surface of the magnetite is displaced by the polar head of the surfactant.

Formation of water-based fatty acid coated magnetite particle dispersions is complicated by the nonpolar nature of the hydrocarbon chain. Oleic acid, used for nonpolar dispersions, cannot form stable dispersions in water. Khalafalla *et al.* report investigations on the effect of the chain length of the fatty acid on forming water dispersible magnetite solutions [100]. The researchers observed that fatty acids with C_{10} to C_{15} are capable of making stable water-based dispersions (Table 2.6).

Table 2. 6 Effect of chain length of a series of fatty acids on the formation of water dispersible magnetite solutions [100].

Chain length, C_n	Acid name		Formula	Colloid formation[1]
	I.U.C. System	Common		
C_9	Nonanoic	Pelargonic	$CH_3(CH_2)_7COOH$	-
C_{10}	Decanoic	Capric	$CH_3(CH_2)_8COOH$	+
C_{11}	Undecanoic	Hendecanoic	$CH_3(CH_2)_9COOH$	+
C_{12}	Dodecanoic	Lauric	$CH_3(CH_2)_{10}COOH$	+
C_{13}	Tridecanoic	Ficocerylic	$CH_3(CH_2)_{11}COOH$	+
C_{14}	Tetradecanoic	Myristic	$CH_3(CH_2)_{12}COOH$	+
C_{15}	Pentadecanoic	Isocytic	$CH_3(CH_2)_{13}COOH$	+
C_{16}	Hexadecanoic	Palmitic	$CH_3(CH_2)_{14}COOH$	-
C_{18}	Octadecanoic	Stearic	$CH_3(CH_2)_{16}COOH$	-

[1] The + and - notation designates whether a colloid was formed or not formed, respectively.

Ammonium oleate, (ammonium soap) formed from oleic acid modified with an excess of an ammonia solution [$CH_3(CH_2)_7CH{=}CH(CH_2)_7COONH_4$], was investigated by Wu *et al*. to stabilize magnetite [87]. Stabilization was achieved using 2.0/0.6/97.4 a weight ratio of Fe_3O_4/ammonium oleate/water. The researchers do not mention specific procedures (such as deoxygenating the solutions); however, they do state that if the magnetite is prepared at temperatures below 60 °C the final iron oxide formed predominated by α – or γ – FeOOH forms. Magnetite dispersions prepared above 60 °C displayed saturation magnetizations of ~52 emu/g and XRD confirmed the magnetite crystal structure. Interestingly, TEM micrographs of the particles that were formed in these reactions showed aggregation at a pH of 12.49. However, when the particles were formed at a pH of 13.98, they were spherical and discrete. However, the researchers do not offer a reason for the particle dispersion quality's dependence on the pH and the parameters that govern their results are not clear [87].

2.9.2.1 Bilayer surfactant

Shimoiizaka first described the use of fatty acids to create iron oxide nanoparticles dispersible in water via the formation of a bilayer surfactant system [110]. Since then several methods have been reported for bilayer surfactant methods [17, 85, 100, 110]. The process often involves the formation of magnetite in the presence of a fatty acid such as oleic acid, which chemisorbs and extracts magnetite into a nonpolar carrier fluid. Then, the carrier fluid is removed and another amphoretic surfactant (usually a fatty acid) is added and the mixture is redispersed in water (Figure 2.20) [111]. The important property of the second surfactant is that it display a hydrophilic-lipophilic balance (HLB) number greater than 12 [36, 100]. The hydrophilic-lipophilic balance system characterizes the ratio of water-loving and oil-loving portions of a surfactant molecule, respectively, in an arbitrary range of 1- 40. The HLB number increases with increasing hydrophilicity.

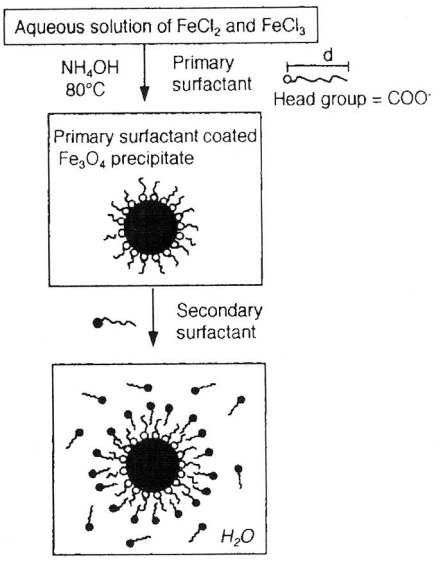

Figure 2. 20 Bilayer method depicting formation to achieve aqueous dispersions [111].

The combination of surfactants varies and includes, oleic acid with either polyoxyethylene-nonylphenyl ether or sodium dodecylbenzyl sulphonate [112]; mixtures of unsaturated and saturated fatty acids or saturated fatty acids for both layers. Wooding offers some experimentally determined concentrations of primary and secondary surfactant systems necessary to prepare stable water ferrofluids [17].

The main limitation of the bilayer method is the destabilization caused by dilution of the bilayer magnetic dispersion where the interpenetrating surfactant chains are weakly absorbed to the primary molecules [100, 113]. Recently Shen *et al*. developed a terminally unsaturated bilayer surfactant system, sodium 10-undecenoate [CH_2=CH(CH_2)$_8$$CO_2$Na], for stable aqueous magnetic dispersions [113]. These researchers followed similar methods as the earlier bilayer procedures; however, unsaturated fatty acids used as the primary and secondary surfactant were covalently linked via γ-irradiation. The covalent binding of the bilayers creates a more dilution stable system; however, these surfactant stabilized iron oxides may be limited in application due to their lack of biocompatibility.

2.10.1 Polymer surfactants

Dextran

Dextran is a polysaccharide polymer composed exclusively of α-D-glucopyranosyl units with varying degrees of chain length and branching. Groman *et al*. reports the use of dextran (M_w 10000 – 15000 g/mol) as a surfactant during the formation of maghemite/magnetite nanoparticles and followed by sonication at 100 °C [114]. The resulting polymer coated particles were modified with sodium citrate after which the pH was adjusted to 6.5 with addition of base [114]. The researchers do not report magnetization data.

However, Pardoe *et al*. offer detailed magnetic and structural properties on magnetite/maghemtite mixtures formed in the presence of dextran (40k g/mol) [75]. TEM micrographs show cluster-like particle formation with the dextran coating. Atomic absorption analysis indicated 0.56 wt. % Fe content. The results of the analysis were compared to iron oxides prepared in the presence of poly(vinyl alcohol) suggesting that the presence of polymer limits the particle size compared to particles prepared without polymer. The researchers state that the size of the dextran- and PVA-coated particles were 4.11 ± 0.85 nm and 5.78 ± 1.30 nm, respectively. The arrangement of iron oxide particles in a dispersion also depends on the polymer used. The magnetization data show that the dextran coated particles have a higher blocking temperature than the PVA coated particles, indicating more interparticle interactions.

Molday and Mackenzie also reported the formation of magnetite in the presence of 40k g/mol dextran [6]. In these studies the dextran was functionalized after magnetite stabilization by oxidization with periodate to create more hydroxyl groups to allow the amino groups of proteins to bind. The design was for immunospecific magnetic separation of cells [6]. The researchers report the formation of a stable nonaggregated dispersion containing 30 – 40 nm diameter polymer coated particles with 15 nm diameter iron oxide cores.

Polyvinyl alcohol

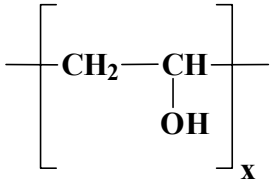

Polyvinyl alcohol (PVA) is a hydrophilic, biocompatible polymer formed by the hydrolysis of poly(vinyl acetate) and often contains residual acetyl groups. Iron oxide nanoparticles formed

in the presence of aqueous polyvinyl alcohol (30-40k g/mol) created necklace-like chain ordering ~100 nm in length [75]. The particle sizes of the PVA dispersed iron oxide particles are 5.78 ± 1.30 nm with a Fe content of 7.7 wt. % [75].

Another investigation reported by Lee *et al*. describes the formation of magnetite in the presence of 1 wt. % PVA (saponification value of 87% and M_n ~22k g/mol) solution [76]. The magnetite cores are 4 – 7 nm in diameter and display saturation magnetization values of ~55 emu/g. The investigators suggest that PVA irreversibly binds to the surface of magnetite using FT-IR absorbance shifts. The three absorption bands used were observed at 1380, 1330 and 1083 cm^{-1}, the first two bands are assigned to the C – H deformation and the later to the C – O stretching of PVA [76].

Poly(methacrylic acid)

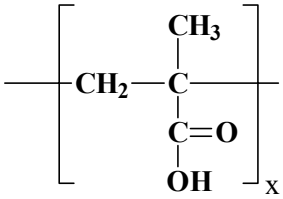

Magnetite particles were synthesized from a non-stoichiometric molar ratio of Fe^{2+} and Fe^{3+} and were stabilized with poly(methacrylic acid) in a procedure that included sonication at elevated temperatures [77]. The solutions, particles and ferrofluids generated in this study were characterized with vibrating sample magnetometry (VSM) to provide magnetic property data, dynamic light scattering (DLS) to understand solution characteristics and TEM and powder X-ray diffraction (XRD) to determine particle sizes. In addition, the zeta potentials were determined by electrophoretic mobility measurements of the ferrofluids as a function of pH.

Magnetic properties were provided in terms of reduced magnetization. VSM and TEM analyses indicated that iron oxide particles ~9 nm in diameter, and DLS suggested clusters ranging in size from ~17 – 38 nm in diameter. The effects of temperature and time during sonication were investigated in light of the potential for polymerchain scission during this process. The researchers concluded that the molecular weight of the poly(methacrylic acid) decreased with increasing sonication time.

Poly(ethylene oxide)-b-poly(methacrylic acid)

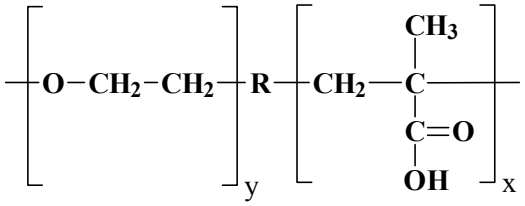

Wormuth reports the preparation of magnetite in the presence of poly(ethylene oxide)-b-poly(methacrylic acid) at 60 °C [81]. Interestingly, the iron salts in a 1:2 molar ratio of Fe^{2+}/Fe^{3+} were added dry to an aqueous polymer mixture and allowed to dissolve in the presence of the polymer stabilizer. The hydrated iron salt mixture is acidic and the diblock surfactant polymer remains dispersed undissolved until the pH is raised above 5 with base. As the pH of the solution is raised, the polymer dissolves and magnetite is formed. The researchers suggest that magnetite formation in the presence of the PEO-PMAA leads to reduced particle size, which averaged ~5nm in diameter (TEM), with 5 nm of surfactant stabilizer (TGA). The magnetization curve for 5.5 wt % solids PEO-PMAA coated nanoparticles display a magnetic susceptibility of 0.02 and a saturation magnetization equal to 60 emu/g Fe_3O_4 [81].

Poly(ethylene oxide) based surfactants

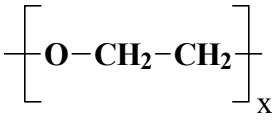

Poly(ethylene oxide) (PEG) is a hydrophilic water soluble biocompatible polymer. Several investigations have reported the use of poly(ethylene oxide) based surfactants to increase the biocompatibility of the iron oxide dispersions. One example is the preparation of iron oxide nanoparticles stabilized with Brij® 97 [polyoxyethylene (10) oleyl ether], $C_{18}H_{35}(OCH_2CH_2)_nOH$, for MR contrast agents [11]. Another investigation reports the formation of Fe_3O_4 via the oxidation of $FeSO_4$ in the presence of 4000 g/mol poly(ethylene oxide) [78]. TEM micrographs show particle sizes of ~50 nm, uniformly dispersed with some multi-particle clustering. The researchers propose that the PEG was partially oxidized during the formation of magnetite as suggested by a C=O adsorption peak at 1630 cm^{-1} via FT-IR [78].

Another investigation was reported where poly(ethylene oxide) having two carboxylic acid groups was used to stabilize magnetite (Figure 2.21).

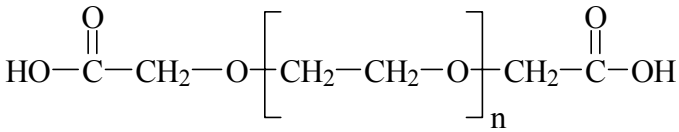

Figure 2. 21 α, ω-Dicarboxymethylpoly(oxyethylene) (DCPEG)

The modified poly(ethylene oxide) containing terminal carboxylate groups was used to couple magnetite to lipase [80]. Magnetite particles were synthesized in the presence of 50 wt. % dicarboxypolyethylene glycol (DCPEG) (Sapporo Breweries Ltd., Japan) with M_n ~2000 g/mol in water. The DCPEG coated magnetite was bound to lipase using a water soluble carbodiimide. The researchers suggest that the DCPEG irreversibly adsorbed to the magnetite through hydrogen bonding of the carboxylate of the DCPEG with the hydroxyl of the iron oxide surface. The coupling of the lipase occurs through the amino groups of the enzyme reacting with the carboxyl group of the DCPEG forming acid-amide bonds. The size range of the particles is 30 – 70 nm, which appears aggregated in the TEM micrograph [80]. The lipase bound iron oxides were large enough to be magnetically separable in relatively low (250 Oe) magnetic fields. Unfortunately, the researchers report a reduction in the enzymatic activity of these magnetic enzymes, which they attribute to crosslinking of the enzyme molecules.

In an attempt to prevent the reduction of enzymatic activity, the same researchers investigated the preparation of an activated magnetic modifier using DCPEG-coated magnetite reacted with N-hydroxysuccinimide, which could be directly coupled to amino groups of the enzyme molecule (Figure 2.22) [115]. The enzymes were either lipase or L-asparaginase.

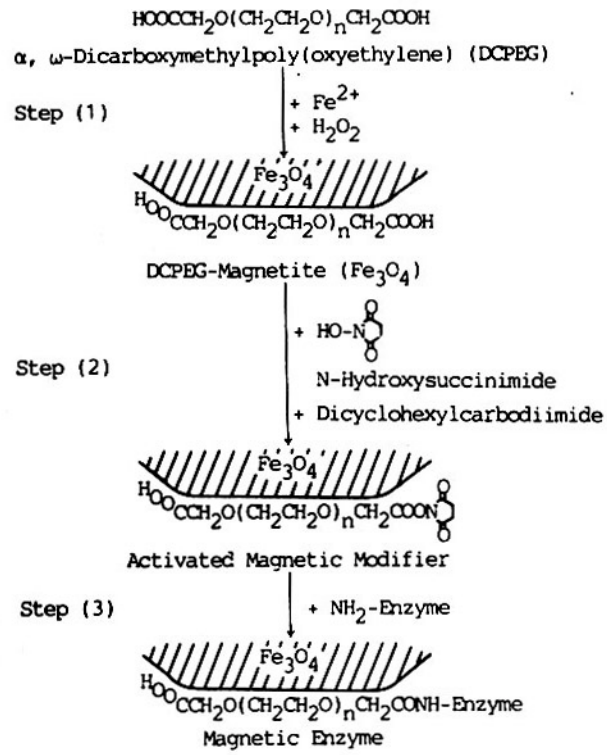

Figure 2. 22 Synthesis of a magnetic enzyme by coupling activated DCPEG-coated magnetite to the enzyme. (Step (1) = Fe_3O_4 formation in the presence of DCPEG via oxidation; Step (2) = activation of carboxyl groups on DCPEG coated magnetite; and Step (3) = the coupling of the activated magnetic modifier to the enzyme amine groups [115])

In these investigations magnetite was prepared by oxidizing Fe^{2+} (1 wt. %) with hydrogen peroxide (0.03 wt. %) in the presence of 30 wt. % DCPEG (Nippon Oil & Fat Co., 4500 g/mol) at 50 °C. These polymer-coated magnetite particles were dispersible in both water and organic solvents (solvents for poly(ethylene oxide)). The average particle size of the activated (succinimide functionalized) DCPEG coated magnetite was ~200 nm. The succinimide functionalized DCPEG coated magnetite was coupled to the enzyme. These magnetic enzymes formed stable dispersions in organic solvents and water and were recovered from solution by a 6000 Oe applied magnetic field without loss of enzymatic activity [115].

Polymer templates

A polymer template can serve as constrained environments for the formation or stabilization of iron oxide nanoparticles. One unique synthetic method is offered by Underhill and Liu who report the synthesis of an ABC triblock polymer nanosphere template for maghemite formation [116]. These structures were synthetically designed to act as nanoreactors for the oxidation of Fe^{2+} solution and form water dispersible iron oxide nanoparticles with controlled sizes. The triblock polymer is polyisoprene-block-poly(2-cinnmoylethyl methacrylate)-block-poly(tert-butyl acrylate) (Figure 2.23).

The micellar structure is comprised of a polyisoprene corona, a crosslinked poly(2-cinnamoylethyl methacrylate) (PCEMA) shell and a poly(*tert*-butyl acrylate) (P*t*BA) core. The nanosphere template is prepared in a complex multi-step process. The triblock polymer is dissolved in THF and micelle formation is induced by adding 65 vol. % hexane.

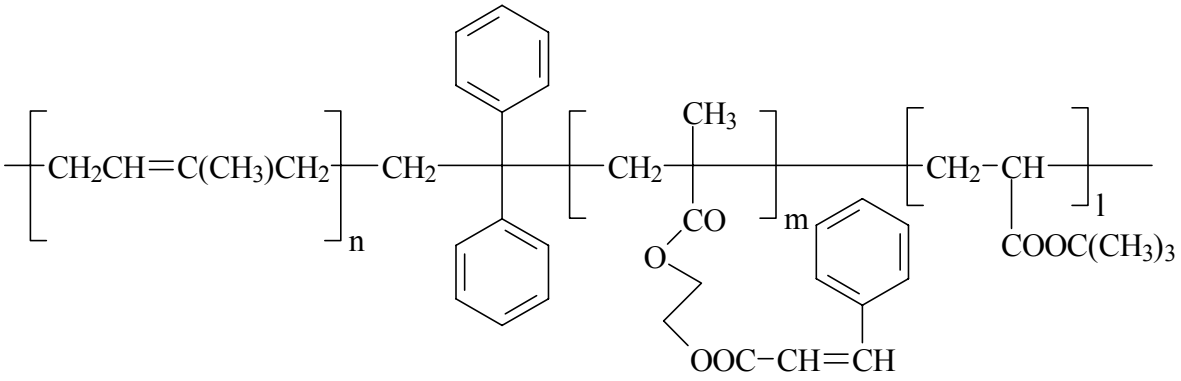

Figure 2. 23 Poly(isoprene)-***b***-poly(2-cinnmoylethyl methacrylate)-***b***-poly(tert-butyl acrylate) used as triblock nanosphere template for maghemite formation [116].

The poly(isoprene) (PI) segments extend out into the nonpolar solvent creating the micelles. Once the micellar structure is formed the PCEMA central segments are crosslinked via photolysis as indicated in their reaction scheme as a black circle (Figure 2.24).

The polymer structures were made water dispersible by hydroxylating the PI tail blocks. The P*t*BA core was made compatible for the iron oxide formation by removing the t- butyl groups with iodotrimethylsilane forming pendent carboxylic acids. These designed nanosphere templates were soaked in aqueous $FeCl_2$ solution. The Fe^{2+} ions that were swollen in the core of the templates were converted to maghemite using NaOH and H_2O_2 (Figure 2.24) [116]. The particle size ranges from 4 – 16 nm and were dispersible in water. The magnetic properties of these water dispersible nanoparticles were not investigated. However, the researchers did state that the iron oxide nanoparticle structures in a water dispersion was stable for "tens of minutes without appreciable precipitation".

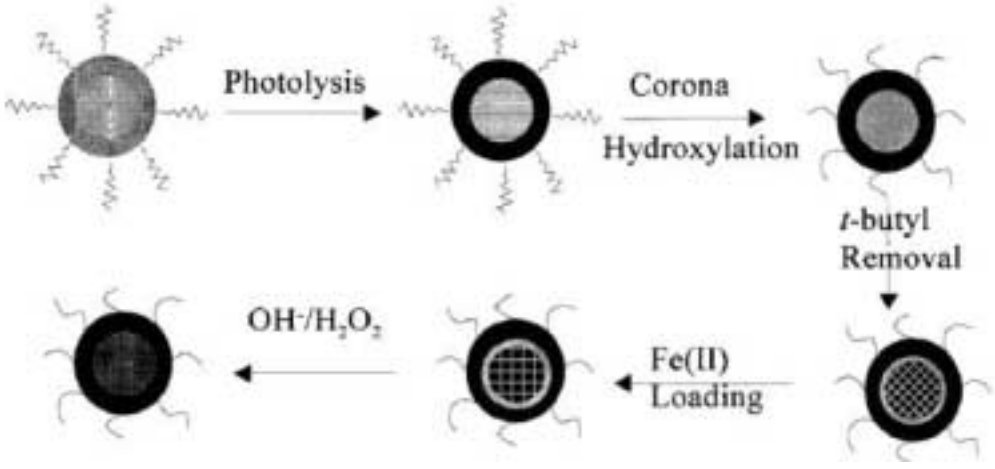

Figure 2. 24 Polymer template design and maghemite formation [116].

Another type of polymer template is a porous gel structure, where iron oxide nanoparticles are formed in the constrained architectures of a polymer gel [117, 118]. Pore in the gel serve as nanoreactors where iron oxides nanoparticles are formed *in situ*. Breulmann *et al.* investigated the formation of magnetite inside the pore of an elastic polystyrene-polyacrylate copolymer gel template [117]. The researchers state that the sponge-like gel with a mesoporous open cell structure was prepared by copolymerization of monomer mixtures in bicontinous microemulsions. The synthetic parameters of the polymerization allow the pore size and carboxylate functionality to be tailored. The gel described for magnetite formation was an open cell structure. The gel was soaked in a Fe^{2+}/Fe^{3+} aqueous solution for 2 – 4 days. The orangish-red swollen gel was transferred into a 1 M NaOH aqueous solution. Magnetite formation was observed as the orange-red gel rapidly turned from green-brown to black. The researchers report that the iron oxide content of the gels is ~3.5 – 8 wt. % Fe_3O_4 with just one reaction cycle and that the loading can be increased up to 20 wt. % iron with successive swelling/reaction cycles. The Fe_3O_4 particles formed in these polymer templates are ~16 nm in diameter and are bound to the carboxylate functional groups of the polyacrylate component of the gel pore. The researchers also suggest that the gel "acts as a spatial framework and molecular template for magnetite deposition" [117]. They propose that the "nucleation of magnetite is favored by kinetic and redox changes accompanying the binding of metal cations at the carboxylate side groups, which are present in high densities along the side groups" [117].

These same researchers also investigated the use an acrylic acid based copolymer gel. The polymer gels were synthesized by the copolymerization of acrylic acid (AA), 2-hydroxyethylmethacrylate (HEMA) and ethyleneglycoldimethacrylate (EGDMA) monomer

mixtures in aqueous solution containing polyoxyethylene(10) cetyl ether surfactant. Surprisingly, the researchers state that attempts to prepare magnetite in the pore structure of this polymer gel was unsuccessful. The acrylate based polymer gel was swollen with a Fe^{2+}/Fe^{3+} aqueous solution. When transferred to the 1 M NaOH solution the orangish-red solution turned a darker red-orange indicative of Fe(II) oxyhydroxides.

Since the *in situ* formation of magnetite in this particular gel structure was not possible, the researcher prepared magnetically responsive hybrid composite systems by swelling the dried polymer gels with aqueous dispersions of previously prepared magnetite. These systems appear to be versatile in that the changes in the polymer crosslink density and chemical composition alter the structural nature of the templates. The dried magnetite filled composites showed zero coercive force and minimal hysteresis; however, magnetization analysis in terms of Fe_3O_4 concentration was not reported [119].

2.11 Polymer composites: μm and submicron particle systems

Micron and submicron sized magnetically responsive polymer composite systems can be created by either incorporating the iron oxide particles inside polymer particles by *in situ* polymerization or by attachment to the polymer particle surface. In these systems the overall size of the magnetically loaded or coated polymer particles is larger.

Iron oxide nanoparticles incorporated into polymer particles synthesized *in situ*

The incorporation of magnetite into polymer particles synthesized *in situ* is generally referred to as a magnetic composite. Examples of the preparation of these magnetically loaded polymer particles are provided. One method reported by Zaitsev *et al.* is the addition of a magnetite nanoparticle dispersion to the seed precipitation polymerization of methacrylic acid and

hydroxyethyl methacrylate monomers [120]. In this procedure, 1 wt. % magnetite dispersed in ethyl acetate was added to 0.5 – 2.5 wt. % monomers, crosslinker (1 – 10 mol % of monomer) and 0.025 wt. % azobisisobutyrnitrile initiator (AIBN) and polymerized at 65 °C under N_2. The magnetite and the polymer coated magnetite nanparticles are ~6 – 80 nm and 340 – 400 nm in diameter, respectively. The researchers report the magnetite's saturation magnetization prior to polymer coating, but do not provide the value for the magnetite loaded polymer particles.

Lee and Senna describe the seed polymerization of polystyrene in the presence of sodium oleate stabilized magnetite [121]. Sodium oleate coated magnetite was added to an emulsion of styrene monomer and surfactant. The solution was mixed with seed polystyrene particles and the heterogeneous polymerization of polystyrene was initiated. The core shell morphology of the particles consists of polystyrene centers with magnetite/polystyrene composite shells. The researchers suggest that this heterogeneous polymerization method may be used to prepare a wide variety of magnetic composite microspheres. The magnetic properties of these core-shell type polystyrene-magnetite/polystyrene materials were not investigated.

Another interesting magnetic composite is formed by poly(isobutylcyanoacrylate) particles with magnetic cores [15, 122]. Polyalkylcyanoacrylates are drug compatible and biodegradeable [122] polymers prepared by anionic polymerization. Magnetite was prepared by the crystallization of an amorphous Fe^{2+} hydroxide gel [89]. The magnetite/poly(ethyl-2-cyanoacrylate) (core/shell) nanoparticles were prepared by anionic initiation of the monomer by covalent bases. In this process a 0.75 % w/v magnetite suspension in 2 x 10^{-3} N HCl solution was added to the polymerization medium. The monomer (1 % w/v) was added dropwise to the stirring solution were polymerization occurred. The size of the polymer coated particles and their internal

magnetic cores vary depending on experimental parameters. Arias *et al.* report polymer coated particles sizes of ~144 nm in diameter with ~84 nm magnetic cores [122]. However, larger composite particles (0.22 μm) and larger magnetic cores (0.01 – 0.05 μm) may be produced [15].

Iron oxides nanoparticles attached to the surface of polymer particles

An alternative magnetic composite system is achieved by the adsorption of magnetite nanoparticles onto the surface of polymer spheres. These systems are just one type of magnetic microspheres reported in literature. The vast literature regarding these materials will not be discussed in detail; however, the interested reader should find the following books resourceful [123-125].

One example is the surface absorption of citrate stabilized magnetite onto polystyrene (PS), polystyrene/poly(isopropylacrylamide) (P(S/NIPAM) core/shell) and poly(isopropylacrylamide) (P(NIPAM) spheres [126]. The method was based on previous work by Furuzawa *et al.* [127] and includes: 1) the preparation of anionic iron oxide nanoparticles and cationic latex particles; 2) the adsorption of the anionic iron oxides particles to the surface of seed polymer particles; 3) encapsulation of the magnetic coated particles onto seed latexes [126]. The researchers note that the adsorption of anionic magnetite particles onto the cationic latex particles increased in the order of cationic PS < cationic amino containing P(S/NIPAM) < cationic amino containing P(NIPAM). The polymer particle size ranges from ~100 – 500 nm in diameter with 10 nm diameter magnetite particles attached. Magnetization investigations were reported for the magnetite nanoparticle; however, the magnetic properties of the magnetite coated polymer particles were not investigated.

2.12 Silica coating of iron oxides nanoparticles

A silica layer on the surface of iron oxide nanoparticles may be desirable because it can 1) create a functional surface to tailor dispersibility of the nanoparticles or 2) form an insulating layer to control electron tunneling between particles, which may be important in charge transport or magnetooptics [128]. In addition, the silica coating might also provide better protection against toxicity. A method to coat magnetite with silica was developed by Philipse *et al.* in the early 1990s [129]. Following this process, magnetite nanoparticles were formed by the coprecipitation of di- and trivalent iron salts and then coated with two consecutive layers of silica in water and ethanol, respectively. The first thin silica layer lowers the isoelectric point of the dispersion to pH 3.3; however, the particles are clustered. The second layer creates stable dispersion of discrete particles ~35 – 45 nm in diameter with magnetite cores [129].

2.13 Effect of COOH on iron oxide nanoparticle formation and magnetic properties

The surfactants used to sterically stabilize magnetite nanoparticles often contain carboxylate functional groups. The carboxylates are popular because they form stable covalent attachment of the surfactant to the iron oxide surface. The effect of the surface adsorption of functional groups in nanoparticles has been investigated in terms of 1) its presence during magnetite formation and 2) the resulting magnetic properties displayed by the system. The significance of these effects is heightened because the particles have high surface areas and surface to volume ratios.

Effect on the growth of iron oxide nanoparticle

Bee *et al*. investigated the effect of the concentration of citrate ions on the size of maghemite particles. The actual synthesis of the particles was achieved by a stoichiometric coprecipitation of Fe^{2+} and Fe^{3+} hydrated salts in the presence citric acid trisodium salt using a base forming

magnetite [130]. The resulting magnetite particles were oxidized to maghemite with ferric nitrate at elevated temperatures. The molar ratio of citrate to the total Fe^{2+} and Fe^{3+} was varied from 0 to 10 %. The researchers report that the size of the particles decreases with increasing concentrations of citrate (0 % and 3 % citrate results in ~8 nm and 3 nm in diameter particles, respectively) as determined by powder XRD and TEM analyses.

Krishnamurti and Huang studied the influence of citrate on the kinetics of Fe^{2+} oxidation and the resulting hydrolytic products of Fe^{3+} [97]. The researchers suggest that the oxidation of Fe^{2+}, in the form of $Fe(ClO_4)_2$, to Fe^{3+} species is inhibited by the complexation of citrate ions, which also retards kinetics of the reaction [97]. In addition, the complexation of the citrate species to Fe^{3+} affects the crystallization processes of the iron products [97]. Specifically, the adsorption of citrate onto the iron nuclei produced by hydrolysis inhibits crystal growth mechanisms [130]. Huang and Wang restate these same results in 1997 [102]. Furthermore, the rate constant governing the oxidation of Fe^{2+} in the presence of inorganic ligands decreases in the order: perchlorate > fluoride > nitrate > chloride > carbonate > sulfate >silicate > phosphate [102].

Liu and Huang investigated the effect of the presence of citric acid during iron oxide synthesis using XRD and atomic force microscopy (AFM). The results suggest that the citrate significantly influences the formation, fine scale morphology and surface geometry, such as surface roughness of the particles [131]. Specifically, in the absence of citrate species their experimental procedures produced acicular goethite and cubic maghemite. However, in the presence of citrate only lath-shaped lepidocrocite was obtained. In addition, increasing concentrations of the citric acid caused significant decreases in the crystallinity of the iron oxides formed. Moreover, the presence of the citrate led to changes in the surface geometry [131].

While their research was not specific to magnetite formation, these investigations suggest that similar effects may be observed in other formation mechanisms and subsequent surface and structural features. Other related studies that focused on the influence of carboxylate ions on the formation of ferric oxides show similar results [96, 132, 133]. The formation and crystallization of iron oxide particles appear inhibited by the presence of citrate ions and the particle sizes decrease with increasing concentration.

Proposed effects of COOH on magnetic properties

Surfactants bound to nanomagnetite particles affect magnetic properties and are related to the dependence of the particle size on magnetic properties described in Section 2.3. In fact, considering the reported evidence that the presence of carboxylate groups during the formation of iron oxides leads to smaller particles than in its absence, the two variables may not be completely separable. Similarly, the theories and experimental interpretations regarding the effect of a polar surfactant bound to the surface of magnetite nanoparticles conflict and remain debatable.

One of the first theories, introduced by Kaiser and Miskolczy, was the existence of a magnetic dead layer created by chemically bound surfactant molecules on the surface of magnetite [134]. It was proposed that the nonmagnetic layer accounted for the experimentally observed decrease in magnetization of the surface stabilized particles. The theory allowed the calculation of an effective magnetic particle size using magnetization data and resulted in a predicted nonmagnetic layer of ~8Å thick. Since this initial study, several investigators have proposed alternate theorizes using a variety of techniques.

Mössbauer spectroscopy analysis uses ^{57}Fe sensitivity to investigate the surface magnetic effects of the iron oxide nanoparticles and their superparamagnetic relaxations, τ. The existence of the nonmagnetic layer was investigated and argued against with Mössbauer analyses in several different studies [135-138]. The arguments consistently state that a magnetic dead layer created by the carboxylate chemisorption onto iron oxide nanoparticles would produce a central peak in a Mössbauer spectrum, indicative of a nonmagnetic paramagnetic compound [135, 138]. However, the lack of this central peak appears to justify the opposition to a magnetic dead layer [135-138].

An alternative theory suggested that chemisorption of the surfactant pins surface spins in extremely high anisotropy fields [135]. Furthermore, Mössbauer spectroscopy analysis of τ revealed a larger effective magnetic anisotropy energy constant, K, for the coated iron oxide nanoparticle than for particles without carboxylate groups [137, 138]. Davies *et al.* suggest that particles containing sufficient concentrations exhibit spin-pinning of the iron oxides and that these particles require higher applied fields to achieve saturation (~20T) [137]. Measurements performed at applied fields lead to lower magnetization values than for uncoated particles, which is subsequently mistaken for a particle size effect [137] as evidenced by Mössbauer spectroscopy [43, 135]. These results suggest that the surfactant molecule bound to the surface allows for spin pinning, which gives rise to a noncollinear spin structure with reduced magnetic properties [43, 137, 138]. From these studies the canted layer is predicted to be ~1 nm thick [27].

2.14 Characterization of magnetic nanoparticle systems

FT-IR analysis: investigations of carboxylate binding to magnetite surfaces

Fourier transform infrared (FT-IR) spectroscopy can be used to investigate the covalent nature of the surface stabilization of oleic acid bound to magnetite nanoparticles [107]. Molecularly free carboxylate group (COO^-) of oleic acid show a carboxyl-group stretching IR band at 1710cm^{-1}, whereas the band attributable to bound carboxylate group on the magnetite surface yields shifts to lower frequencies and broadens. The chemically bound COO^- group is observed at 1600 cm^{-1} due to the antisymmetric stretching of the COO^- group [107].

Additionally, Rocchiccioli-Deltcheff *et al*. investigated adsorbed species at the surface of magnetite particles in apolar solvents using FT-IR (Figure 2.25) and thermal gravimetric analysis (TGA) [139]. Molecular chemisorbed water and surface hydroxy group IR bands were assigned to 3440 cm^{-1} and 3380 cm^{-1}, respectively. The researchers propose that the carboxylate group adsorbs primarily via a chelating bidentate configuration to a single surface Lewis acid Fe^{3+} species and the IR bands appear at ~ 1520 cm^{-1} [$\nu_{as}(CO_2^-)$] and 1425 cm^{-1} [$\nu_s(CO_2^-)$] (Figure 2.25a).

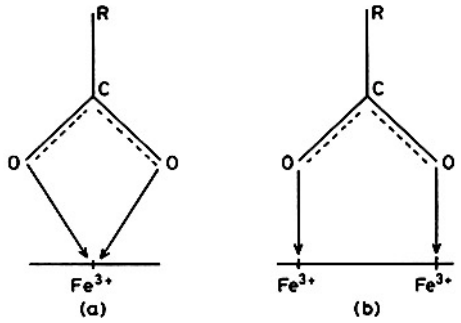

Figure 2. 25 Binding modes of carboxylates on the surface of magnetite [139].

A weak vibrational energy band was observed at 1560 – 1580 cm^{-1} attributed to a small quantity of oleate bridging in a bidentate configuration (Figure 2.25b) [139].

Powder X-ray diffraction

The determination of the crystalline structure using X-ray diffraction is performed to obtain the crystalline lattice spacings of a sample. The crystal structure contains symmetry elements along planes, axes or centers. The intercept of any plane of a symmetry axis is defined by the reciprocal values of the intercepts, hkl, known as Miller indices. The X-ray radiation source can be CoKα or FeKα, however CuKα is less desirable because Fe of the sample strongly adsorbs this radiation and leads to reductions in X-ray intensity [61].

Magnetite's X-ray diffraction pattern is shown in Figure 2.26. The peak intensity can be used to quantify the proportion of iron oxide forms in a mixture by comparing experimental peak and a reference peak intensity.

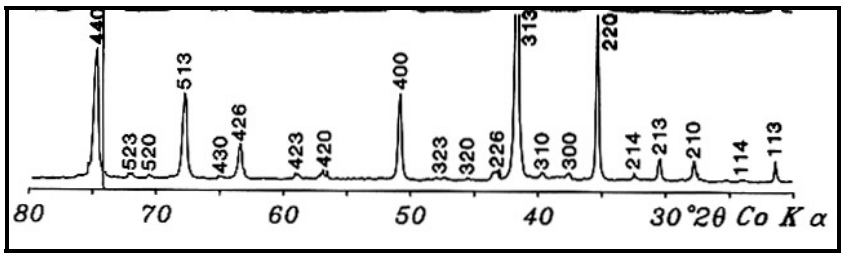

Figure 2. 26 X-ray diffraction pattern of pure magnetite (intensity versus 2θ) [61].

The crystal size can be calculated from line broadening from the XRD pattern using the Scherrer formula shown in Equation 2.20.

$$D_{hkl} = \frac{K\lambda}{b\cos\theta} \tag{2.20}$$

The Equation uses the corrected reference peak width at angle θ, where λ is the X-ray wavelength, b is the corrected width of the XRD peak at half height and K is a shape factor which is approximated as 0.9 for magnetite [27]. The corrected peak height takes into account instrument effects.

Transmission Electron Microscopy

Particle sizes can also be determined by digitizing TEM micrographs to mathematically determine the particle size distribution or using Martin's diameters of 250 particles [134]. The particle size distribution can be calculated using Equation 2.21 from the TEM micrographs.

$$p(d) = \frac{1}{D\rho_d\sqrt{2\pi}} \exp\left(\ln\frac{D}{D_O}\right)^2 \tag{2.21}$$

Using this Equation, ρ_d is the diameter standard deviation and D is the diameter and D_O is the mean diameter, respectively [10].

Vibrating Sample Magnetometry

The magnetization properties investigated using vibrating sample magnetometry provide fundamental magnetic behavior quantification. Information includes: saturation magnetization

(M_S), magnetic susceptibility (χ), magnetic remanence (M_R), coercive force (H_C), and particle size information. Particle sizes and their distributions can be calculated using Equation 2.22.

$$D_m = \left(\frac{18kT}{\pi} \frac{\chi_i}{\rho M_S^2} \right)^{1/3} \tag{2.22}$$

In this formula, $\chi_i = (dM/dH)_{H \to 0}$ is the initial magnetic susceptibility, k is the Boltzmann constant, T is the absolute temperature in Kelvin, and M_S is the saturation magnetization [84].

Several characterization methods are available to investigate the properties of magnetic particle systems (Table 2.7). More detailed characterization information may be found in literature and texts such as Cornell and Schwertmann's "Iron Oxides in the Laboratory; Preparation and Characterization" [61] and magnetic fluids books [3, 22, 24, 36, 48].

Table 2. 7 Some magnetite nanoparticle characterization techniques.

Method	Abbreviation	Determines
Powder X-ray Diffraction	XRD	lattice spacing, particle size, iron oxide structure, degree of crystalline
Energy Disspersive Spectroscopy	EDS	lattice spacing, particle size, iron oxide crystallinity structure
Transmission Electron Microscopy	TEM	dispersion quality, particle size
Magnetic Force Microscope	MFM	magnetic adhesion and forces
Small Angle Neutron Scattering	SANS	e- spin orientations, magnetic structures and oxygen parameters
Small Angle X-ray Scattering	SAXS	particle size and lattice spacing
Mössbauer Spectrometry	-	magnetic relaxation times (τ) and core/surface magnetic property variations
SQUID-based Magnetometers	-	magnetic flux and general magnetic properties
Variable frequency AC magnetic susceptometry	-	magnetic susceptibility of magnetic fluids
Rotating Sample Magnetometer	-	measures rotational hysteresis
Vibrating sample magnetometer	VSM	general magnetic properties
Thermal gravimetric analysis	TGA	weight % iron oxide
Atomic Flame Absorbance Elemental Analysis	AFA-EA	weight % iron

2.15 Magnetic nanoparticle applications

Electronics

In electronics technology researchers are attempting to increase storage density and processing speeds by decreasing the size of components. Nanocrystal superlattices offer some very interesting research and potential technologies. However, as the size of the components decreases the spontaneous reversal of magnetization desired for biomedical applications leads to difficulty in maintaining stable magnetic moments [49]. This superparamagnetic limit is a serious limitation for the stable storage of information [1]. The creation of nanocrystals passivated with organic moieties to prevent physical contact of metal cores and act as superlattice templates may allow for tunable magnetic properties. In fact, some researchers suggest that the optical, electrical and transport properties are tuneable by the spacing of the particles via control of the organic sheath thickness [2]. Advances in the future are currently focusing on investigating the feasibility of a spin based electronics system by incorporating the spin degree of freedom to current charged based systems or using the spin alone [140]. Giant magnetoresistive sensors are considered the beginnings of the spin-based age. Currently, spintronics is finding application in the head sensors industry and researchers hope to open up access to control over spin in electronics devices in the future.

Biomedical applications

Iron oxide nanoparticle systems offer great potential in a diverse number of biomedical applications due to their guidable nature. The biocompatibility and dispersion quality may be enhanced by surface stabilization of the magnetite nanoparticles. Biomedical applications under current investigation include retinal detachment therapy [4, 5], cell separation methods [6, 7], tumor

hyperthermia [8], improved MRI diagnostic contrast agents [9-12] and as magnetic field-guided carriers for localizing drugs or radioactive therapies [13-15]. The nanomagnetic particle surface can influence both material durability in biological environments and also toxicity issues.

Dextran coated iron oxides have been utilized in cell separation applications [6]. The researchers oxidized the surface of the dextran coated particles with periodate leading to Schiff base linkages which were then reacted with the amino groups of protein A, wheat germ agglutinin or immunoglobulins [6]. The process for cell separation is visualized in Figure 2.27 using an external magnetic guidance system (+++) [7].

The ability to target and biologically link a magnetic particle to a cell is approached by several different methods. A specific application is bone marrow transplant, where a magnetically directable process is known as positive rescue [7]. Moreover, a list of advantages for this approach is proved in the paper[7].

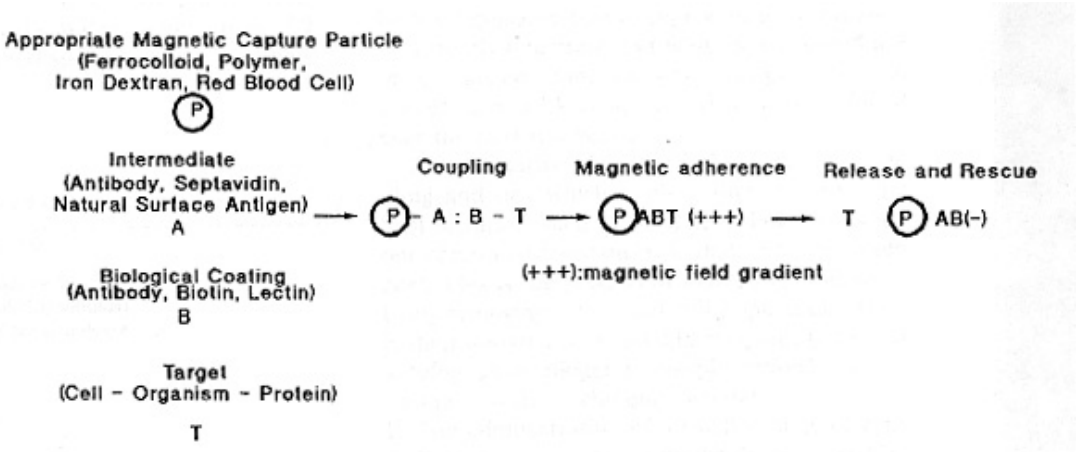

Figure 2. 27 Flow diagram of magnetic capture cell [7].

Iron oxide colloidal dispersions with high magnetic field gradients near the surface display the diagnostic sensitivity needed for detection as magnetic resonance contrast agents [9]. There is extensive literature in this area and magnetite nanoparticles are a main focus for the magnetic materials. The biodistribution of the dextran-coated iron oxides and dextran coated particles with poly-L-lysine modified surfaces was studied in rabbits and rats[9]. The researchers found that a large dextran coating on the iron oxide lead to particle accumulation in the lymph nodes [9]. Also, intravenously injected polymer coated iron oxide nanoparticles maintained some magnetic field of their own while in blood vessels after exposure to an external magnetic field (exhibit vascular remanence). The particles migrate into white cells and then into bone marrow and reticulo-endothelial structures (liver, spleen, and lymph nodes) [12]. These physical behaviors are predictable physiological responses and may be useful in magnetically targeted delivery systems; however, the magnetic remanence may alter their performance as MRI contrast agents

Other materials include magnetoliposomes, designed as MR contrast agents which are prepared by derivatizing magnetoliposomes with poly(ethylene glycol) . The concept was to try to minimize the rapid uptake of the magnetoliposomes by cells of the reticulo-endothelial system. The iron oxide was stabilized with lauric acid and the vesicle composition was a mixture of dipentadecanoyl-phosphatidylglycerol and dimyristoyl-phophatidyl-ethanolamine-N-poly(ethylene oxide) [74].

Other researchers report the synthesis of iron oxide nanoparticles for MRI contrast agents using starch, albumin, silicones and poly(ethylene glycol) with particle sizes between 30-150 nm [12]. Kim *et al*. prepared iron oxide nanoparticles coated with polyoxyethylene (10) oleyl ether and sodium oleate and investigated their application as MR contrast agents [10, 11].

Magnetic materials designed as magnetically delivering or targeting enzymes are described by Inada *et al*. using magnetite-PEG-enzyme conjugates [141]. In addition, magnetic latex particles are of interest in biomedical applications as immunomicrospheres with bound immobilized antigens for antibody purification [112]. Extensive literature resources are available regarding magnetic drug delivery in the following citations [123-125].

2.16 Magnetite toxicity

Magnetite in biological systems is commonly encapsulated in a protein cage and hence nontoxic [94]. The toxicity of the water dispersible ionic and citrate-based iron oxide nanoparticles was investigated by Lacava *et al*. to access their biocompatibility [142]. The researchers analyzed the toxicity of uncoated and citrate coated $MnFe_2O_4$ nanoparticles. Pure citrate, uncoated iron oxide and citrate coated $MnFe_2O_4$ solutions were intraperitoneally injected into Swiss mice. The neat citrate did not produce a significant biological response. However, both of the magnetic fluids caused severe inflammatory reactions of the spleen and kidney hilum, and diarrhea.

Another literature source stated the toxicity of magnetite nanoparticles (LD_{50} in rats) was 400 mg/kg [143]. Other analysis shows that the morphology of the peritoneal cells was affected and damage of the nuclear material of lymphocyte and neutrophil was observed. These investigations indicate that iron oxide nanoparticles will require a biocompatible sheath to prevent toxic interactions in biological media [142].

Investigations on the blood clearance of dextran-coated magnetite suggest that magnetite is at least partially metabolized [144]. The particle size distribution of the dextran (40k g/mol) coated magnetite is 0.02 – 0.52 μm [143]. The blood clearance inversely related to the median particle

size [143]. Okon *et al.* provide biodegradation results as indirect evidence that the dextran coated magnetite particles undergoe a multi-step biodegradation and may bind to ferritin and slowly cleared from the blood stream. However, it should be noted that the dissolution of magnetite nanoparticles might be inhibited by the adsorption of polar surfactant species [27]. Considering that dextran is superficially adsorbed on the surface of magnetite, the differences may or may not be significant.

The polyalkylcyanoacrylate magnetite nanoparticles similar to those described in Section 2.11 were studied for their toxicity in mice [15]. The coated particles are ~0.22 μm in diameter with 0.01 – 0.05 μm diameter magnetite cores. The researchers determined that the LD50 was 242 mg/kg and 245 mg/kg for the polyisobutylcyanoacrylate particles and the polyisobutylcyanoacrylate-magnetite particles, respectively. Therefore, the research suggests that the presence of magnetite has a minimal effect on the acute toxicity of the materials investigated [15].

Chapter 3: Polymer Stabilized Magnetite Nanoparticles

3.1 Introduction

Magnetic nanoparticles display magnetic properties different from their bulk material counterparts. These unique properties originate from the size of the particles, which are below a critical diameter for magnetic vector domain wall formation. In the absence of an externally applied magnetic field, thermal energy is sufficient to cause the magnetic moments in these single domain particles to equilibrate, and they do not display magnetic behavior. Their magnetic moments align rapidly in the direction of the field and display a net magnetization when the particles are placed in an external magnetic field. When the magnetic field is removed, thermal energy is again sufficient to cause the particles' vector moments to randomize and they no longer display a strong magnetic response. The magnetic response of these nanomagnetic materials disappears when the external field is removed (i.e., zero magnetic remanence and zero coercivity) in short times relative to the experiment time. These properties define superparamagnetic behavior and make nanoparticles ideal components of vehicles for magnetic field-directed delivery of therapeutic agents.

Magnetic attractive forces and inherently large surface energies (> 100 dyn/cm) [10] favor particle aggregation [3, 36]. Magnetic nanoparticles can be dispersed in carrier fluids in the presence of surfactants. Such fluid dispersions of small magnetic particles are known as "ferrofluids" [3].

Current and potential applications for these nanomagnetic materials in electronics and biotechnology are diverse. Nanomagnetic films have great promise for electronic and electrical devices, sensors, electromagnetic shielding and high-density digital storage [29]. Biomedical applications under current investigation include retinal detachment therapy [4], cell separation methods [6, 7], tumor hyperthermia [8], improved MRI diagnostic contrast agents [9-12] and as magnetic field-guided carriers for localizing drugs or radioactive therapies [13-15]. The nanomagnetic particle surface can influence both material durability in biological environments and also toxicity issues.

These particles must remain non-aggregated, be oxidatively-stable and display high saturation magnetization during application. Transition metals offer high magnetization, but are sensitive to oxidation, which converts their magnetic behavior to antiferromagnetic (loss of magnetic response). Currently, oxidization of the transition metals remains a hurdle, especially in biomedical, oxygen-rich environments. Iron oxides, such as magnetite (Fe_3O_4) and maghemite (γ-Fe_2O_3), are oxidatively more stable and display ferrimagnetism. In addition, investigations show magnetite has low toxicity (LD_{50} in rats = 400 mg/kg) and polymer-coated magnetite has not shown any acute or subacute toxicity in animal studies [143].

Magnetite is commonly prepared by condensation of divalent and trivalent iron salts by reaction with a strong base (pH of 9 – 14). The magnetite crystal structure forms readily in aqueous media. Methods to prevent agglomeration include the use of electrostatic and steric or entropic stabilizers. Aqueous dispersions have been prepared using electrostatic [83] and bilayer surfactants [85, 100, 110, 113], polymers as steric stabilizers [75-78, 81, 114] and polymer templates [116]. Applications of the magnetite dispersions comprised of electrostatic stabilizers and bilayer

surfactants are limited due to pH sensitivity and dispersion stability, respectively. Many of the polymer stabilizers lack a functional component to bind to the magnetite surface, which decreases their dispersion stability.

This dissertation reports the preparation of novel hydrophilic triblock copolymers containing controlled concentrations of bis(hydromethyl) propionic acid, carboxylic acid groups, in the central segments and poly(ethylene oxide) tails (PEO-COOH-PEO) (Figure 3.1). A method for preparing magnetite nanoparticles and subsequent dispersion and stabilization using these polymers will be described. The resulting polymer-coated magnetite nanoparticles appear to be single crystals, which are dispersible in both water and chlorinated organic solvents. These dispersions are stable in pH ranges common to biological systems and at the isoelectric point of uncoated magnetite (~pH 6.8).

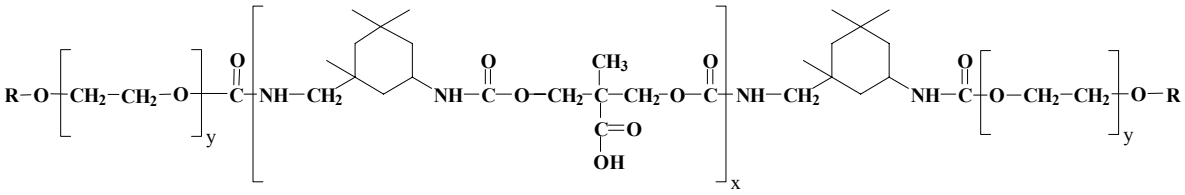

Figure 3. 1 Controlled molecular weight triblock dispersion stabilizers comprised of hydrophilic poly(ethylene oxide) tail blocks and central short urethane segments containing carboxylic acid groups which react with the magnetite surface. "x" = 3, 5, or 10 and "y" = 44, 112 or 340.

3.2 Experimental

3.2.1 Materials

Tetrahydrofuran (THF, EM Science, 99.5%) was refluxed over sodium with benzophenone until the solution was deep purple and fractionally distilled prior to use. Potassium *tert*-butoxide (Aldrich, 1.03M in THF) was stored under nitrogen and used as received. Ethylene oxide (EO, Kodak) was dried over calcium hydride (CaH_2) and distilled onto activated molecular sieves. Glacial acetic acid (Aldrich) was diluted to a 4 M aqueous solution. Dimethylformamide (DMF, EM Science) was dried over CaH_2, fractionally distilled to a clean, dry round bottom flask containing activated molecular sieves (4Å) and stored under N_2 at 0 °C. Isophorone diisocyanate (IPDI, Aldrich, 99.5 %) was fractionally distilled and stored under N_2. Poly(ethylene glycol) monomethyl ether (PEO), 2000 and 5000 g/mol M_n, were purchased from Aldrich. A 15000 g/mol M_n poly(ethylene oxide) mono-*t*-butyl ether was synthesized by anionic living polymerization of ethylene oxide monomer in a high pressure Series 4561 Parr reactor. All monofunctional PEO oligomers were dried overnight at 80 °C under reduced pressure prior to use. The bis(hydroxymethyl) propionic acid (DMPA, Aldrich) was dried in a vacuum oven at 60 °C for 2 days prior to use. The dibutyltin dilaurate (DBTL, Aldrich) catalyst was used as received.

$FeCl_3 \cdot 6H_2O$ and $FeCl_2 \cdot 4H_2O$ (Aldrich) were stored under nitrogen in a dessicator and used without further purification. All water used was filtered with Millipore gradient Model A10 (specific conductance ~0.52 μS/cm) and deoxygenated for a minimum of 30 minutes with ultrahigh purity N_2. Ammonium hydroxide (NH_4OH, 50% v/v aqueous, Alfa-Aesar) was deoxygenated prior to use for a minimum of 30 minutes with ultrahigh purity nitrogen (99.9%).

Dichloromethane (Burdick and Jackson) was used as received. Hydrochloric acid (Aldrich) was diluted to a 25 % v/v aqueous solution.

3.2.2 Synthesis of polymer precursors and triblock polymer stabilizers

Synthesis of a 15000 g/mol monofunctional poly(ethylene oxide) oligomer to be used as a component in the triblock copolymer stabilizers. Ethylene oxide monomer (60.4 g) was transferred to the chamber of a clean, dry 300-mL Parr reactor via a cannula using a slight pressure gradient (vacuum) toward the receiver flask, where the receiver flask was chilled externally with a dry ice/isopropanol bath. Potassium *tert*-butoxide initiator in THF (3.91 mL, 1.03 M) and 100 mL of THF solvent were syringed into the reactor with stirring. The temperature was slowly increased to 60 °C and the exotherm of the anionic initiation of the monomer was observed with an increase in temperature (up to 131 °C) and pressure (up to 120 psi) in the Parr reactor. The polymerization was monitored by the decrease in pressure (~10 hours) at 60 °C with stirring. The living polymerization was terminated with an excess of dilute acetic acid (2.46 mL, 4 M). Upon reaction completion, the THF was removed under reduced pressure and the polymer was resolidified from hot acetone and dried in a vacuum oven at ambient temperature.

Synthesis of carboxylic acid-containing triblock copolymer stabilizers. An exemplary procedure for a triblock polymer stabilizer with an average of three carboxylic acid groups in the central segments and 2000 g/mol M_n poly(ethylene oxide) tails blocks (2k-3-2k) is provided. Copolymers with other tail block lengths (5000 and 15000 g/mol M_n) were prepared in a similar manner by appropriately varying the molar stoichiometries to obtain controlled average

Table 3. 1 Chemical compositions and targeted number average molecular weight of carboxylate containing triblock copolymer stabilizers, where the tail blocks ranged from 2000, 5000, and 15000 g/mol poly(ethylene oxide) with 3, 5 or 10 carboxylic acid units in the central segments.

Composition (PEO-COOH-PEO)	Targeted M_n (g/mol)
2k-3-2k	5200
2k-5-2k	5900
5k-3-5k	11000
5k-5-5k	11700
5k-10-5k	13500
15k-3-15k	35300

concentrations of carboxylic acid groups (3, 5 or 10 units in the central carboxylic acid containing segments) (Table 3.1).

The first part of the reaction involves diisocyanate capping of the monofunctional PEO. The dried PEO (60 g PEO, M_n=1929 g/mol, 0.0311 mol) was transferred molten to a warm flame-dried, 3-neck, 250-mL, roundbottom flask equipped with a mechanical stirrer and nitrogen inlet. Isophorone diisocyanate (13.18 mL, 0.622 mol, ρ = 1.049 g/cm^3) was syringed into the flask which was placed in an oil bath maintained at 50 °C under N_2. Dibutyl tin dilaurate catalyst (100 ppm, 0.0083g) was added to the reaction flask via syringe. The melt reaction was monitored by Fourier transform infrared spectroscopy (FT-IR) by observing the decrease of the isocyanate

absorption peak at 2260 cm^{-1}. The isocyanate functionalization of the PEO required ~30 minutes.

Once all of the poly(ethylene oxide) was capped with the diisocyanate, this material and the remaining isophorone diisocyanate were chain extended with bis(hydroxymethyl) propionic acid (DMPA) (6.258 g, 0.0467 mol) dissolved in a minimal amount of purified DMF (~50 mL) and another 100 ppm increment of DBTL catalyst (0.0083 g). Reaction completion was determined by the absence of the isocyanate peak in the FT-IR, which required ~36 hours total reaction time for this composition. DMF was removed under reduced pressure at ~53 °C and ~500 mTorr. The polymer was dissolved in chloroform, and the chloroform solution was washed three times with water to remove any unreacted DMPA. The copolymer was coagulated and solidified by adding the chloroform mixture into an excess of cold hexane. The polymer was recovered by filtration and dried in a vacuum oven at ambient temperature.

3.2.3 Magnetite formation and steric stabilization

A novel procedure for preparing a stabilized magnetite composition using a PEO-COOH-PEO triblock copolymer with ≈2000 g/mol M_n PEO endblocks and an average of three carboxylic acids in the central segment (2k-3-2k) was developed and is provided. This composition utilizes 34.9 wt. % Fe_3O_4 charged to the reaction. All solutions (water, base and polymer/CH_2Cl_2) were carefully deoxygenated prior to use, by purging with ultrahigh purity dry nitrogen for a minimum of 30 minutes.

The first reaction of this sequence involves formation of magnetite nanoparticles in anaerobic conditions at ambient temperature. Aqueous solutions of $FeCl_3 \cdot 6H_2O$ (0.389 M, 2.0 g) and $FeCl_2 \cdot 4H_2O$ (0.195 M, 0.736 g) reagents were prepared separately under N_2 and syringed into a

3-neck, 250-mL, round-bottom flask equipped with a mechanical stirrer and pH electrode connected to a pH meter. The fittings for the apparatus were attached with vacuum-tight adapters to maintain an inert nitrogen environment. NH_4OH (50% v/v aqueous) was quickly syringed into the flask until a pH of 9.5 was reached (~10 mL) with rapid stirring (~60 rpm) immediately after the addition of aqueous iron salts. The solution quickly turned black through bluish-green rust phases indicating the formation of magnetite. The nucleation and growth of magnetite particles were allowed to occur for 30 minutes with stirring under a N_2 atmosphere.

After this, the N_2 flow was terminated and the steric stabilizer solution dissolved in CH_2Cl_2 (2 g PEO-COOH-PEO polymer in 25 mL CH_2Cl_2) was syringed into the flask and allowed to interact with the magnetite for 30 minutes with stirring (pH ~8.5 – 9). The CH_2Cl_2 solvent was subsequently removed with a strong N_2 flow (~2 hrs) and the resulting polymer-magnetite nanoparticle aqueous suspension was neutralized with dilute HCl (25 % v/v aqueous) to a pH ~6.5 – 7. The resulting stable dispersion was transferred to a dialysis membrane (Spectra pore 7, MWCO 1000) and was dialyzed against water for three days (refreshing the dialysis water twice/day). Particle aggregates in the salt-free magnetite ferrofluids were removed by centrifuging for 30-minute time intervals where the sediment was discarded and the process was repeated until little to no precipitation was observed in the bottom of the centrifuge tube. This generally required centrifuging the magnetite for 3 – 5 intervals.

3.2.4 Polymer precursors and triblock polymer stabilizer characterization

^1H and quantitative ^{13}C NMR analyses were acquired on a Varian Unity 400 NMR spectometer operating at 400 and 100.6 MHz, respectively. For quantitative ^{13}C NMR investigations of the polymer stabilizers, 0.63 g of polymer, 2.4 mL of $CDCl_3$ or d_6-DMSO, and

52 mg of chromium trisacetylacetonate ($Cr(acac)_3$) were analyzed with a 4.8 s relaxation delay and inverse gated decoupling. The relaxation agent was added to decrease spin-lattice relaxation times and provide quantitative analyses. FTIR spectra were collected on a Nicolet Impact 400 FTIR spectrometer with liquid samples cast onto salt plates. Titrations used to determine the concentration of carboxylic acid groups in the triblock polymers were conducted by dissolving the polymer (0.5 g) in 95 v/v % ethanol (25 mL) with 0.1 N KOH as titrant and phenolphthalein as an indicator. Each sample was titrated in triplicate to obtain an average concentration of carboxylic acids per polymer chain.

3.2.5 Characterization of the polymer-stabilized magnetite

The magnetite dispersion quality was investigated with a Phillips 420T transmission electron microscope (TEM) at 100kV. Aqueous dispersions of the polymer-stabilized magnetite were diluted to the appearance of a "weak tea", deposited on carbon-coated copper grids and allowed to air dry. The concentrations of Fe_3O_4 were determined by elemental analyses. Elemental analysis (EA) was performed by Desert Analytics Laboratory by treating the samples with hot concentrated nitric acid followed by concentrated perchloric acid until complete dissolution was achieved. The sample solution was analyzed by Inductively Coupled Plasma methods (ICP) to determine iron. Iron was calculated from sample response relative to standards and blanks.

The crystalline structure and particle sizes were investigated with powder X-ray diffractometry (XRD) and electron diffraction (EDS). XRD studies of powder samples were measured using a Philips Electronics Instruments APD 3720 X-ray diffractometer. The X-ray diffraction patterns were taken from 10 to 80 (2θ value) using Cu Kα radiation. EDS investigations were run on a high resolution Philips EM430 TEM instrument. The aqueous

polymer-coated magnetite dispersion was placed on a carbon coated copper grid and allowed to dry.

Magnetic properties were measured in the solid state using a Standard 7300 Series Lakeshore Vibrating Sample Magnetometer (VSM). The saturation magnetization value was determined from the plateau region of the magnetic flux density of a solid sample at 8000 Oe applied field with a sensitivity of 0.1 emu. The saturation magnetization in emu/(weight sample) was normalized with the weight percent of magnetite derived from elemental analysis to obtain emu/g Fe_3O_4.

3.3 Results and Discussion

The primary objectives in this work have been to develop methodologies for preparing dispersions which are (1) highly concentrated with discrete magnetite nanoparticles, and (2) which have the highest possible magnetic susceptibility and saturation magnetization. For most medical applications, these nanoparticles must be coated with biocompatible, hydrophilic stabilizers so that they can be dispersed in biological fluids.

Triblock copolymer stabilizers comprised of a central urethane 'anchor block' which chemisorbs onto the magnetite surfaces, and hydrophilic 'tail blocks' designed to extend out into water and provide dispersion stability have been synthesized (Figure 3.2). The central anchor blocks were prepared with systematically varied concentrations of carboxylic acids to better understand the effects of multiple covalent bonding sites on the ability to produce irreversibly bound complexes. Previous studies have shown that certain functional groups including carboxylic acids, phosphates and sulfates can bind to magnetite [27].

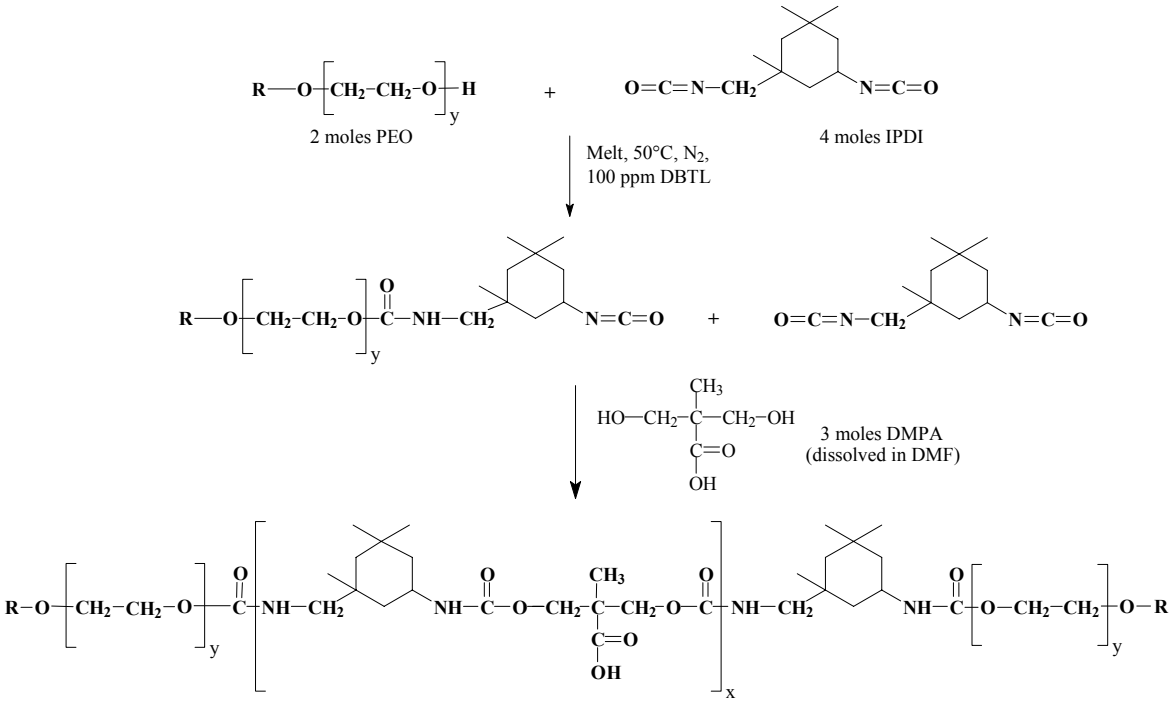

Figure 3. 2 Synthesis of hydrophilic carboxylic acid-containing triblock copolymers to serve as dispersion stabilizers for magnetite nanoparticles (PEO-COOH-PEO), where R = CH_3 or t-butyl.

Carboxylic acid groups have been reported to chemisorb to magnetite through reaction with iron on the particle surfaces [27, 139]. The hydrophilic, poly(ethylene oxide) tail blocks are well-known to be biocompatible [145, 146].

Living polymerizations of ethylene oxide can produce tail block lengths with controlled molecular weights, which enables optimization of the dispersions. One important parameter is to determine the critical block length necessary to produce stable dispersions. The length of the

stabilizing polymer chain must be sufficient to balance the magnetic attractions and the van der Waals attractive forces. However, an excessively long polymer segment reduces the concentration of magnetic particles, which can be incorporated into the polymer-magnetite material.

The tail block lengths which have been investigated thus far ranged from 2000 - 15000 g/mol monofunctional poly(ethylene oxides). Triblock polyurethane stabilizers were synthesized using a two-step procedure. The polymer tail block was capped with the diisocyanate in the first step where there was an excess of the diisocyanate to ensure that the relatively high molecular weight component was quantitatively incorporated into the block copolymer. In these reactions it is important to have an excess of isocyanate present during the first step to minimize coupling of monofunctional PEO oligomers. In the second step the isocyanate species were reacted with the hydroxyl groups of DMPA dissolved in a minimal amount of DMF, to provide homogeneity.

Side reactions forming carbamates and CO_2 occurred with higher reaction temperatures and addition of excessive catalyst. Mild reaction conditions minimized the carboxylate hydroxyl group reacting with the isocyanate, which helps to maintain the targeted acid concentration. The concentration of acid groups in the central segment of the polyurethane segment was varied from 3 – 10 units in order to determine the quantity necessary to bind to the surface of the nanomagnetite. The reaction completion was determined by the disappearance of the isocyanate (NCO) absorption peak via FTIR (Figure 3.3).

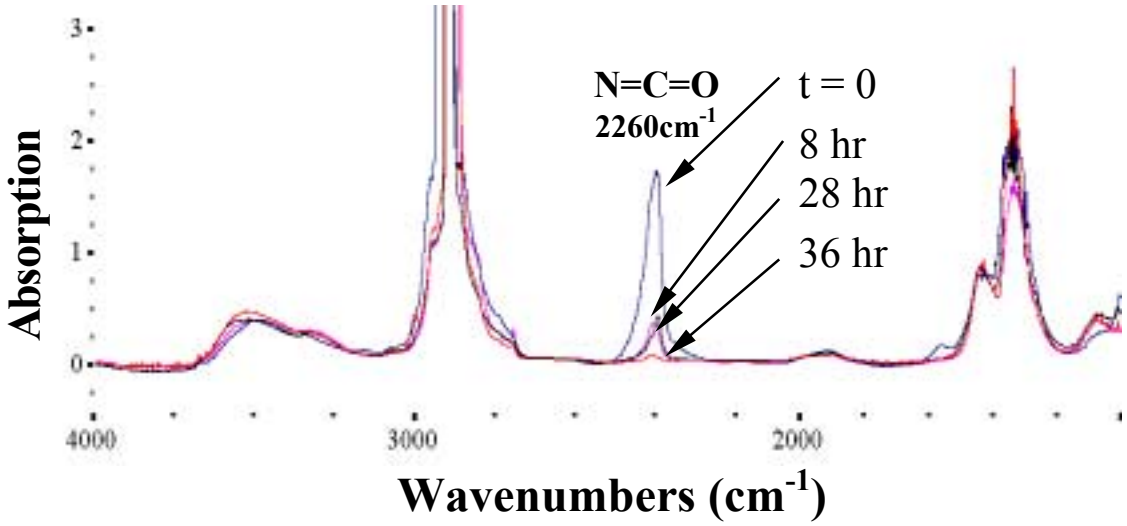

Figure 3. 3 Disappearance of the isocyanate absorbance at 2260 cm^{-1} via FT-IR during polyurethane synthesis of the carboxylic acid containing triblock copolymers.

The time required for complete isocyanate disappearance depends on the concentration of carboxylic acids incorporated into the polyurethane central segment of the polymer stabilizer. The synthesis of a triblock copolymer comprised of 2000 g/mol PEO tail blocks and 3 moles of DMPA (3 carboxylic acid units) in the central polyurethane segment (connected by 4 moles of IPDI) required ~36 hrs for the complete disappearance of the NCO peak via FT-IR (Figure 3.3).

The average number of carboxylic acid groups per chain was determined by quantitative ^{13}C NMR and titration studies (Table 3.2). Titration values show that the average concentrations of carboxylic acid groups incorporated in the triblock polymers were essentially quantitative.

Table 3. 2 Concentration of carboxylic acids/chain determined by quantitative ^{13}C NMR and titration analyses, where the targeted number is shown underlined in the composition column (^{13}C NMR samples in $CDCl_3$ with the exception of * sample, which was in d_6-DMSO).

Composition (PEO-COOH-PEO)	Quantitative ^{13}C NMR	Titration
2k-**3**-2k	3.1	3.9 ± 0.2
2k-**5**-2k	2.4	3.9 ± 0.1
5k-**3**-5k	2.9	3.2 ± 0.2
5k-**5**-5k	7.0	6.8 ± 0.2
5k-**10**-5k	3.8, (9.9)*	9.3 ± 0.0
15k-**3**-15k	—	3.4 ± 0.3

Inverse gated decoupling and the use of the spin-spin relaxation agent, $Cr(acac)_3$ allowed a quantitative ^{13}C NMR analysis for the determination of the carboxylate group (174.6 ppm). The carbonyl signal was ratioed to the methylene carbon signal of the poly(ethylene oxide) block endgroup (52 ppm) (Figure 3.4). Target values were achieved according to ^{13}C NMR and titration analyses, with the exception of the ^{13}C NMR analysis of the 2k-5-2k and 5k-10-5k stabilizers. The deviation was attributed to a micellar formation in the chloroform, due to the large number of acid groups relative to their respective block lengths. When these samples were analyzed dissolved in d_6-DMSO the integration values for the concentration of carboxylate groups are similar to the targeted and titration values.

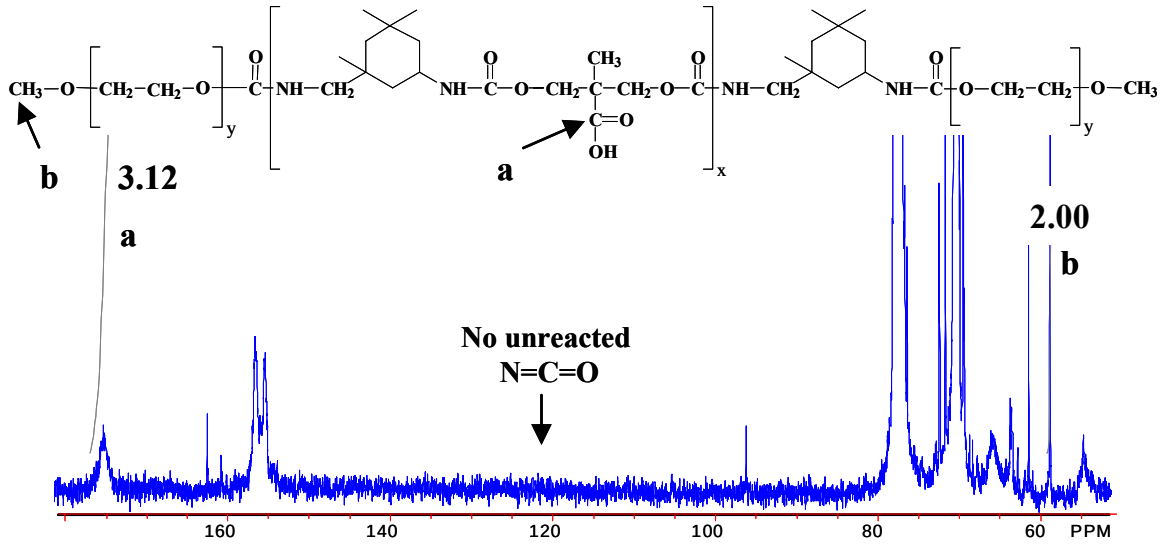

Figure 3. 4 Quantitative ^{13}C NMR used to assess the concentration of carboxylic acid groups in the triblock copolymer stabilizers.

The concentration of carboxylic acid groups per chain could not be determined for the triblock copolymer comprised of 15000 g/mol PEO tail segments because the allowable sample size was not sufficient for this high M_n polymer for detection. Purified polymer stabilizers do not display a peak at 153.7 ppm in the ^{13}C NMR spectra indicating absence of unreacted isocyanate species.

These polymer stabilizers were used to coat magnetite nanoparticles, in a process where the magnetite was formed first. The formation of magnetite nanoparticles was achieved via aqueous coprecipitation of $FeCl_2$ and $FeCl_3$ hydrated salt solutions at room temperature under N_2 with a strong hydroxide base. The molar ratio of the Fe^{2+}/Fe^{3+} was 0.5 for quantitative conversion. All solutions were deoxygenated prior to use and reacted immediately to minimize oxidation of the Fe^{2+} species and side reactions leading to nonmagnetic iron oxides [61]. The base was quickly

syringed into the flask with rapid stirring (~1 – 3 s) to a pH of 9.5 – 10. Previous investigators reported that quick addition of base with rapid stirring creates magnetite with improved magnetic response [86].

Ammonium hydroxide was used to prepare magnetite because the nature of its cation produces better magnetic properties compared with other alkaline-based hydroxides such as KOH, NaOH and LiOH [86]. After base addition the reaction was stirred at ambient temperature for 30 minutes to allow for nucleation and crystal growth to occur [27].

The carboxylate containing polymer stabilizer was added after magnetite formation because the presence of this functional group is known to retard the kinetics of nucleation and affect the crystallization mechanisms [97, 102]. The polymer was dissolved in dichloromethane to potentially promote interfacial interactions with the deprotonated carboxylic acid and the surface of the iron oxide nanoparticles.

After mixing for 30 minutes the dichloromethane was removed by a strong N_2 purge in order to assure the complete transfer the polyethylene oxide based stabilizer into the water phase. At this stage, if stirring was stopped the magnetite settled out of solution indicating that the carboxylate group was not irreversibility bound to the surface of the magnetite. However, when the pH of the reaction mixture was lowed to pH 6.5 – 7 stable dispersions were obtained.

The binding of the carboxylic acids in the polymer onto nanomagnetite was investigated as a function of pH by removing small aliquots of the solution in unit pH intervals from pH 10 to pH 3 during the addition of dilute acid. Aqueous polymer/magnetite aliquots at pH 9 and 10 were unstable and settled after a few hours. The dispersion at pH 8 remained stable for one week and then settled out of solution.

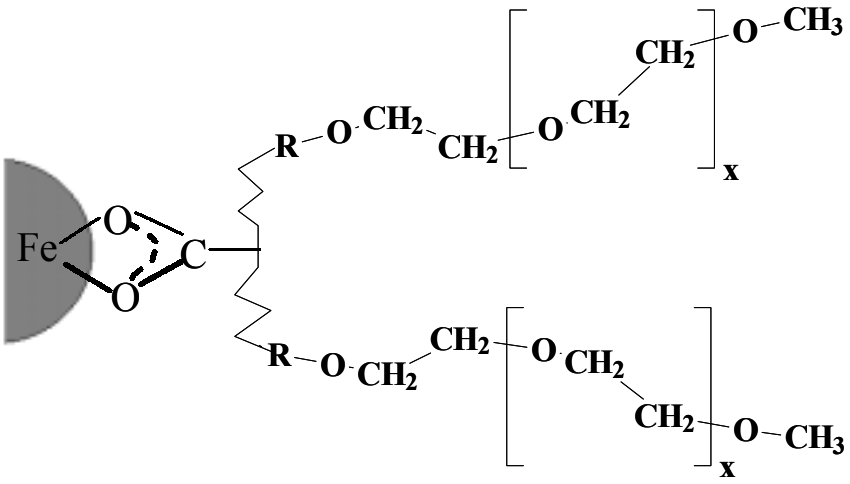

Figure 3. 5 The central segment of the stabilizer anchors to the magnetite surface via the carboxylic acid groups while the hydrophilic tail blocks extend into water.

Stable dispersions were observed at pH 7 to pH 3, which was the lowest pH investigated. This preliminary pH stability study suggests that magnetite stabilization occurs between pH 8 and pH 7. Below pH 8 the deprotonated carboxylate group binds onto the surface of magnetite creating a stable dispersion at the isoelectric point of bare magnetite (pH 6.8) and the physiological pH (~7) (Figure 3.5). The neutralized polymer coated magnetite dispersions were dialysis and centrifuged.

In these experiments the concentration of polymer stabilizer used was selected by calculating the number of carboxylate groups in the polymer capable of binding to the surface of a ~10 nm particle. The calculations were determined by converting the mass of magnetite theoretically obtained to the theoretical number of Fe_3O_4 particles using the density of magnetite (5.26 g/cm^3)

and the volume of a particle 10 nm in diameter. For example, 0.857g of Fe_3O_4 is equivalent to 3.16 x 10^{17} Fe_3O_4 particles. The number of surface sites available for chemisorption, on a 10 nm in diameter particle, was determined by considering the surface area consumed by a carboxylic acid group (0.16 nm^2) [30]. Using this information 1.2 g of polymer stabilizer (containing an average of 5 carboxylic groups and 2000 g/mol PEO tail blocks) was theoretically needed to cover the surface of 0.857g of magnetite (41.7 wt. % Fe_3O_4). However, in practice an excess of polymer stabilizer (0.8 g excess, 32.2 wt. % Fe_3O_4) was added to ensure that the magnetite was well coated with polymer.

The concentration of carboxylic acid groups per chain did not appear to have an effect on the attainment of stable dispersions of magnetite. Stable polymer-bound magnetite nanoparticle dispersions were prepared with all of the carboxylic acid containing triblock polymers (Table 3.2). These coated magnetite particles were dispersible in water or chlorinated solvents such as dichloromethane and chloroform. Dispersibility in chloroform and dichloromethane will be important for the preparation of magnetic field sensitive microspheres comprised of polymers such as poly(lactide)s via oil-in-water emulsion processes. Moreover, the coatings on the magnetite nanoparticles are comprised of a hydrophilic, biocompatible material that allows the particle to redisperse in biological fluids and may allow for their elimination from the body [16].

PEO block lengths ranging from 2000 – 15000 g/mol were investigated to determine the block necessary to form a stable dispersion with these triblock copolymer stabilizers. It was determined that steric stabilization was provided by all of the block lengths in the triblock polymers investigated. Steric stabilization is necessary to create repulsive forces to balance the magnetic attractive forces and the van der Waals attractive forces of the magnetic nanoparticles.

Theory described by Rosensweig's modified Hamaker equation, suggests that surfactant tails must be greater than 1 – 2 nm in length in solution to prevent agglomeration and hence a stable ferrofluid [3]. This expression considers the predicted repulsive forces by converting the flat surface model into an integrated expression for two neighboring spheres. A sufficiently long surfactant chain creates a potential energy barrier (~25 kT) that is an order of magnitude greater than the thermal energy associated with each nanoparticle so particle coalescence is minimized [3]. The theoretical end-to-end distance determined by the characteristic ratio of a terminally attached chain [147] can be calculated by Equation 3.1

$$C_n^{IF} = \frac{\left\langle r_0^2 \right\rangle}{n l^2}, \qquad (3.1)$$

where the characteristic ratio for an attached chain at the interface is $C_n^{IF} = 4/3\ C_n^F$, C_n^F is the characteristic ratio for a free chain (~4.0 for PEO), r_0^2 is the end-to-end distance, n is the number of bonds along the backbone and *l* is the bond length (0.148 nm for PEO) [50]. The calculation of the predicted end-to-end distance using the characteristic ratio is valid because the lowest M_n poly(ethylene oxide) tail block used is sufficiently long for valid application of Gaussian statistics [148]. Using this equation the end-to-end distance for a 2000 g/mol poly(ethylene oxide) block segment is ~3.21 nm. This calculation suggests that our shortest block length poly(ethylene oxide) block polymer stabilizer is well above the length necessary to stabilize a magnetic nanoparticle. The theoretical mean squared end-to-end distance for all of the PEO tail blocks investigated are shown in Table 3.3.

Table 3.3 Theoretical root-mean square end-to-end distance of PEO tail block segments of polymer stabilizers using the characteristic ratio for an attached chain at the interface.

M_n PEO block (g/mol)	Number of bonds (n)	$\langle r_0^2 \rangle^{1/2}$ (nm)
2000	129.3	3.9
5000	338.4	6.3
15000	1019.7	10.9

However, it is important to note that these calculations are for polymers where the substrate/particle attachment is at the terminus of the polymer chain. Theoretically, the end-to-end distance for polymer stabilizers attached by the central segments will be greater than these models predict, due to the reduced volume available for the chains [50]. Therefore, the location of carboxylic acids in the central segments may be ideal to minimize the block length necessary for colloidal stability. Thus, in theory the block length of the polymer tail block may be decreased and still create stable dispersions. The intended benefit would be an increase in wt. % magnetite relative to polymer stabilizer.

The polymer stabilizer comprised of 2000 g/mol PEO tail blocks and an average of 5 carboxylic acid units (2k-5-2k) may be ideal to achieve a greater magnetic response per gram sample. The titration value of this polymer suggests that it contains an average of ~3.9 carboxylic acid groups per chain, which is slightly lower than the target. Literature has suggested that the presence of carboxylates during magnetite formation can negatively affect the nucleation and crystal growth mechanisms. These interactions can lead to formation of nonmagnetic iron species. The nonmagnetic iron oxides can be detected by X-ray diffraction analysis of the crystalline structure.

The powder X-ray diffraction data of a polymer-coated magnetite displayed peak line positions and relative intensities consistent with magnetite crystalline structure (Figure 3.6). The X-ray spectra also display several peaks not associated with the crystalline structure of magnetite. These additional diffraction peaks were produced by the crystalline poly(ethylene oxide) based stabilizer (Figure 3.6, spectrum 2). Magnetite coated with all of the polymer stabilizer compositions investigated indicated the magnetite crystal structure. The XRD analyses also suggests the absence of other nonmagnetic crystalline iron oxide species; however XRD cannot be used to completely refute the presence of maghemite due to strong similarities in their diffraction patterns. Finally, it was important to note that the X-ray diffraction patterns confirmed that the ammonium chloride salt byproduct produced during magnetite formation was successfully removed via dialysis.

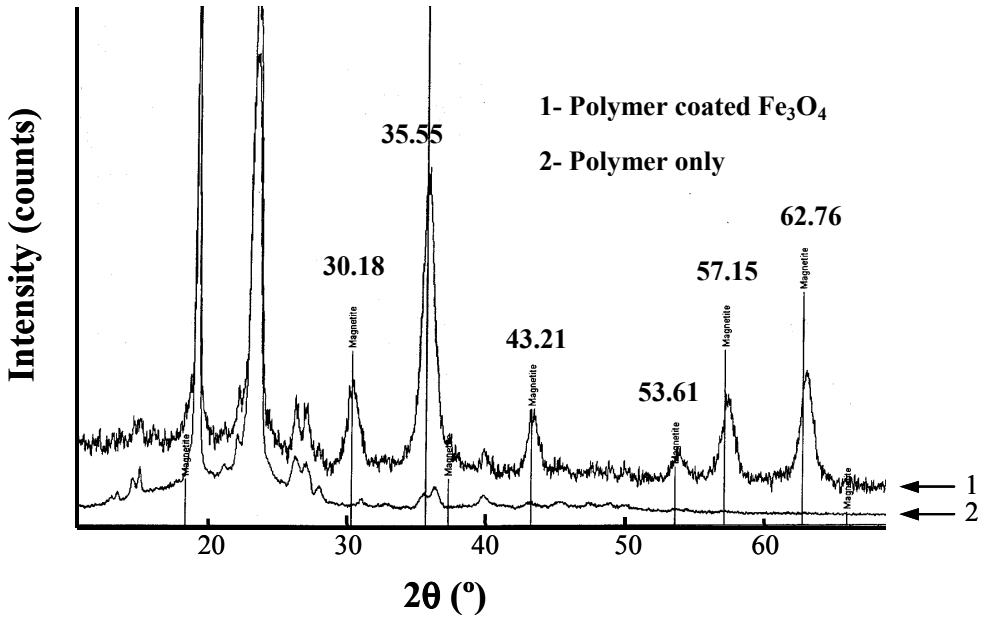

Figure 3. 6 Overlay of powder XRD patterns, where spectrum 1 = PEO-COOH-PEO coated Fe_3O_4 and spectrum 2 = neat polymer.

TEM micrographs of all aqueous dispersions show magnetite particles ~10 nm in diameter. The electron dense magnetite particles appear black and the polymer stabilizer is light gray in the micrographs (Figure 3.7). Magnetite nanoparticles coated with all of the polymer stabilizer compositions showed similar TEM micrograph dispersions in that no Fe_3O_4-Fe_3O_4 aggregation was observed. However, magnetite stabilized with the 5000 and 15000 g/mol PEO tail blocks appear to display slightly more clustering of the polymer coated magnetite particles (Figure 3.7b-c). However, elemental analysis determined that magnetite dispersions with 5000 and 15000 g/mol poly(ethylene oxide) containing polymer stabilizers contained less magnetite in terms of wt. % (Table 3.4).

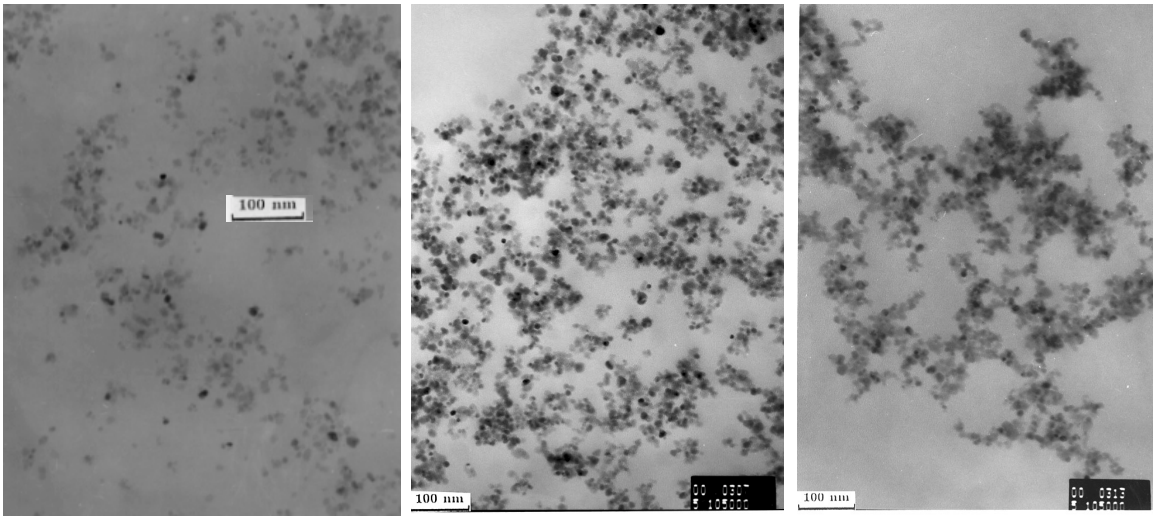

A) 2k-5-2k **B) 5k-5-5k** **C) 15k-3-15k**

Figure 3. 7 Transmission electron micrograph of some representative aqueous dispersions of PEO-COOH-PEO polymer stabilized magnetite nanoparticles cast onto a carbon grid.

The TEM samples preparation method currently employed to image magnetite dispersions may not be an appropriate for these materials because of the crystalline nature of the PEO-based polymer stabilizer. The polymer-coated magnetite nanoparticles reported in this paper are larger than polymer stabilized iron oxide systems previously reported. Magnetite formed by the method reported herein creates particles ~10 nm in diameter, while iron oxide particles formed in the presence of dextran and polyvinyl alcohol are 4.11 ± 0.85 nm and 5.78 ± 1.30 nm, respectively[75]. Moreover, the particles formed in the presence of dextran were clustered and necklace-like dispersion structures in PVA [75]. The small size of the particles may be due to the presence of the polymer during iron oxide formation. However, these polymers stabilizers do not contain functional groups and therefore may only superficially stabilize the nanoparticles.

Other carboxylic acids containing water dispersible polymer stabilizers previously reported are poly(ethylene oxide)-b-poly(methacrylic acid) (PEO-b-PMA) [81] and a modified poly(ethylene oxide) containing two terminal carboxylate groups (DCPEG) [80]. Both research groups reported the method of iron oxide formation by aqueous coprecipitation in the presence of the stabilizer. Magnetite nanoparticles prepared in the presence of PEO-b-PMA were ~5 nm in diameter, with 5 nm of surfactant stabilizer suggesting a hydrodynamic radii of 15 nm. The DCPEG polymer stabilizer reported by Tamaura *et al*. was a modified poly(ethylene oxide) containing two terminal carboxylate groups [80]. The researchers reported that magnetite was formed in the presence of a 50 wt. % solution of 2000 g/mol DCPEG. The large excess of DCPEG was used to promote coupling of the lipase through the amino groups of the enzyme and the carboxyl group of the polymer bound to the magnetite. Surprisingly, the size range of their particles was 30 – 70 nm, which appears aggregated in the TEM micrograph [80]. It is not clear

why such large magnetite particles were formed in the presence of the carboxylic acid containing polymer stabilizer. However, the large excess of polymer present clearly led to significant polymer agglomerations. These experimental observations suggest that an excess of carboxylate groups on the polymer stabilizers may be undesirable.

Additional the magnetite crystal structure characterization of the polymer stabilized magnetite nanoparticles was investigated by the high-resolution transmission electron microscopy (HRTEM). The electron diffraction pattern suggests that these magnetite nanoparticles are single crystalline materials (Figure 3.8). The experimental electron diffraction and the theoretical pattern (overlapped circles) contain many of the same spacings.

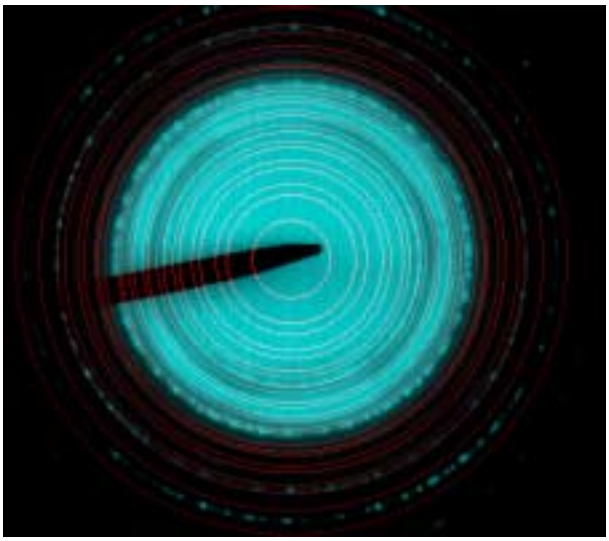

Figure 3. 8 Electron diffraction pattern of magnetite nanoparticles coated with polymer stabilizer containing 5000 g/mol PEO tail segments and ~ 3 carboxylic acid groups (5k-3-5k) via HRTEM.

The magnetic properties of these polymer stabilized magnetite nanoparticles were investigated by VSM analyses. The magnetic moments of these polymer-stabilized magnetite nanoparticles rapidly saturated in the presence of an externally applied magnetic field (up to 8000 Oe). The magnetization data were quantified in terms of magnetite using elemental analysis. The magnetization curve for magnetite nanoparticles stabilized with a polymer containing 2000 g/mol poly(ethylene oxide) tail segments and an average of ~3.9 carboxylic acid units in the central segments (2k-5-2k) is shown in Figure 3.9. The applied magnetic field was varied from 8000 Oe to – 8000 Oe. It is important to note that the magnetite nanoparticles do not display magnetic remanence and that the initial slope of the magnetization curve is relatively steep, indicating superparamagnetic behavior with a high magnetic susceptibility.

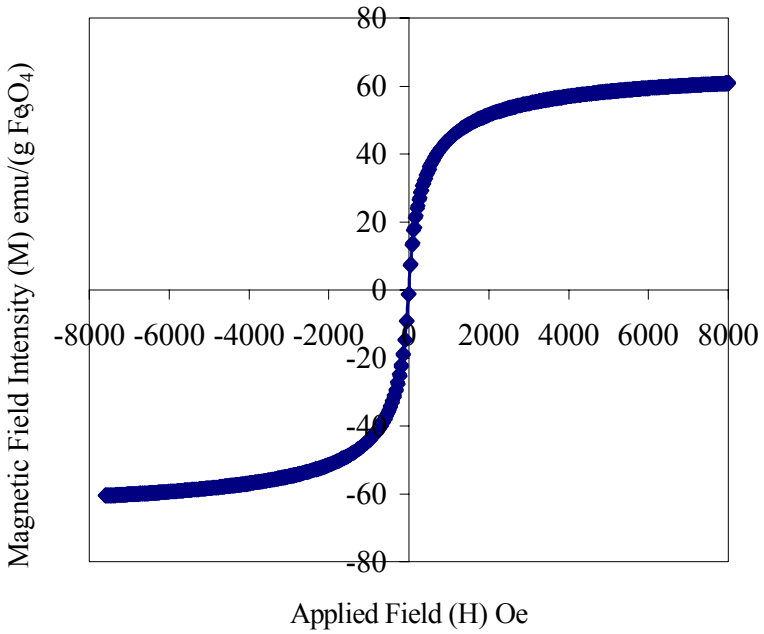

Figure 3. 9 Magnetization curve of a magnetite-triblock copolymer as a function of applied field (the stabilizing triblock polymer was comprised of 2000 g/mol PEO tail blocks and a central segment containing 5 carboxylic acid units).

Table 3. 4 Magnetic properties of nanomagnetite stabilized with poly(ethylene oxide) containing triblock stabilizers.

Polymer stabilizer	Concentration of magnetite predicted (wt. %)	Concentration of magnetite obtained (wt. %)	M_S/g sample (emu/g)	M_S/g Fe_3O_4 (emu/g)
2k-5-2k	35	23.0	17.0	73.7
5k-3-5k	46	30.2	20.1	66.4
5k-5-5k	30	22.8	18.0	78.8
5k-10-5k	30	7.8	9.4	69.9
15k-3-15k	18	6.9	4.6	66.7

The magnetic properties and the elemental analysis of all of the polymer-coated magnetite are shown in Table 3.4. Experimental values for the saturation magnetization of magnetite nanoparticles reported for similar sized iron oxide nanoparticles ranges from 30 – 60 emu/g, whereas bulk magnetite can theoretically be as high as is 92 emu/g [41, 42].

The magnetization values of 66 – 74 emu/g Fe_3O_4 (Table 3.4) are higher than values reported for similar iron oxide nanoparticle systems; however, these values are still lower than what bulk materials are capable of producing. As a comparison, PEO-b-PMA coated magnetite displayed a high saturation magnetization of ~60 emu/g Fe_3O_4, but a relatively low magnetic susceptibility of 0.02 [81]. The low magnetic susceptibility may be a result of the high concentration of carboxylic acids in the polymer stabilizer. One theory offered by Davies *et al*. suggests that particles containing sufficient concentrations of functional groups allows for spin-pinning of the iron oxide surfaces [137]. These results and others suggest that spin-pinning gives rise to a noncollinear spin structure, which is known to produce reduced magnetic properties [43, 137, 138]. These theorize may help explain the low magnetic susceptibility in magnetite nanoparticles

formed in the presence of poly(ethylene oxide)-b-poly(methacrylic acid) polymer stabilizers, which contain a significant concentration of functional groups.

The reduced magnetization of the nanoparticles compared to the bulk material properties has been investigated by several researchers using a variety of techniques. The theories and experimental interpretations of these studies are in conflict and remain debatable. Some studies suggest that reduction of the magnetic moment observed as the particle decreases depends largely on the crystalline magnetic anisotropy constant, K. The smaller the K value, the less relative magnetization the particle can display [41]. Experimental analyses including microscopy, XRD and magnetometry studies suggest that the reduced magnetization is due to surface characteristics of nanoparticles. Nevertheless, it seems that the effects of particle size in the nano length scales are complex and alter relaxation processes and interparticle interactions [42]. Therefore, values of 60 – 70 emu/g Fe_3O_4 may be approaching the theoretical and experimental magnetic moment limit for steric stabilized iron oxide nanoparticles.

The M_S in terms of sample weight is relatively low for the systems studied (~20 emu/g sample) and suggests that there is a significant amount of excess polymer in the samples. It will be necessary to eliminate the excess polymer to achieve higher M_S values per sample. The approach in future experiments will be to increase the wt. % magnetite relative to the polymer stabilizer until an experimental limit is determined while maintaining a stable dispersion.

3.4 Conclusions

Triblock polymers were successfully synthesized having controlled concentrations of carboxylic acid binding groups in central polyurethane segments and poly(ethylene oxide) end

blocks. These polymers were demonstrated to be hydrophilic steric stabilizers for magnetite nanoparticle dispersions in water and chlorinated solvents. It was important that the nanomagnetite particles were synthesized under strongly basic conditions prior to stabilization. After stabilization with the polymer, it was necessary to neutralize (pH 6.5 – 7) the mixtures to maintain stable dispersions. These aqueous dispersions were stable at physiological pH (7.4) and lower, suggesting that they will be stable in blood. The method developed to prepared stable magnetite dispersions may be generalized with by altering the chemical compositions of the sterically stabilizing polymer tail segments. Triblock copolymers containing controlled concentrations of carboxylic acid groups in the central urethane segments may be synthesized with a variety of different hydroxyl terminated polymer tail blocks, suggesting that this stabilization method could be generalized to serve diverse dispersion applications.

Transmission electron micrographs of stabilized magnetite showed nonaggregated Fe_3O_4 particles ~10 nm in diameter. The saturation magnetizations of these coated particles were 20 emu/g (30 wt. % Fe_3O_4), which corresponds to ~66.4 emu/g Fe_3O_4. This compares well with values reported by others for nanomagnetite [81]. It will be important to optimize these dispersions to obtain higher concentrations of magnetite to maximize their response.

Chapter 4: Polymer Stabilized Magnetite Nanoparticles Future Directions

4.1 Conclusions and suggested future work

Stable polymer coated magnetite dispersions were achieved with all of polymer stabilizers synthesized. These polymer-bound nanomagnetite particles form stable dispersions at neutral pH. Their ability to be dispersed in water and organic solvents may make them ideal for incorporation in to a biodegradable polymer microsphere matrix, such as poly(lactide), for utility as magnetic field sensitive drug delivery vehicles. Characterization including powder XRD and EDS was used to confirm the magnetite crystal structure. TEM photomicrographs indicate ~10 nm in diameter particles surface stabilized with polymer. Currently, these polymer coated magnetite nanoparticles are undergoing in vivo toxicity tests.

The saturation magnetization values we report (~66 – 78 emu/g Fe_3O_4) for the carboxylic acid containing poly(ethylene oxide) coated magnetite particles prepared appear to be near the limit possible for ~10 nm in diameter iron oxides. However, in terms of sample mass the saturation magnetization values are significantly lower (maximum ~20 emu/g sample), due to the presence of excess polymer. Synthetic and procedural modifications may help to increase the magnetic response per gram basis, which will be important for their incorporation into a biodegradable microsphere matrix for utility in magnetically guidable drug delivery vehicles. Modification of the current procedure for future investigations should include the study of higher magnetite loadings to a given concentration of triblock polymer stabilizer used. Also, excess polymer not bound to the magnetite may be removed during dialysis with a higher MWCO membrane, such as 14000 g/mol.

A synthetic approach to increase the magnetic response would be to consider the thickness of the organic sheath. It appears that the lowest molecular weight poly(ethylene oxide) tail block we investigated is still above the lower limit necessary to produce interparticle steric repulsive forces needed to prevent particle agglomeration. Therefore, synthesis of lower M_n monofunctional poly(ethylene oxide) oligomers will be important. These shorter block length poly(ethylene oxide) oligomers may be incorporated in triblock polymer stabilizers with controlled concentrations of carboxylic acids in the central urethane segments. Moreover, the critical number of carboxylic acids per chain necessary to bind to the surface of magnetite and form a stable dispersion should also investigated. In these studies, it may to useful to consider the ratio of the number of carboxylic acid groups per chain to the degree of polymerization of the poly(ethylene oxide) tail block.

4.2 Generalized stabilizer methods: Carboxylic acid containing triblock polymers

The success shown by the PEO-COOH-PEO triblock polymers in surface stabilizing magnetite nanoparticles suggests that the method may be generalized. The approach is a materials design of triblock polymer stabilizers comprised of carboxylic acid groups coupled to a variety of different monofunctional oligomeric tails having a hydroxyl group on its terminus. Future polymer stabilizers with triblock architectures containing controlled amounts of carboxylic acid groups in the central segments may be tailored for a variety of different applications based on the tail blocks chosen. One example currently being investigated by other researchers is the synthesis of a carboxylic acid containing hydrophobic triblock copolymer containing poly(propylene oxide) tail segments (Figure 4.1).

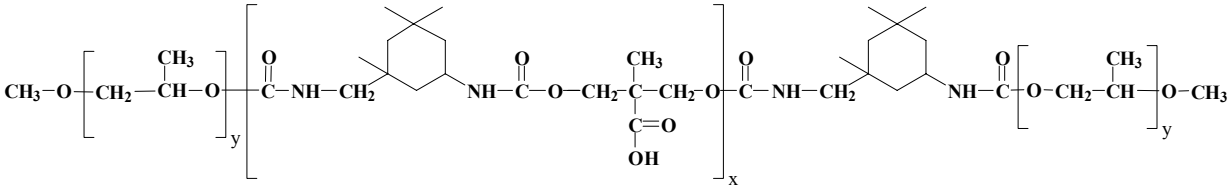

Figure 4. 1 Hydrophobic triblock polymer stabilizer containing carboxylic acid central segments and poly(propylene oxide) tail blocks.

The hydrophobic poly(propylene oxide)-based triblock polymer stabilizer was prepared to investigate the potential interfacial stabilization mechanism of the carboxylic acid to the magnetite nanoparticles. In addition, this liquid polymer stabilizer may provide insight into the quality of the coating on the magnetite surface. Previously, Section 3.3, it was proposed that the encapsulation of magnetite nanoparticles with the poly(ethylene oxide) based polymer stabilizer may not be properly visualized by TEM, due to it's crystalline nature.

The monofunctional poly(propylene oxide) oligomer (1600 g/mol, kindly donated by Bayer) used in this study was synthesized using coordination catalyst that allowed for low unsaturation and good hydroxyl functionalization. The poly(propylene oxide) based triblock copolymer (Figure 4.1) was synthesized by the same procedure described in Section 3.2.4 to contain three carboxylic acid groups per molecule. The concentration of the carboxylic acid groups were determined using quantitative ^{13}C NMR with $Cr(acac)_3$ relaxation agent in $CDCl_3$. The triblock copolymer synthesized contains ~2 carboxylic acid groups per chain (Figure 4.2).

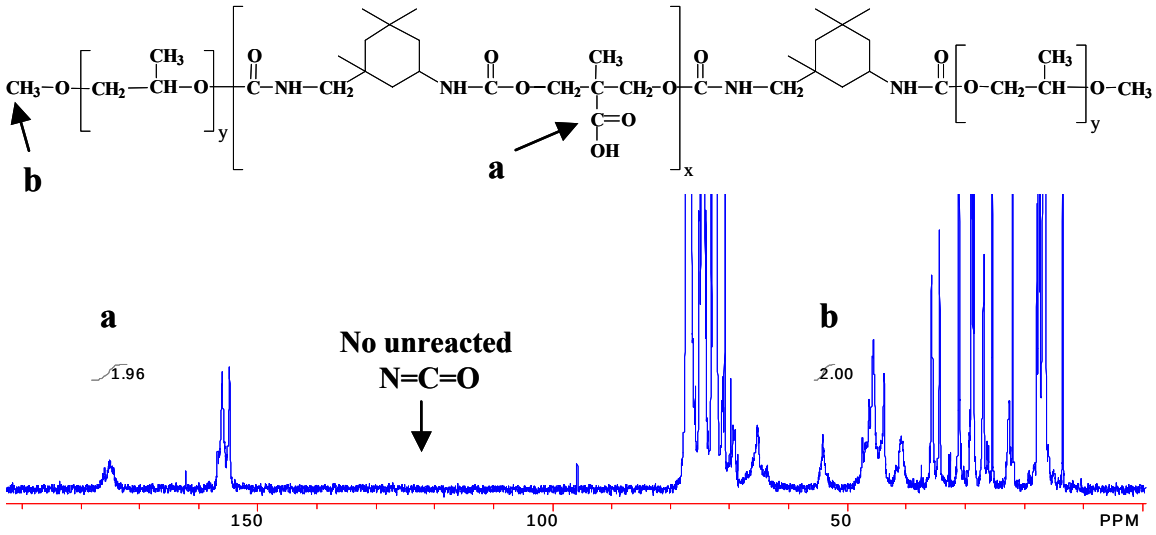

Figure 4. 2 ^{13}C NMR spectrum of PPO-COOH-PPO triblock polymer stabilizer containing ~2 carboxylic acid groups per chain.

Magnetite was prepared by the same procedure, using concentrations, described in Section 3.2.3 with the exception that the dichloromethane was not removed with a strong nitrogen purge. After magnetite formation and interfacial interaction with the polymer stabilizer in dichloromethane (water immiscible) were allowed to occur for ~1 hour. The mixture was neutralized and allowed to settle for ~8 hours. Upon settling the magnetite is extracted into the bottom organic phase. Currently, the dispersion's magnetic properties and magnetite content are being investigated.

4.3 Acknowledgements

The author would like to thank Prof. Phil Fraundorf and Sam Shuhan Lin for EDS analysis, and Frank May for powder XRD analysis (University of St. Louis). Funding for this researcher was graciously provided by Carilion Biomedical Institute, Orris C. and Beatrice Dewey Hirtzel Memorial Foundation and the DARPA-AFOSR Contract #F49620-01-1-0407.

List of Abbreviations I:

a	Lattice spacing
B	Magnetic Induction (gauss)
c	Major axis of a spheroid
D	diameter
H	Magnetic field strength (Oe)
H_C	Coercivity
k	Boltzmanns constant
K	Anisotropy constant
K	Kelvin
M	Magnetization (emu/g)
M_R	Remanence
M_S	Saturation magnetization
T_B	Blocking temperature
T_N	Néel temperature
U	Potential energy
κ	Magnetic susceptibility
μ	Magnetic moment
μ	Magnetic permeability
μ_o	Magnetic permeability of free space
ρ	Mass density (g/cm^3)
θ	Angle
τ	Timescale of measurement
PEO	Poly(ethylene oxide)
PPO	Poly(propylene oxide)
COOH	Carboxylate group
VSM	Vibrating sample magnetometer
FT-IR	Fourier transform infrared spectrometer
EA	Elemental Analysis
C_n^{IF}	Characteristic ratio of an attached chain
C_n^F	Characteristic ratio of a free chain
$\left\langle r_0^2 \right\rangle^{1/2}$	Mean square end-to-end distance
n	Number of bonds
l	Bond length
M_n	Number average molecular weight

References I:

[1] D. A. Thompson, J. S. Best, *IBM Journal of Research and Development* **2000**, *44*, 311.
[2] Z. Wang, J. S. Yin, S. A. Harfenist, R. L. Whetten, I. Vezmar, http://www.ieee.org/organizations/pubs/newsletters/leos/oct98/univ.htm, **1998**.
[3] R. E. Rosensweig, *Ferrohydrodynamics*, Cambridge University Press, Cambridge, **1985**.
[4] J. P. Phillips, C. Li, J. P. Dailey, J. S. Riffle, *Journal of Magnetism and Magnetic Materials* **1999**, *194*, 140.
[5] M. Rutnakornpituk, M. S. Thompson, L. A. Harris, K. E. Framer, A. R. Esker, J. S. Riffle, J. Connolly, T. G. St. Pierre, *Polymer* **2002**, *43*, 2337.
[6] R. S. Molday, D. MacKenzie, *Journal of Immunological Methods* **1982**, *52*, 353.
[7] S. Roath, *Journal of Magnetism and Magnetic Materials* **1993**, *122*, 329.
[8] A. Jordan, R. Scholz, P. Wust, H. Schirra, T. Schiestel, H. Schmidt, R. Felix, *Journal of Magnetism and Magnetic Materials* **1999**, *194*, 185.
[9] M. I. Papisov, A. Bogdanov Jr., B. Schaffer, N. Nossiff, T. Shen, R. Weissleder, T. J. Brady, *Journal of Magnetism and Magnetic Materials* **1993**, *122*, 383.
[10] D. K. Kim, Y. Zhang, W. Voit, K. V. Rao, M. Muhammed, *Journal of Magnetism and Magnetic Materials* **2001**, *225*, 30.
[11] D. K. Kim, Y. Zhang, J. Kehr, T. Klason, B. Bjelke, M. Muhammed, *Journal of Magnetism and Magnetic Materials* **2001**, *225*, 256.
[12] L. Babes, B. Denizot, G. Tanguy, J. J. Le Jeune, P. Jallet, *Journal of Colloid and Interface Science* **1999**, *212*, 474.
[13] K. Widder, G. Flouret, A. Senyei, *Journal of Pharmaceutical Sciences* **1979**, *68*, 79.
[14] P. K. Gupta, C. T. Hung, F. C. Lam, D. G. Perrier, *International Journal of Pharmaceutics* **1988**, *43*, 167.
[15] A. Ibrahim, P. Couvreur, M. Roland, P. Speiser, *Journal of Pharmaceutics and Pharmacology* **1982**, *35*, 59.
[16] A. C. Guyton, J. E. Hall, in *Textbook of Medical Physiology*, W.B. Saunders Company, Philadelphia, **1996**, pp. 315.
[17] A. Wooding, M. Kilner, D. B. Lambrick, *Journal of Colloid and Interface Science* **1991**, *144*, 236.
[18] K. Yasugi, Y. Nagasaki, M. Kato, K. Kataoka, *Journal of Controlled Release* **1999**, *62*, 89.
[19] A. Beiser, *Modern Technical Physics*, 2 ed., Cummings Publishing Company, Menlo Park, **1973**.
[20] C. Kittel, *Introduction to Solid State Physics*, Wiley, New York, **1976**.
[21] R. Nave, http://hyperphysics.phy-astr.gsu.edu/hbase/solids/magpr.html, **2001**.
[22] C. M. Sorensen, in *Nanoscale Materials in Chemistry* (Ed.: K. J. Klabunde), John Wiley and Sons, Inc., New York, **2001**, pp. 169.
[23] P. C. Scholten, *Journal of Magnetism and Magnetic Materials* **1995**, *149*, 57.
[24] C. Chen, *Magnetism and Metallurgy of Soft Magnetic Materials*, Dover Publications, Inc., New York, **1986**.
[25] S. R. Elliott, *The Physics and Chemistry of Solids*, John Wiley & Sons, New York, **1998**.
[26] R. S. Tebble, D. J. Craik, *Magnetic Materials*, Wiley-Interscience, London, **1969**.

[27] R. M. Cornell, U. Schertmann, *The Iron Oxides: Structure, Properties, Reactions, Occurrence and Uses*, VCH Publishers, Weinheim, **1996**.
[28] D. J. Dunlop, *Science* **1972**, *176*, 41.
[29] D. L. Leslie-Pelecky, R. D. Rieke, *Chemistry of Materials* **1996**, *8*, 1770.
[30] S. Wells, University of Wales (Wales), **1989**.
[31] J. Smit, H. P. J. Wijn, *Ferrites*, John Wiley & Sons, New York, **1959**.
[32] M. Ozaki, in *Fine Particles: Synthesis, Characterization, and Mechanisms of Growth, Vol. 92* (Ed.: T. Sugimoto), Marcel Dekker, Inc., New York, **2000**.
[33] E. P. Wohlfarth, *Journal of Magnetism and Magnetic Materials* **1983**, *39*, 39.
[34] C. P. Bean, J. D. Livingston, *Journal of Applied Physics* **1959**, *30*, 120S.
[35] C. Kittel, *Physical Reviews* **1946**, *70*, 965.
[36] E. Blum, A. Cebers, M. M. Maiorov, *Magnetic Fluids*, Walter de Gruyter, Berlin, **1997**.
[37] R. H. Kodama, A. E. Berkowitz, *Physical Review B* **1999**, *59*, 6321.
[38] R. H. Kodama, *Journal of Magnetism and Magnetic Materials* **1999**, *200*, 359.
[39] R. Kotitz, P. C. Fannin, L. Trahms, *Journal of Magnetism and Magnetic Materials* **1995**, *149*, 42.
[40] I. S. Jacobs, C. P. Bean, in *Magnetism, Vol. III* (Eds.: G. T. Rado, H. Suhl), Academic Press, New York, **1963**, pp. 271.
[41] T. Sato, T. Iijima, M. Sekin, N. Inagaki, *Journal of Magnetism and Magnetic Materials* **1987**, *65*, 252.
[42] J. Popplewell, L. Sakhnini, *Journal of Magnetism and Magnetic Materials* **1995**, *149*, 72.
[43] J. M. D. Coey, *Physical Review Letters* **1971**, *27*, 1140.
[44] A. E. Berkowitz, W. J. Schuele, P. J. Flanders, *Journal of Applied Physics* **1968**, *39*, 1261.
[45] M. P. Morales, M. Andres-Verges, S. Veintemillas-Verdaguer, M. I. Montero, C. J. Serna, *Journal of Magnetism and Magnetic Materials* **1999**, *203*, 146.
[46] P. Mollard, P. Germi, A. Rousset, *Physica B+C* **1977**, *86-88*, 1393.
[47] J. L. Dormann, E. Tronc, D. Fiorani, in *Advances in Chemical Physics Series, Vol. 98* (Eds.: I. Prigogine, S. A. Rice), John Wiley & Sons, New York, **1997**, pp. 283.
[48] V. E. Fertman, *Magnetic Fluids Guidebook: Properties and Applications*, Hemisphere Publishing Corporation, New York, **1990**.
[49] J. P. Jolivet, E. Tronc, C. Chaneac, *The European Physical Journal Applied Physics* **2000**, *10*, 167.
[50] W. B. Russel, D. A. Saville, W. R. Schowalter, *Colloidal Dispersions*, Cambridge University Press, Cambridge, **1989**.
[51] H. Huang, S. Yang, G. Gu, *Journal of Physical Chemistry B* **1998**, *102*, 3420.
[52] X. Sun, A. Gutierrez, M. J. Yacaman, X. Dong, S. Jin, *Materials Science & Engineering A* **2000**, *286*, 157.
[53] D. Zins, V. Cabuil, R. Massart, *Journal of Molecular Liquids* **1999**, *83*, 217.
[54] F. A. Tourinho, R. Franck, R. Massart, R. Perzynski, *Progress in Colloid Polymer Science* **1989**, *79*, 128.
[55] T. Sato, *IEEE Transactions on Magnetics* **1970**, *MAG-6*, 795.
[56] N. Moumen, M. P. Pileni, *Chemistry and Materials* **1996**, *8*, 1128.
[57] V. Pillai, D. O. Shah, *Journal of Magnetism and Magnetic Materials* **1996**, *163*, 243.

[58] X. Qui, *Chinese Journal of Chemistry* **2000**, *18*, 834.
[59] V. A. M. Brabers, in *Handbook of Magnetic Materials, Vol. 8* (Ed.: K. H. J. Buschow), Elsevier Science, **1995**, pp. 189.
[60] P. A. Cox, *Transition Metal Oxides*, Oxford University Press, Oxford, **1992**.
[61] R. M. Cornell, U. Schertmann, *Iron Oxides in the Laboratory; Preparation and Characterization.*, VCH, Weinheim, **1991**.
[62] P. S. Sidhu, R. J. Gilkes, A. M. Posner, *Journal of Inorganic and Nuclear Chemistry* **1978**, *40*, 429.
[63] E. Strable, J. W. M. Bulte, B. Moskowitz, K. Vivekanandan, M. Allen, T. Douglas, *Chemistry of Materials* **2001**, *13*, 2201.
[64] K. M. Lee, C. M. Sorensen, K. J. Klabunde, G. C. Hadjipanayis, *IEEE Transactions on Magnetics* **1992**, *28*, 3180.
[65] P. A. Dresco, V. S. Zaitsev, R. J. Gambino, B. Chu, *Langmuir* **1999**, *15*, 1945.
[66] C. J. O`Connor, C. Seip, C. Sangregorio, E. Carpenter, S. Li, G. Irvin, V. T. John, *Molecular Crystals and Liquid Cystals* **1999**, *335*, 423.
[67] J. A. Lopez-Perez, M. A. Lopez-Quintela, J. Mira, J. Rivas, *IEEE Transactions on Magnetics* **1997**, *33*, 4359.
[68] S. Santra, R. Tapec, N. Theodoropoulou, J. Dobson, A. Hebard, W. Tan, *Langmuir* **2001**, *17*.
[69] I. I. Yaacob, A. C. Nunes, A. Bose, *Journal of Colloid and Interface Science* **1995**, *171*, 73.
[70] F. C. Meldrum, B. R. Heywood, S. Mann, *Science* **1992**, *257*, 522.
[71] P. M. Harrison, P. Arosio, *Biochimica et Biophysica Acta* **1996**, *1275*, 161.
[72] K. K. W. Wong, T. Douglas, S. Gider, D. D. Awschalom, S. Mann, *Chemistry of Materials* **1998**, *10*, 279.
[73] C. Sangregorio, J. K. Wiemann, C. J. O`Connor, Z. Rosenzweig, *Journal of Applied Physics* **1999**, *85*, 5699.
[74] J. W. M. Bulte, M. de Cuyper, D. Despres, J. A. Frank, *Journal of Magnetism and Magnetic Materials* **1999**, *194*, 204.
[75] H. Pardoe, W. Chua-anusorn, T. G. St. Pierre, J. Dobson, *Journal of Magnetism and Magnetic Materials* **2001**, *225*, 41.
[76] J. Lee, T. Isobe, M. Senna, *Journal of Colloid and Interface Science* **1996**, *177*, 490.
[77] G. D. Mendenhall, Y. Geng, J. Hwang, *Journal of Colloid and Interface Science* **1996**, *184*, 519.
[78] X. B. Ding, Z. H. Sun, G. X. Wan, Y. Y. Jiang, *Reactive & Functional Polymers* **1998**, *38*, 11.
[79] I. Dumazet-Boonamour, P. Le Perchec, *Colloids and Surfaces A: Physicochemical and Engineering Aspects* **2000**, *173*, 61.
[80] Y. Tamaura, K. Takahasi, Y. Kodera, Y. Saito, Y. Inada, *Biotechnology Letters* **1986**, *8*, 877.
[81] K. Wormuth, *Journal of Colloid and Interface Science* **2001**, *241*, 366.
[82] W. C. Elmore, *Physical Reviews* **1938**, *54*, 309.
[83] J. Bacri, R. Perzynski, D. Salin, V. Cabuil, R. Massart, *Journal of Magnetism and Magnetic Materials* **1990**, *85*, 27.

[84] R. Massart, *IEEE Transactions on Magnetics* **1981**, *Mag-17*, 1247.
[85] L. Shen, P. Laibinis, T. A. Hatton, *Langmuir* **1999**, *15*, 447.
[86] N. M. Gribanov, E. E. Bibik, O. V. Buzunov, V. N. Naumov, *Journal of Magnetism and Magnetic Materials* **1990**, *85*, 7.
[87] K. T. Wu, P. C. Kuo, Y. D. Yao, E. H. Tsai, *IEEE Transactions on Magnetics* **2001**, *37*, 2651.
[88] S. S. Papell, O. C. Faber, in *NASA Technical Note, Vol. (NASA-TN-D-4676)*, **1968**, 25pp.
[89] T. Sugimoto, E. Matijevic, *Journal of Colloid and Interface Science* **1980**, *74*, 227.
[90] B. A. Gardineer, C. J. Sambucetti, *IBM Technical Disclosure Bulletin* **1974**, *17*, 1820.
[91] M. Blesa, E. Matijevic, *Advances in Colloid and Interface Science* **1989**, *29*, 173.
[92] M. Gobe, K. Kon-No, K. Kandori, A. Kitahara, *Journal of Colloid and Interface Science* **1983**, *93*, 293.
[93] L. Liz, M. A. Lopez-Quintela, J. Mira, J. Rivas, *Journal of Materials Science* **1994**, *29*, 3797.
[94] D. P. E. Dickson, S. A. Walton, S. Mann, K. Wong, *NanoStructured Materials* **1997**, *9*, 595.
[95] M. De Cuyper, M. Joniau, *Langmuir* **1991**, *7*, 647.
[96] K. Kandori, M. Fukuoka, T. Ishikawa, *Journal of Materials Science* **1991**, *26*, 3313.
[97] G. S. R. Krishnamurti, P. M. Huang, *Clays and Clay Minerals* **1991**, *39*, 28.
[98] Y. Tamaura, K. Ito, T. Katsura, *Journal of the Chemical Society Dalton Transactions* **1983**, 189.
[99] K. J. Farley, D. A. Dzombak, F. M. M. Morel, *Journal of Colloid and Interface Science* **1985**, *106*, 226.
[100] S. E. Khalafalla, G. W. Reimers, *IEEE Transactions on Magnetics* **1980**, *Mag-16*, 178.
[101] R. L. Parfitt, R. S. C. Smart, *Soil Science of America Journal* **1978**, *42*, 48.
[102] P. M. Huang, M. K. Wang, in *Advances in Geoecology, Vol. 30* (Eds.: K. Auerswald, H. Stanjek, J. M. Bigham), International Development Centre, Ottawa, **1997**, pp. 241.
[103] Y. Sahoo, H. Pizem, T. Fried, D. Golodnitsky, L. Burstein, C. N. Sukenik, G. Markovich, *Langmuir* **2001**, *17*, 7907.
[104] N. Fauconnier, A. Bee, J. Roger, J. N. Pons, *Progress in Colloid Polymer Science* **1996**, *100*, 212.
[105] B. Denizot, G. Tanguy, F. Hindre, E. Rump, J. J. Le Jeune, P. Jallet, *Journal of Colloid and Interface Science* **1999**, *209*, 66.
[106] J. Israelachvili, *Intermolecular and Surface Forces*, 2 ed., Academic Press, London, **1992**.
[107] A. E. Lesnikovich, T. M. Shunkevich, V. N. Naumenko, S. A. Vorobyova, M. W. Baykov, *Journal of Magnetism and Magnetic Materials* **1990**, *85*, 14.
[108] A. Grants, A. Irbitis, G. Kronkaln, M. M. Maiorov, *Journal of Magnetism and Magnetic Materials* **1990**, *85*, 129.
[109] T. Hyeon, S. S. Lee, J. Park, Y. Chung, H. B. Na, *Journal of the American Chemical Society* **2001**, *123*, 12798.
[110] J. Shimoiizaka, K. Nakatsuka, T. Fujita, A. Kounosu, *IEEE Transactions on Magnetics* **1980**, *MAG-16*, 368.

[111] L. Shen, A. Stachowiak, K. F. Seif-Eddeen, P. E. Laibinis, T. A. Hatton, *Langmuir* **2001**, *17*, 288.
[112] A. Kondo, H. Kamura, K. Higashitani, *Applied Microbiology and Biotechnology* **1994**, *41*, 99.
[113] L. Shen, A. Stachowiak, T. A. Hatton, P. E. Laibinis, *Langmuir* **2000**, *16*, 9907.
[114] E. V. Groman, L. Josephson, J. M. Lewis,,, US, **1989**.
[115] T. Yoshimoto, T. Mihama, K. Takahasi, Y. Saito, Y. Tamaura, Y. Inada, *Biochemical and Biophysical Research Communications* **1987**, *145*, 908.
[116] R. S. Underhill, G. Liu, *Chemistry and Materials* **2000**, *12*, 2082.
[117] M. Breulmann, H. Colfen, H. Hentze, M. Antonietti, D. Walsh, S. Mann, *Advanced Materials* **1998**, *10*, 237.
[118] R. F. Ziolo, E. P. Giannelis, B. A. Weinstein, M. P. O'Horo, B. N. Ganguly, V. Mehrotra, M. W. Russel, D. R. Huffman, *Science* **1992**, *257*, 219.
[119] M. Breulmann, S. A. Davis, S. Mann, H. Hentze, M. Antonietti, *Advanced Materials* **2000**, *12*, 502.
[120] V. S. Zaitsev, D. S. Filimonov, I. A. Presnyakov, R. J. Gambino, B. Chu, *Journal of Colloid and Interface Science* **1999**, *212*, 49.
[121] J. Lee, M. Senna, *Colloid and Polymer Science* **1995**, *273*, 76.
[122] J. L. Arias, V. Gallardo, S. A. Gomez-Lopera, R. C. Plaza, A. V. Delgado, *Journal of Controlled Release* **2001**, *77*, 309.
[123] U. Hafeli, W. Schütt, J. Teller, M. Zborowski, *Scientific and Clinical Applications of Magnetic Carriers*, Plenum Press, New York, **1997**.
[124] R. Arshady, *Radiolabeled and Magnetic Particles in Mecidine & Biology, Vol. 3*, Citrus Books, **2001**.
[125] U. Hafeli.
[126] F. Sauzedde, A. Elaissari, C. Pichot, *Colloid and Polymer Science* **1999**, *227*, 846.
[127] K. Furusawa, K. Nagashima, C. Anzai, *Colloid and Polymer Science* **1994**, *272*, 1104.
[128] M. A. Correa-Duarte, M. Giersig, N. A. Kotov, L. M. Liz-Marzan, *Langmuir* **1998**, *14*, 6430.
[129] A. P. Philipse, M. P. B. van Bruggen, C. Pathmamanoharan, *Langmuir* **1994**, *10*, 92.
[130] A. Bee, R. Massart, S. Neveu, *Journal of Magnetism and Magnetic Materials* **1995**, *149*, 6.
[131] C. Liu, P. M. Huang, *Soil Science of America Journal* **1999**, *63*, 65.
[132] H. Kodama, M. Schnitzer, *Geoderma* **1977**, *19*, 279.
[133] K. Kandori, Y. Kawashima, T. Ishikawa, *Journal of Colloid and Interface Science* **1992**, *125*, 284.
[134] R. Kaiser, G. Miskolczy, *Journal of Applied Physics* **1970**, *41*, 1064.
[135] A. E. Berkowitz, J. A. Lahut, C. E. Van Buren, *IEEE Transactions on Magnetics* **1980**, *16*, 184.
[136] Y. W. Du, H. X. Lu, Y. Q. Wang, T. X. Wang, *Journal of Magnetism and Magnetic Materials* **1983**, *31-34*, 896.
[137] K. J. Davies, S. Well, S. W. Charles, *Journal of Magnetism and Magnetic Materials* **1993**, *122*, 24.
[138] S. Morup, *Journal of Magnetism and Magnetic Materials* **1983**, *39*, 45.

[139] C. Rocchiccioli-Deltcheff, R. Franck, V. Cabuil, R. Massart, *Journal of Chemical Research* **1987**, *5*, 126.
[140] S. A. Wolf, D. D. Awschalom, R. A. Buhrman, J. M. Daughton, S. von Molnar, M. L. Roukes, A. Y. Chtchelkanova, D. M. Treger, *Science* **2001**, *294*, 1488.
[141] Y. Inada, K. Takahasi, T. Yoshimoto, Y. Kodera, A. Matsushima, Y. Saito, *Trends in Biotechnology* **1988**, *6*, 131.
[142] Z. G. M. Lacava, R. B. Azevedo, E. V. Martins, L. M. Lacava, M. L. L. Freitas, V. A. P. Garcia, C. A. Rebula, A. P. C. Lemos, M. H. Sousa, F. A. Tourinho, M. F. Da Silva, P. C. Morais, *Journal of Magnetism and Magnetic Materials* **1999**, *201*, 431.
[143] A. Iannone, R. L. Magin, T. Walczack, M. Federico, H. M. Swartz, A. Tomasi, V. Vannini, *Magnetic Resonance in Medicine* **1991**, *22*, 435.
[144] E. Okon, D. Pouliquen, P. Okon, Z. V. Kovaleva, T. P. Stepanova, S. G. Lavit, B. N. Kudryavtsev, P. Jallet, *Laboratory Investigation* **1994**, *71*, 895.
[145] H. Otsuka, Y. Nagasaki, K. Kataoka, *Current Opinions in Colloid & Interface Science* **2001**, *6*, 3.
[146] J. M. Harris, *Poly(ethylene glycol) chemistry*, Plenum Press, New York, **1992**.
[147] D. H. Napper, *Polymeric Stabilization of Colloidal Dispersions*, Academic Press, London, **1983**.
[148] P. J. Flory, *Statistical Mechanics of Chain Molecules*, Oxford University Press, **1989**.

Chapter 5: Background to Rubber Modified Dimethacrylate Networks

5.1 Brief history of toughened thermosets

Thermoset networks display high strength, thermal stability and good mechanical properties. However, these materials are inherently brittle and have a low resistance to crack initiation and growth [1]. Methods to toughen networks were first introduced by the pioneering efforts of McGarry *et al.* in the late 1960s [1]. These researchers improved the toughness of epoxy resins by the incorporation of liquid rubbers. In these methods the rubber modifier was miscible in the resin and phase separated upon cure to form dispersed rubber particles ~0.5 – 5 μm in diameter (Figure 5.1). The image shows the rubber phase in the dark, stained with osmium tetraoxide and the epoxy in the light. The improvements in toughness were attributed to the dispersed rubber phase acting as stress concentrators, dispersing and distributing the stress throughout the matrix.

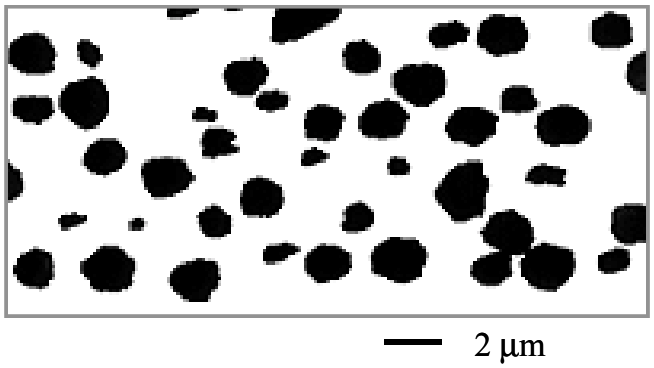

Figure 5. 1 Transmission electron microphotograph of rubber modified epoxy .

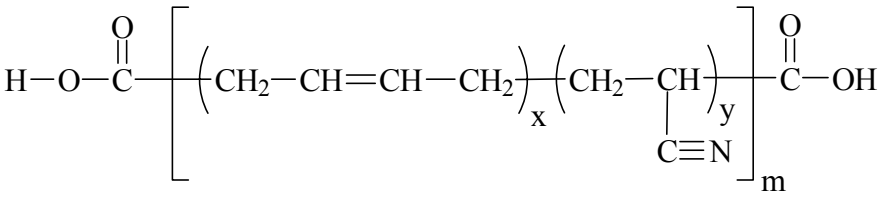

Figure 5. 2 Carboxyl terminated butadiene-acrylonitrile rubber copolymer, where typically m = 10 [1].

The rubber modifiers used in these toughening methods are typically carboxyl-terminated butadiene-acrylonitrile copolymers (CTBN) with M_n ~3500 g/mol (Figure 5.2) [1-3]. The disadvantage of these systems is that the rubber modifier is not chemically bound to the epoxy and therefore not solvent resistant and displays reduced performance at high temperatures [4].

McGrath and coworkers were among the first to introduce the use of reactive thermoplastic toughening to improve the toughness and maintain high temperature performance of the networks in the early 1980s [5]. One example is the reaction of an amine functionalized polyethersulfone with a diglycidyl ether of bisphenol-A (DGEBA) epoxy resin [5]. The reactive thermoplastic is miscible with the resin and then during cure the modifier copolymerizes into the network and simultaneously phase separates. The concentration of the reactive thermoplastic is an important factor. At low concentrations the epoxy was the major phase (Figure 5.3a). However, above 15 wt. % a phase inversion of the resin mixture occurs during copolymerization.

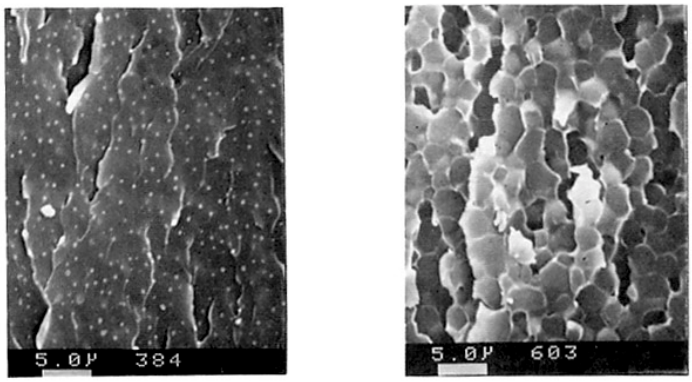

Figure 5. 3 Rubber modification of epoxy resins with a reactive polysulfone, where a) shows an epoxy continuous phase containing 10 wt. % thermoplastic and b) shows a phase inversion were the polysulfone (25 wt. %) is the continuous phase [5].

Phase inversion is a conversion of the homogeneous mixture of two or more components into a two phase system where the minor phase forms the continuous phase and essentially encapsulates the segregated major phase (Figure 5.3b). The researchers determined that this morphology leads to significant increases in fracture toughness and chemical resistance, due to the covalent bonds between the two components [4].

Kinloch notes that there are several factors that govern the toughening of thermosetting resins including the chemistry and microstructural features of the rubbery phase [6]. The chemistry of the rubber toughener should be such that it is compatible with the resin. Several elements of the microstructure of the dispersed rubber phase govern the toughening achieved and include: volume fraction, particle diameter, particle size distribution, interfacial adhesion of particle/matrix, morphology of dispersed phase and T_g of dispersed phase [6]. Literature reports extensive investigations of the rubber toughening of epoxy resins via condensation cures. What

is less well known is the rubber toughening of free radically cured networks such as vinyl ester resins.

5.2 Rubber modified vinyl ester resins

Epoxy acrylate-based resins are commonly known as vinyl ester or dimethacrylate resins. In terms of free radically cured networks, vinyl esters display better chemical resistance and are more cost effective than unsaturated polyesters resins [7]. Interestingly, researchers found that rubber toughening miscible with the DGEBA based epoxy resins such as reactive vinyl terminated acroylonitrile butadiene toughener (VTBN) [8, 9], epoxy terminated acrylonitrile butadiene (ETBN) [8] and CTBN [10] have poor initial compatibility with styrene diluted DGEBA based vinyl esters resins. Attempts to improve the compatibility of liquid rubbers such as VTBN and ETBN with the vinyl ester oligomers using surfactants also failed [8].

However, the compatibility of these rubber modifiers was enhanced by synthetically incorporating CTBN along the backbone of the vinyl ester oligomer (Derakane 8084) [11]. The fracture toughness of these modified networks increases slightly, but the networks are still relatively brittle. The presence of the pendent carboxyl terminated acrylonitrile butadiene chemically bound to the vinyl ester backbone increases the compatibility of rubber modifiers which does lead to improvements in fracture toughness. The critical stress intensity factor (K_{1C}) and the strain energy release rate (G_{1C}) values are shown in Table 5.1 for several vinyl ester resins [11].

Table 5. 1 Fracture toughness values of some vinyl ester materials [11].

Material	K_{1C} ($MN/m^{1/2}$)	G_{1C} (J/m^2)
A) Derakane 411-45 (45 wt. % styrene)	0.72	157
B) A + modified polybutadiene	2.22	1948
C) Derakane 8084	1.15	432
D) C + VTBN	1.71	1234
E) C + caprolactone modified RLP	2.97	2940

[B]polybutadiene end-capped with low molecular weight polyurethane
[D]vinyl terminated butadiene acrylonitrile copolymer (VTBN)
[E]caprolactone oligomer-terminated acrylonitrile copolymer

Despite some initial incompatibility, the use of various liquid acrylonitrile-butadiene copolymer rubber modifiers in vinyl ester compositions has been studied by several researchers [8, 9, 12-14].

The vinyl ester resins commonly reported are unmodified vinyl ester resin (VE 411-45, DOW Chemical Co.) and CTBN elastomer modified vinyl ester (VE 8084, DOW Chemical Co.). The unmodified VE and the CTBN elastomer modified VE commercial materials contain 45 wt. % and 40 – 50 wt. % styrene, respectively. The liquid rubbers added to improve the fracture toughness may also contain an additional 5 – 15 wt. % styrene [14].

Pearce *et al.* reported the toughening of unmodified VE and CTBN elastomer modified VE with addition of ETBN or VTBN rubber modifiers [14]. The samples were cured at 60 °C for 1 hour and then 120 °C for two hours. The unmodified vinyl ester cured with ETBN phase separated into large particles. However, when the ETBN was added to the CTBN elastomer modified VE the ETBN phase separated into small elastomeric particles, which significantly increased the fracture toughness of the network. The same increase in fracture toughness of CTBN elastomer modified VE resins with additions of ETBN liquid rubber cured at 80 °C for 1 hour and then for 2 hours at 120 °C was also reported by Seibert *et al.* [13]. Pearce *et al.* suggest

that the ETBN associates with the CTBN bound to the VE resin. In general, when cured at elevated temperatures the incorporation of ETBN or VTBN rubber modifiers added to the elastomeric CTBN vinyl ester resin produced significant increases in fracture toughness and adhesion [14]. However, samples comprised of VTBN rubber modified added to CTBN elastomer modified VE displayed a lower G_{1C} then the same resin containing ETBN rubber modifier when cured at 25 °C for 16 hours and then cured 90 °C for 90 minutes.

The rubber toughening produced by the addition of VTBN was also investigated by Liao *et al.* to DGEMA based vinyl ester resin cured at 90 °C for 4 hours [9]. The VTBN phase separated into 20 – 100 nm in diameter dispersed particles during the cure. The researchers state that only moderate increases in fracture toughness were due to low compatibility of the VTBN in the vinyl ester resin [9].

Ullett *et al.* investigated several liquid rubber modifiers including poly(butadiene-acrylonitrile) copolymers, poly(epichlorohydrin) and poly(acrylates) [12]. The poly(butadiene-acrylonitrile) copolymers include: CTBN, VTBN and ETBN. The poly(acrylates) were butyl acrylate and ethyl-hexyl acrylate based materials. The researchers determined that in general the networks with two phase morphology produced improvements in fracture toughness. They found that when the poly(butadiene-acrylonitrile) liquid rubber were added to unmodified VE resins and cured at elevated temperature they showed lower fracture toughness than when the specimens were cured at lower temperature. The CTBN elastomer modified VE resins were tougher than the unmodified VE resins independent of the type of liquid rubber added. The poly(epichlorohydrin) rubber modifier was the most effective of all the liquid rubbers. However, the extent of the toughening effectiveness was dependent on the cure temperature. The highest

temperature cure produced the largest increase in fracture toughness of the unmodified VE resins when poly(epichlorohydrin) was used as the modifier.

In general, these liquid rubbers improve the fracture toughness of vinyl ester resins. However, the disadvantage of the acrylonitrile-butadiene copolymer rubber modifiers is that they are inherently sensitive to ultraviolet light and thermoxidative degradation due to the double bonds in the butadiene repeat units.

Chapter 6: Rubber Modified Dimethacrylate Networks

6.1 Introduction

Polymer matrix fiber reinforced composites were first introduced to construction and infrastructure applications over half of a century ago. These materials have display a higher strength to weight ratio compared to conventional steel and concrete structures, with superior corrosion resistance and reduced construction time. In the past few decades there has been an increase in their utilization in infrastructure designs [15]. Currently, the cost of these materials has been a limitation to their implementation. However, it is projected that the cost will decrease as their demand increases. An upsurge in consumption has recently been predicted due to the aging and environmental deterioration of a large number of structures in the United States. Furthermore, 4-10 % of the all of the bridges in the United States are deemed structurally deficient and require immediate repair [16, 17] and an average of 150 to 200 bridges in the U.S. experience partial to complete collapse each year [18]. The significance of the problem has led scientists and engineers to investigate optimized matrix resins for fiber reinforced composites and improved structure designs. Moreover, one very important application may be for the design of load bearing adhesives. These adhesives are essential because conventional mechanical fasteners create a stress concentration that diminishes the strength and lifetime of polymeric composite structures [19, 20]. The research described herein begins to address the issues regarding adhesive design and their characterization. Properties desired in a structural civil adhesive includes: 1) low viscosities for *in situ* application at construction sites; 2) reduced volatile content to ensure worker safety; 3) sufficiently high T_g of the cured material to avoid creep under

environmental conditions; 4) moisture resistance; 5) good adhesion to substrates; and 6) cyclic deformation durability that meets the requirements necessary for structural applications.

Unsaturated polyesters and vinyl esters are two examples of polymer matrix resins widely used in construction and infrastructure applications [15]. Vinyl ester/styrene systems are one of the most promising classes of matrix resins for infrastructure because of their amenity for automated processing into composites combined with rapid free radical cure mechanisms. Vinyl ester resins are more appropriately known as dimethacrylate resins. The high viscosity of the dimethacrylate resins is commonly reduced by the addition of a reactive dilute such as styrene, in concentrations up to 45 % by weight. When crosslinked these materials have T_gs, which can approach 150°C, and display excellent moisture resistance and hydrolytic stability that make them good candidates for use civil infrastructure [15, 21, 22]. However, the cure reaction of such resins causes 6 – 8 wt. % shrinkage due to the rather high styrene content [22]. In an attempt to reduce internal stresses caused by the volume reduction, a series of rubber toughened vinyl ester networks have been investigated. These modified vinyl esters may be ideal for coatings, toughened matrix resins for fiber reinforced composites, bridge deck wear surface resins and structural adhesive applications. The reduced concentration of volatile monomer is also of interest since coatings and adhesives from these materials are often applied in the field. Literature has reported several different approaches to rubber toughen vinyl ester resins using liquid rubbers such as carboxyl-terminated butadiene-acrylonitrile (CTBN) [8, 12-14]; vinyl-terminated butadiene-acrylonitrile (VTBN) [8, 9, 12, 14]; epoxy-terminated butadiene-acrylonitrile [12, 14]; poly(epichlorohydrin) (HTE) [12]; poly(ethyl hexyl acrylate) (EHA) [12]; poly(butyl acrylate) (BA) [12]. However, the vinyl terminated acroylonitrile butadiene (VTBN) [8], epoxy

terminated acrylonitrile butadiene (ETBN) [8] and carboxy terminated acrylonitrile (CTBN) [10] have poor initial compatibility with styrene diluted vinyl esters resins. In addition, work reported by Dreerman *et al*. state that attempts to improve the compatibility of VTBN and ETBN using surfactants also failed [8].

The materials described in this research are rubber-toughened dimethacrylate resins comprised of methacrylate functionalized poly(propylene oxide) and vinyl ester resins containing less styrene than normally used (Figure 6.1). These modified "vinyl ester" systems may be ideal for coatings, toughened matrix resins for fiber reinforced composites, bridge deck wear surface resins and structural adhesive applications, partially because lower styrene contents were possible, which alleviates environmental concerns with currents systems.

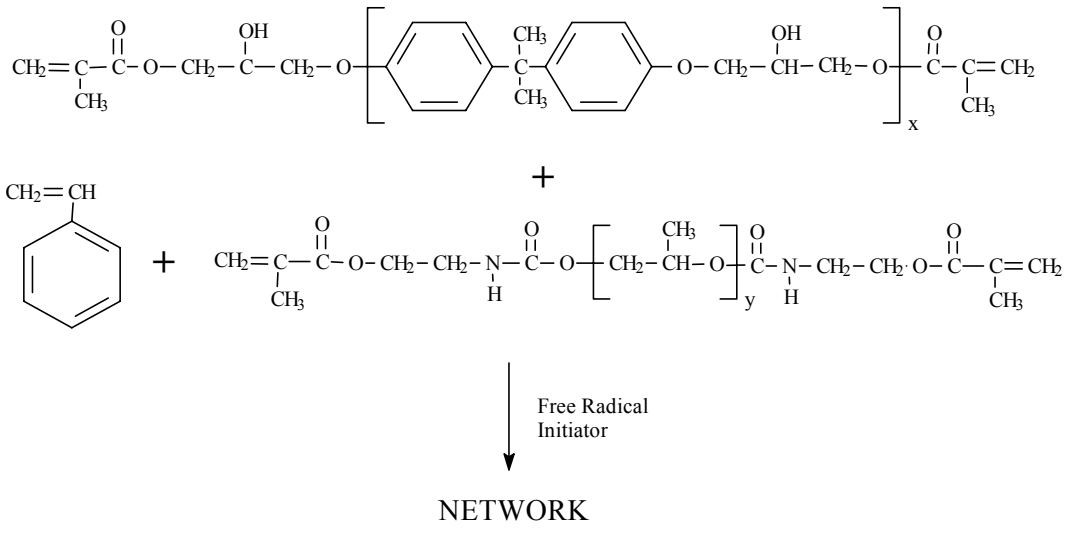

Figure 6. 1 Rubber modified dimethacrylate network formation with free radical initiator.

The concentration of styrene incorporated is reduced in the sense that our resins were prepared with 20 wt. % styrene, as opposed to the 35 – 60 wt. % often used in commercial vinyl esters. The methacrylate functionalized poly(propylene oxide) (mPPO), styrene (Sty) and vinyl ester (VE) resin composition mixtures (mPPO/Sty/VE) are miscible in their uncured states. Their network properties were investigated for potential application as structural adhesives.

6.2 Experimental

6.2.1 Materials

Dow Chemical kindly provided the 700 and 1000 g/mol vinyl ester resins. The 4200 g/mol poly(propylene oxide) was kindly donated by Bayer and was methacrylate terminated via urethane chemistry. The poly(propylene oxide) was dried under reduced pressure at 70 °C overnight prior to use. Isocyanatoethyl methacrylate (IEM, Aldrich) was fractionally distilled under reduced pressure at ~110 °C. Methyl ethyl ketone peroxide (MEKP) was kindly donated by Witco Corporation. Benzoyl peroxide (BPO), dimethylaniline (DMA) and styrene (Sty) were purchased from Aldrich Chemicals and used as received. Cobalt naphthenate was purchased from Alfa Aesar and used as received.

Modified poly(propylene oxide) synthesis. The 4200 g/mol poly(propylene oxide) was endcapped with isocyanatoethyl methacrylate to provide methacrylate reactive groups. Dried poly(propylene oxide) was reacted with isocyanatoethyl methacrylate (IEM) in a 1:2 mole ratio (stoichiometric equivalents) and 500 ppm dibutyltin dilaurate (DBTL) catalyst. The reaction mixture was purged with dry air and allowed to react at 40 °C with stirring. The reaction was

monitored by observing the disappearance of the isocyanate peak at 2260 cm^{-1} via Fourier transform infrared spectroscopy (FT-IR). Upon completion, hydroquinone (100 ppm) was added to the mPPO prior to refrigerated storage, under N_2.

Resin Preparation and Network Formation. A series of resin mixtures were prepared with the 700 and 1000 g/mol oligomers (Table 6.1). These resins were mixed with a mechanical stirrer at 40 – 45 °C until transparent miscible blends were obtained. The homogeneously mixed resins were degassed under mild vacuum at 35 – 40 °C prior to network formation to remove oxygen.

Table 6. 1 Chemical composition of series of resin mixtures.

Polymer Compositions (wt. %)
20% styrene:20% m4200 PPO:60% VE(700 g/mol)
20% styrene:20% m4200 PPO:60% VE(1000 g/mol)

Two sets of curing conditions were explored: 1) room temperature for 16 hrs followed by a postcure at 100 °C for 1 hr and 2) 150 °C for 1 hr. The room temperature reactions were conducted using methyl ethyl ketone peroxide (MEKP) (0.0905 moles/mol vinyl) as the initiator combined with 0.002 moles cobalt naphthenate/mole vinyl and 8.5 x 10^{-4} moles dimethylaniline/mole vinyl as accelerators. The mixtures were cured at 25°C for 16 hrs and then postcured at 100 °C for 1 hr (Figure 6.2).

Component	Function	moles / mole vinyl group
Cobalt Naphthenate	Accelerator	0.029
Dimethylaniline	Accelerator	1.09×10^{-3}
Methyl Ethyl Ketone Peroxide	Free radical source	8.45×10^{-4}

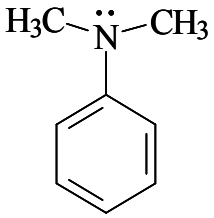

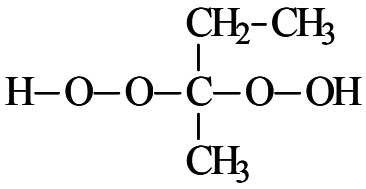

$$Co^{+2} + ROOH \rightarrow RO^{\bullet} + HO^{-} + Co^{+3}$$

$$Co^{+3} + ROOH \rightarrow ROO^{\bullet} + H^{+} + Co^{+2}$$

Figure 6. 2 Components for room temperature network formation using methyl ethyl ketone hydroperoxide (MEKP) with accelerators.

The reactions at higher temperatures were conducted with 9.31 x 10^{-3} moles benzoyl peroxide (BPO)/mole vinyl at 150 °C for 1 hr (Figure 6.3). Samples were then cooled to 25 °C in the oven with the door ajar to control their thermal history.

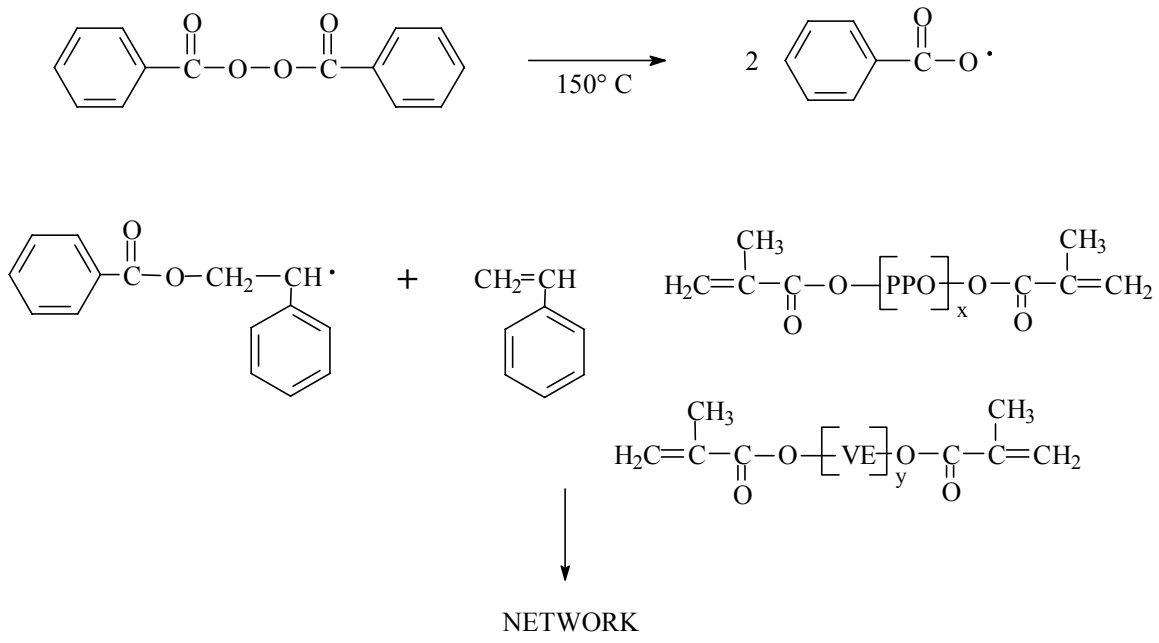

Figure 6. 3 High temperature cure of rubber modified dimethacrylates using benzoyl peroxide at 150 °C for 1 hour.

6.2.2 Methods

Complex viscosity. The complex viscosities of the resin mixtures and neat vinyl ester resin (without initiator) were measured using a Bohlin VOR Rheometer. The rheometer was run in oscillation mode at a frequency of 1 Hz. The parallel plate gap was set at ~1 mm and the temperature was ramped from 25 – 50 °C at 2.5 °C/minute.

FTIR. The methacrylate functionalized of poly(propylene oxide) oliogomers and network cures were studied using a Nicolet Impact Model 400 Fourier transform infrared spectrometer (FTIR). The melt reaction was investigated on salt plates and the cure studies were performed with a controlled demountable heat cell.

Swelling Experiments. Swelling measurements were carried out in dichloromethane (CH_2Cl_2) at room temperature. The dimensions of network specimens were small blocks (3 x 3 x 5 mm). Species were immersed in the CH_2Cl_2 for appropriately 3 weeks until swelling equilibrium was obtained. The swelling equilibria was determined by weighting the samples periodically until constant weights were observed. After equilibria was achieved, the specimens were weighed in the swollen state and then in the dried state, which was achieved by drying the specimens under reduced pressure at 150 °C for three days to a constant weight.

DMA. Network morphologies were investigated using a Perkin-Elmer DMA at 1 Hz with no controls applied in the 3-pt bend mode. The temperature range was –130 ° to 225 °C at 3 °C/minute with liquid N_2 as the coolant.

TEM. Imaging of the network morphologies was performed using a Philips 420T TEM run at 100kV. The samples were cryotomed on a Reichert-Jung Utracut-4E Ultramicrotome with a FC-4D cyroattachment at – 100 °C and imaged without staining.

Cloud Point. Cloud points of the resins were determined without initiator using an Olympus BX50 Optical Microscope with a photodiode array. A Linkam TMS 93 hot stage was used to ramp the temperature of the sample from 25 – 150 °C at 10 °C/minute.

SALS. Small-angle light scattering was investigating utilizing a He-Ne laser with a wavelength of 632.8 nm. The sample-to-film distance was 13.5 cm unless otherwise stated. The light scattering was investigated in V_v mode where the polarization direction of the incident beam is perpendicular to the analyzer using crossed polarized plates. Phase separation morphology was monitored at 55 °C as a function of time using a THM 600 Linkam hot stage.

K_{1C}. Plane-strain fracture toughness of the networks was investigated following ASTM 5045. Opaque networks were pre-cracked using a modification procedure to ASTM 5045 [23]. The K_{1C} analysis was performed on a 5500R Instron model 1123 instrument in the 3-pt bend mode with a 5,000 lb. load cell at a compression rate of 0.039″/minute.

FE-SEM. The surface of the fracture toughness samples were imaged using a LEO 1550 Field Emission scanning electron microscope (FE-SEM). Fracture toughness specimens were embedded in epoxy and gold sputter coated prior to imaging.

Lap Shear Strength. The average lap shear strength of the series was determined following ASTM D1002 & D3136 in triplicate. The lap shear analysis was performed on a 5500R Instron model 1123 instrument with a 5,000 lb. load cell at an extension rate of 0.05″/minute. The substrates investigated were aluminum (60-61), Derakane 411-350 (Dow Chemical) vinyl ester with E-glass fiber and weave composite, and steel (A36). Substrates were surface pre-treated prior to bonding. The Al (60-61) was cleaned and underwent a P-2 etch and the composite and steel substrates were grit blasted, sonicated, rinsed with acetone and oven dried at 115 °C for 15 minutes.

6.3 Results and discussion

Rubber modified dimethacrylate resins may be designed as structural adhesives for bonding fiber reinforced polymer composites to a variety of substrates. Several factor govern the properties of a structural adhesive that must be considered. The chemical composition of these materials is similar to that of the fiber reinforced composites that it is designed to bond. Poly(propylene oxide) may be ideal for these materials because of its relatively low viscosity, hydrolytic stability and miscibility with the bisphenol-A/epichlorohydrin based dimethacrylate oligomers. In contrast, other reactive toughener such as, vinyl terminated acroylonitrile butadiene (VTBN) [8], epoxy terminated acrylonitrile butadiene (ETBN) [8] and carboxy terminated acrylonitrile (CTBN) [10] have poor initial compatibility with styrene diluted vinyl esters resins. In addition, Dreerman *et al*. state that attempts to improve the compatibility of VTBN and ETBN using surfactants also failed [8]. The initial miscibility of the methacrylate

terminated poly(propylene oxide)'s with the styrene containing vinyl ester resin was thought to enhance and promote incorporation of the modifier into the network during cure.

The 4200 g/mol poly(propylene oxide), provided by Bayer, was prepared with a coordination catalyst that allowed for low unsaturation and good hydroxyl termination of the PPO. The methacrylate terminated poly(propylene oxide) was prepared with isocyanatoethyl methacrylate via urethane chemistry in the melt (Figure 6.4).

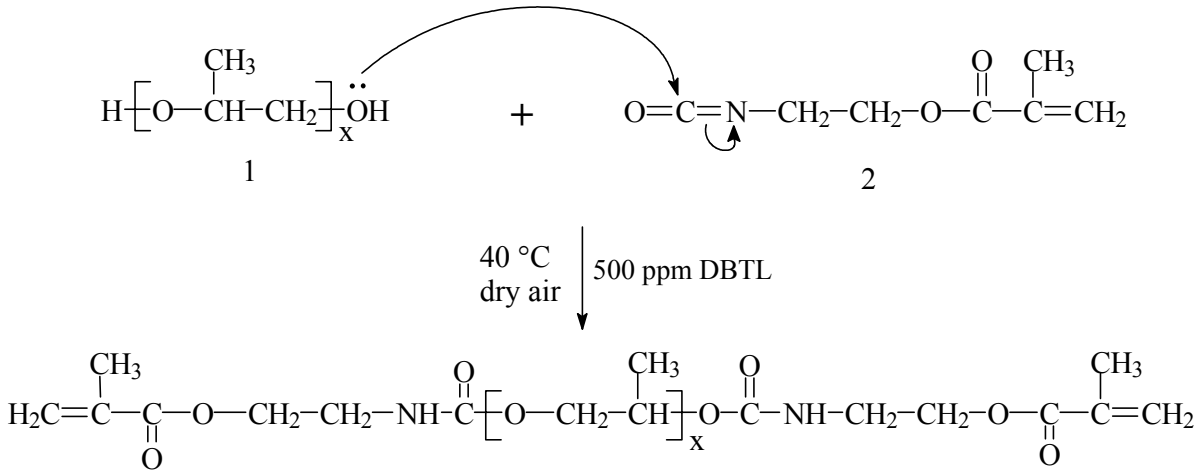

Figure 6. 4 Methacrylate termination of poly(propylene oxide) using isocyanatoethyl methacrylate in a melt reaction.

The reaction was performed in the melt to limit side reactions of the isocyanate. In this functionalization reaction it was important to add the poly(propylene oxide) slowly to the IEM to limit chain extension. A tin catalyst (dibutyl tin dilaurate) was used to promote hydroxyl attack to the carbonyl. The reaction completion was determined by observing the disappearance of the isocyanate peak using FT-IR at 2260 cm^{-1}.

The relatively low viscosity of the methacrylate terminated poly(propylene oxide) oligomer (mPPO) compared to the dimethacrylate resins (VE) allowed for compositions to be prepared with reduced styrene levels. Viscosity is a significant factor for a material designed as a structural adhesive for application and joint filling at a construction site. Commercial structural adhesives have viscosities of ~30 – 60 Pa-s at ambient temperatures. The complex viscosities of these rubber modified dimethacrylate resins were determined in a temperature range between 25 °C and 50 °C (Table 6.2).

Table 6. 2 Complex viscosities of resin mixtures at expected application temperatures.

Resin Composition (wt. %)	Complex Viscosity (Pa-s)		
	30°C	40°C	50°C
20% styrene/20% m4200 PPO/60% VE(700)	9.0	3.4	1.6
20% styrene/20% m4200 PPO/60% VE(1000)	125	64.2	44.4

The viscosity values ranged from ~10 to 120 Pa-s at 30 °C, depending on the resin composition, suggesting that these are all in a workable range. However, the slightly low viscosity displayed by the sty/mPPO/VE resins comprised of the 700 g/mol vinyl ester may need an additional filler to decrease any flow out of the joints. The 1000 g/mol vinyl ester oligomers without added styrene were too viscous to be prepared. Miscibility and the appropriate viscosity allows for a uniform distribution of the toughener throughout the styrene/vinyl ester resin. During the polymerization the methacrylate terminated poly(propylene oxide) chemically reacts with the vinyl ester and styrene via the methacrylate functional endgroups.

The crosslinking of the functional groups in the resins can be monitored by observing the disappearance of the styrene vinyl groups (943 cm^{-1}) and the methacrylate groups of the vinyl ester and the methacrylate terminated poly(propylene oxide) (910 cm^{-1}) via FT-IR. The extent of conversion was monitored in real-time for a resin mixture cured at room temperature cure followed by a postcure at 100 °C (Figure 6.5). The resin-containing initiator was placed in a heat cell and the room temperature cure was monitored as a function of time for 16 hours. After the 16 hour room temperature cure period the heat cell was ramped quickly to 100 °C and monitored for 1 hour. Peak heights of the methacrylate vinyl groups (out of plane bending of CH group) at 943 cm^{-1} and the styrene vinyl group (wagging of CH_2 group) at 910 cm^{-1} were normalized using the vinyl ester backbone peak at 830 cm^{-1} as an internal normalization peak. Earlier investigations have shown that the methacrylate double bond peak overlaps with a peak in the vinyl ester backbone in the 943 cm^{-1} region, which accounts for the residual peak adsorption [21, 22].

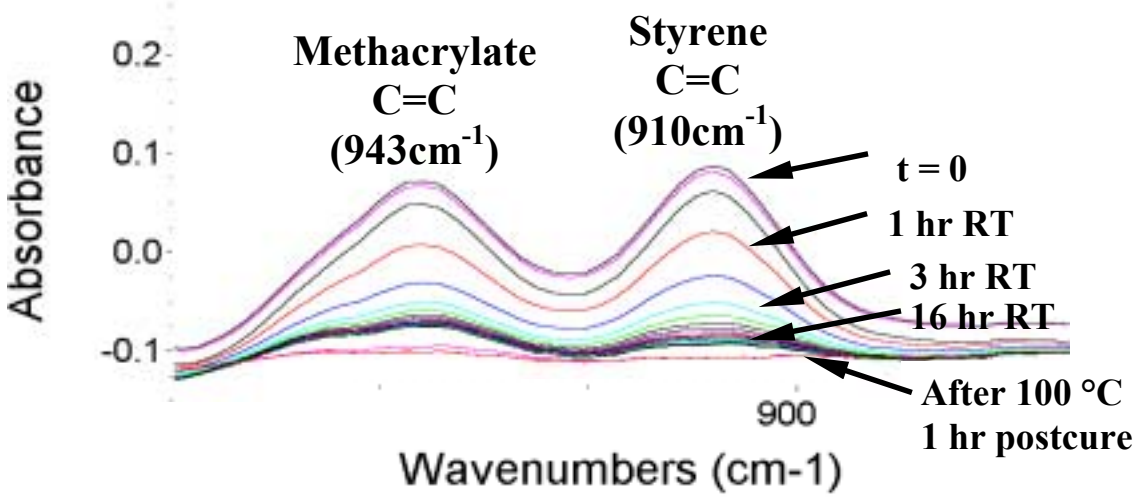

Figure 6. 5 Room temperature conversion monitored via FT-IR with a 100 °C postcure, observing the disappearance of the methacrylate and styrene double bonds at 943 and 910 cm^{-1}, respectively.

The backbone absorbance was removed by subtracting a fully cured system's FTIR spectrum from the normalized spectra. The fully cured network used in these corrections is a sample cured with BPO at 150 °C. It has been previously established using FTIR and solid-state ^{13}C NMR spectroscopy that these conditions lead to full cure [22]. Using this procedure, after 16 hours, the room temperature conversion of the methacrylate vinyl groups and styrene double bonds for a 20% styrene/20% m4200 PPO/60% VE(700) resin was determined to be approximately 71 and 88 %, respectively. When the sample is postcured at 100 °C for one hour the conversion proceeds to 92 and 98 %, for the methacrylate and styrene groups, respectively. These investigations suggest that the room temperature cure provides significant conversions.

The chemical resistance of the networks was investigated by swell experiments in dichloromethane at room temperature. The species (3 mm thick) were immersed in dichloromethane for two weeks and dried in a vacuum oven at 150 °C until constant weight. Dichloromethane was chosen as the swelling liquid because it is a solvent for all of the resin components. Therefore, any extractables will be accessed by the gel fraction values determined. Networks cured by two different cure methods were investigated in terms of swell indices (Equation 6.1) and gel fractions (Equation 6.2).

$$Swell\ index = \frac{volume\ of\ swollen\ gel}{volume\ of\ unswollen\ gel}$$

$$= 1 + \frac{[(W_{sw} - W_d)(1/\rho_s)]}{[W_d\,(1/\rho_g)]} \qquad (6.1)$$

q = 1.00 corresponds to no swelling

W_{SW} weight of gel in swollen state

W_d weight of gel in dry state

ρ_S density of solvent

ρ_g density of solvent

$$Gel\ fraction = \frac{weight\ of\ gel}{initial\ weight} \qquad (6.2)$$

Swell experiments were performed on the modified networks contain 20 % wt. styrene, 20 % wt. mPPO and 60 % wt. vinyl ester (700 or 1000 g/mol) oligomer cured by two different cure methods (Figure 6.6). In addition, an unmodified 700 g/mol vinyl ester network containing 20 % wt. styrene (sample 1) cured at room temperature, reported by Burts, was used as a comparison [24]. All of the networks containing the lower M_n vinyl ester resin (700 g/mol) exhibited relatively low swelling in dichloromethane. Also, the swelling of the unmodified vinyl ester (700 g/mol VE) network is comparable to the rubber modified networks containing the same M_n vinyl ester. The networks containing 1000 g/mol vinyl ester resin oligomers show higher swelling, which is assumed to be due to the lower crosslink density obtained with the higher M_n VE oligomer.

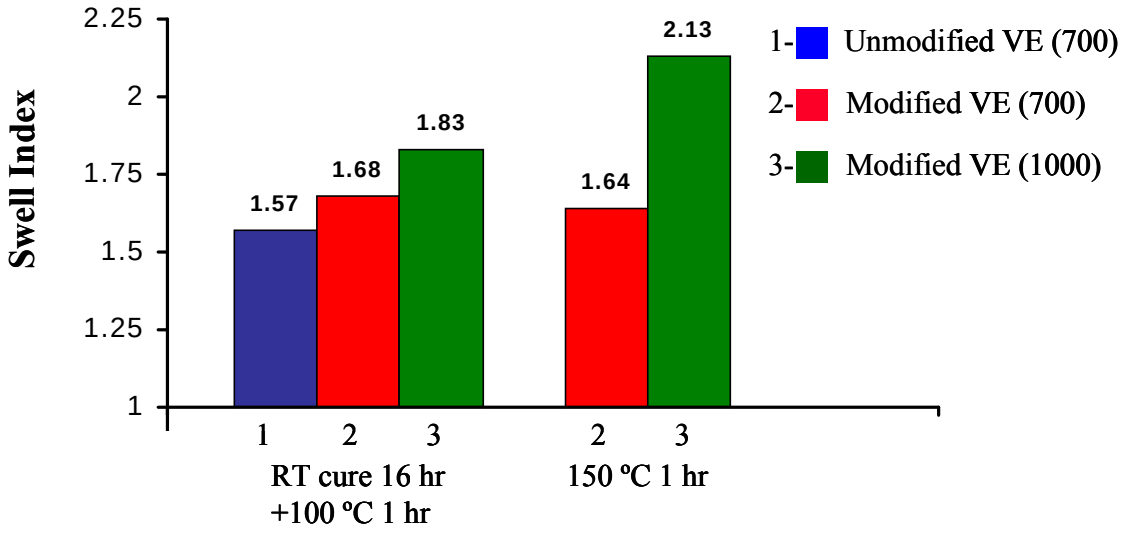

Figure 6. 6 Swelling index of an unmodified network and rubber modified networks. Modified networks are comprised of 20 % sty/ 20 % mPPO/ 60 % VE (700 or 1000 g/mol).

Table 6. 3 Gel fractions of rubber modified vinyl ester networks investigated by immersion in dichloromethane solvent.

Network composition	Cure method	% gel
20 % sty/ 20 % mPPO/ 60 % VE(700)	16 hr RT + 100 °C 1hr	93.4 ± 0.7
	150 °C	97.6 ± 0.3
20 % sty/ 20 % mPPO/ 60 % VE(1000)	16 hr RT + 100 °C 1hr	89.7 ± 2.8
	150 °C	97.5 ± 0.6

However, despite the extent of swelling observed, high gel fractions were observed for all of the rubber toughened networks in dichloromethane, which is a solvent for all resin components (Table 6.3). The FT-IR analysis and gel fraction analyses both indicate that the networks are significantly cured by either room temperature with a postcure or cured at elevated temperatures.

Interestingly, these rubber modified networks formed by two different cure methods produced networks with extremely different phase morphologies. When cured at 150 °C with BPO the once transparent mixtures turned opaque. However, room temperature reacted systems remained transparent after cure. DMA was used to determine the glass transition(s) to assess whether the networks had microphase separated during cure (Table 6.4).

Table 6. 4 T_g values determined by dynamic mechanical analysis for rubber modified vinyl ester resins cured by two different cure methods.

Network Compositions	tan delta (°C)		
	25 °C 16hr + 100 °C 1hr	150 °C 1hr	
20 % sty/ 20 % mPPO/ 60 % VE (700 g/mol)	96	-70	137
20 % sty/ 20 % mPPO/ 60 % VE (1000 g/mol)	87	-34	135

The DMA thermograms of the 25 °C cured materials followed by a postcure at 100 °C displayed only one distinct T_g at ~85 – 100 °C. It should be noted that the T_gs of these networks approached the postcure temperature (100 °C) where vitrification occurred. The thermogram curve of resins cured with BPO at 150 °C displayed two T_gs. The lower temperature T_g is associated with the mPPO component and a higher temperature T_g for the vinyl ester/styrene domain. Thus, from the thermal analysis it was apparent that the networks cured at high temperatures were multiphase materials. The methacrylated poly(propylene oxide) homopolymer displays a T_g at ~ - 70 °C. Phase separation observed in the thermally cured networks comprised of two components (mPPO and vinyl ester/styrene) is clearly observed in the network containing 700 g/mol VE oliogomer. The slightly elevated higher value of the lower temperature T_g of the rubber modified vinyl ester containing 1000 g/mol VE oliogomer suggests that the mPPO may be slightly more phase mixed than the 700 g/mol VE.

The phase morphology was imaged using transmission electron microscopy. TEM analysis confirmed phase separation of the networks cured with BPO at 150 °C (Figure 6.7 A & B). The dark regions of the TEM images correspond to the vinyl ester/styrene domains and the lighter areas represent the poly(propylene oxide) modifier. The interdomain spacing of these networks was 2 – 4 micrometers. By contrast, TEM analysis of networkds cured at ambient temperature with MEKP and a postcure at 100 °C for 1hr networks showed no significant structure (Figure 6.7 C & D).

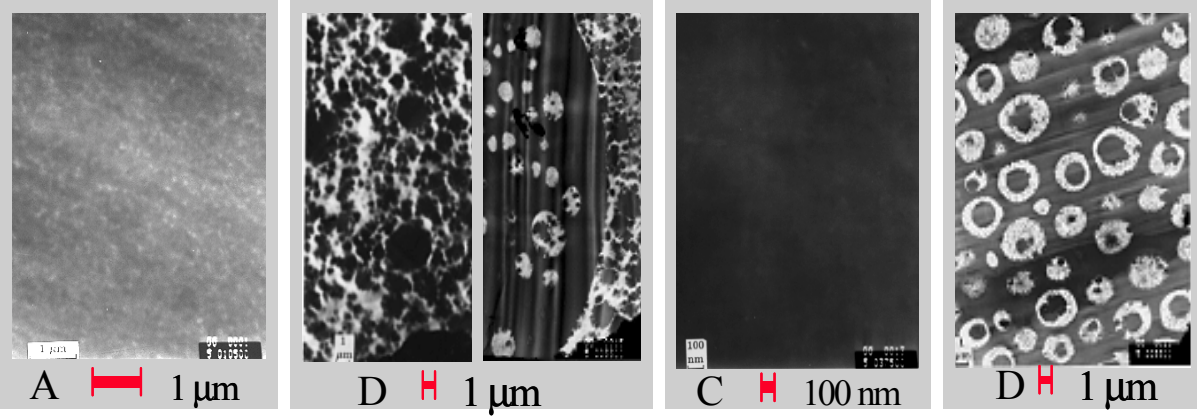

Figure 6. 7 TEM images of resins cured with MEKP at ~25°C for 12 hr followed by a postcure at 100°C for 1 hour (A & C) and resins cured with BPO at 150°C for 1 hour (B & D). The resin compositions all contain 20 wt. % styrene/20 wt. % m4200/ 60 wt. % VE(X) where X = 700 g/mol for A & B and X = 1000 g/mol for C & D.

The possibility of a LCST behavior was investigated by cloud point analysis. Thin films of the resins were studied on an optical microscope equipped with a hot stage. Phase separation was monitored during a temperature ramp by measuring the intensity of transmitted light. When the cloud point was reached a large decrease in transmitted light occurred. The phase separation of an adhesive resin was investigated as a function of temperature were the cure was inhibited by addition of 500 ppm hydroquinone. The resin mixture containing 20% styrene/20 % m4200 PPO/60% VE(1000) exhibited a cloud point at 60 °C (Figure 6.8).

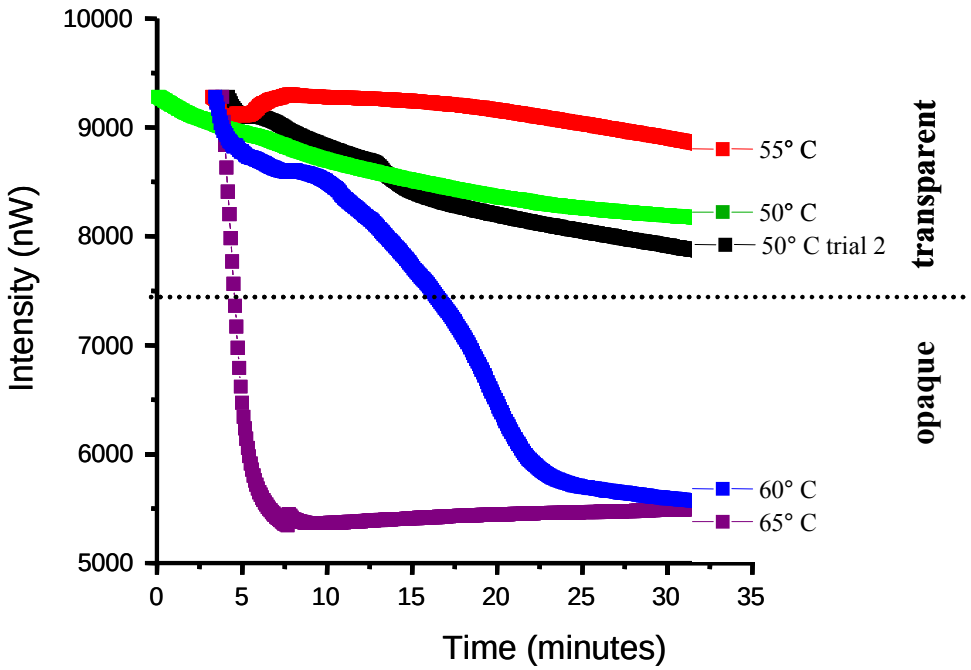

Figure 6. 8 Cloud point analysis of resin containing 20% styrene/20% m4200/ 60% VE(1000) without initiator as a function of time via optical microscopy. Cloud point was observed at 60 °C.

The cloud point of the same adhesive composition was investigated during crosslinking (containing BPO initiator) became turbid at 55 °C. These investigations suggest that the resin mixtures cured at 150 °C are phase separated prior to or during the very early stages of polymerization and lead to opaque microphase separated networks.

Additionally, phase separation was investigated using small angle light scattering (SALS). Light scattering was used to study the resin morphology as the transparent mixture proceeds from a single phase through phase separation to a two phase system at the LCST. The scattering study of a rubber modified 1000 g/mol VE resin was monitored as a function of time at 60 °C, which was the LCST for the resin (Figure 6.9). Crosslinking was prevented by the addition of ~500 ppm hydroquinone.

The SALS patterns shown in Figure 6.9 produce a maximum in scattering at distances that decrease with time. In general, small things scatter at larger angles, which indicates that the phase separation is increasing with time. The interdomain spacing was calculated using Braggs Equation (Equation 6.3) given by

$$d = \frac{\lambda / n}{2 \sin \frac{\theta}{2}} \tag{6.3}$$

where λ is the wavelength (632.8 nm), n is the refractive index (assumed to be 1.5) and θ can be determined using the arctan (B/sample-to-film distance). The interdomain distance of the resin was determined using Equation 6.3 and the scattering patterns produced by the resin held

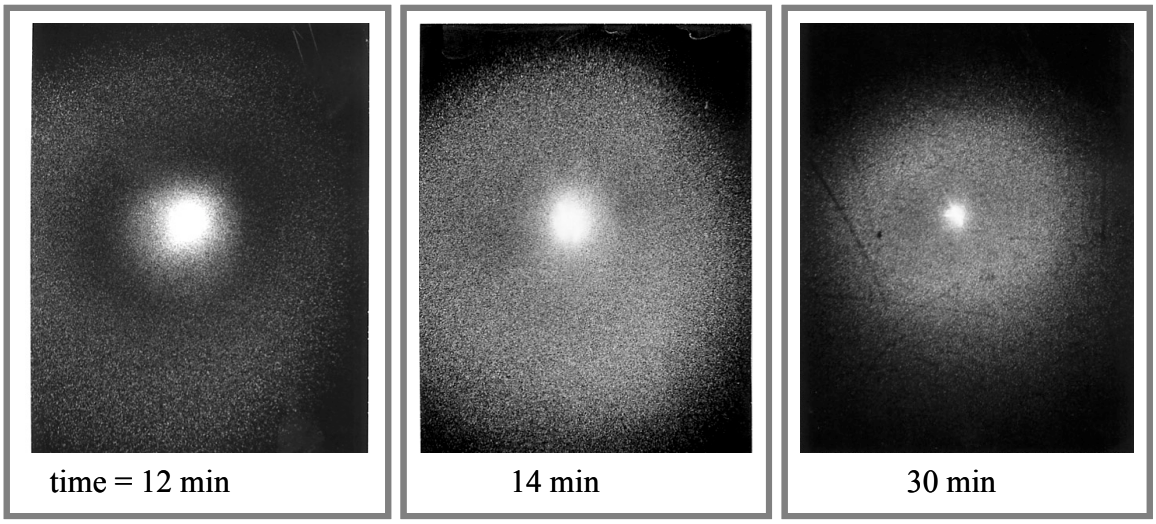

Figure 6. 9 Phase separation of a resin comprised of 20 wt. % styrene/20 wt. % m4200/ 60 wt. % VE(1000) and BPO at 55 °C as a function of time indicating spinodal decomposition (TEM Figure 6.7D).

isothermally at 55 °C. From this analysis the interdomain distance increased from ~1.7 μm at 12 minutes to 3.3 μm at 31 minutes. Phase separation of a polymer blend that occurs where the peak maximum appears at a finite distance and moves to smaller distances is indicative of spinodal decomposition.

The phase separation produced by crosslinking was also investigated. In this study a thin film of the same resin composition was cured at 150 °C for 1hour. The light scattering pattern obtained from this film indicated that interdomain spacing was ~4.2 μm. Thus, phase separation occurs at or above 60 °C independent of curing. When the resins were cured with BPO at 150 °C, the PPO rubber modifier phase separates either prior to, or very early, in the polymerization by spinodal decomposition. By contrast, the room temperature cured materials remain well

below the cloud point while the molecular weight builds. It is proposed that phase separation does not occur during the 100 °C postcure because the PPO is already locked into the network.

The multiphase morphology in these networks observed using TEM and SALS was expected to lead to improvements in fracture toughness by maximizing the energy dissipated throughout the sample under an applied stress by similar mechanisms as those seen in literature. McGrath *et al*. was among the first to introduce the use of reactive thermoplastic oliogomers to toughen networks in the 1980s [5]. The researchers found that epoxy containing sufficient concentrations of reactive thermoplastic modifier created a phase-inverted morphology where the covalently attached thermoplastic is the continuous phase. Furthermore, they state that these morphologies, produced by the presence and copolymerization of the reactive thermoplastics, display significant increases in fracture toughness. Since then, a variety of reactive thermoplastic oligomers have been reported to modify epoxies and other thermosetting resins [25-28].

The fracture toughness produced by the incorporation of methacrylate terminated poly(propylene oxide) to the styrene/dimethacrylate network compositions was investigated using a 3-point bend method (Figure 6.10).

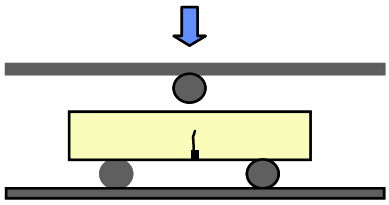

Figure 6. 10 Fracture toughness of networks determined by 3-point bend of prenotched specimens following ASTM 5045.

For each test specimen a load versus displacement curve was obtained. The toughness values were determined in terms of the plane strain critical stress intensity factor (K_{1C}). The K_{1C} values were calculated from the load causing crack propagation in each pre-notched sample using an Equation established on the basis of elastic stress analysis [29] (Equation 6.4)

$$K_{1c} = \frac{p}{BW^{3/2}} \frac{3(X)^{1/2}\,[1.99 - X(1-X)(2.15 - 3.93X + 2.7X^2)]}{2(1+2X)(1-X)^{3/2}} \qquad (6.4)$$

P is the load, B is the specimen thickness, W is the specimen width, a is the crack length and X = a/W. Networks cured at room temperature then postcured at 100 °C exhibited high fracture toughness (1.03 - 1.4 MPa-$m^{1/2}$) relative to the same resin compositions cured at elevated temperatures with BPO (Figure 6.3). The room temperature cured materials, which gave high K_{1C} values also had single phase morphologies. The low fracture toughness values of the elevated temperature cured networks are believed to be due to the phase separation of the PPO caused by the low cloud point. The lack of PPO incorporation into the styrene/vinyl ester domain makes the resulting networks flexible and weak.

Moreover, the room temperature cured, single phase materials containing mPPO rubber toughener also have significantly higher fracture toughness than an unmodified vinyl ester/styrene networks formed with similar viscosity and styrene content. However, the fracture toughness is similar to or slightly lower than butadiene-acrylonitrile based copolymer liquid rubber modified vinyl esters reported in literature [11]. Nonetheless, the observed relationship between phase morphology and fracture toughness suggests that optimal properties may be obtained by curing slightly below the cloud points of the resins.

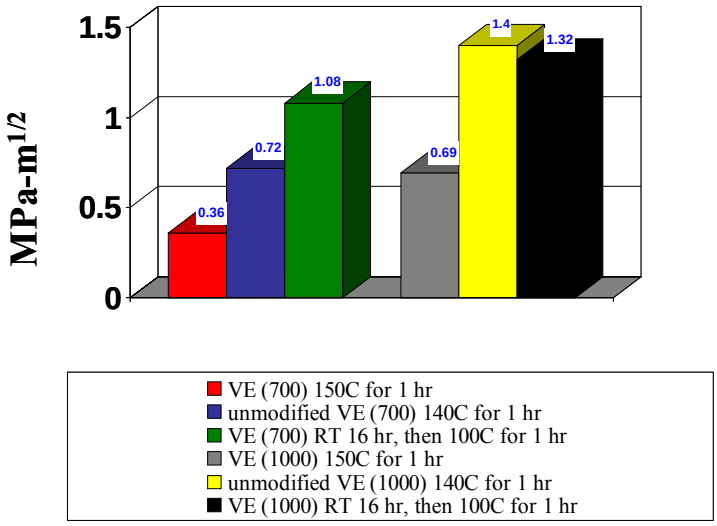

Figure 6. 11 Fracture toughness by three point bend test of rubber modified networks containing 20% styrene/20% m4200/ 60% VE(700 or 1000g/mol) and unmodified styrene/vinyl ester networks.

This approach may allow for incorporation of a large portion of the PPO into the network prior to phase separation.

The fracture surface created by the 3-point bend test was imaged using scanning electron microscopy (Figure 6.12). The fracture surface for the single phase room temperature cured sample suggests a tearing mechanism during fracture (Figure 6.12A). Whereas, the phase separated high temperature cured networks images help to suggest that the polymerization of the methacrylate groups of the poly(propylene oxide) rubber modifier are unable to react into the vinyl ester/styrene network. In fact, the cavitations observed compare well with the interdomain spacing determined by TEM and SALS studies. The phase separated regions create materials that are flexible and ductile, but not tough. The mechanism of toughening reported by McGrath

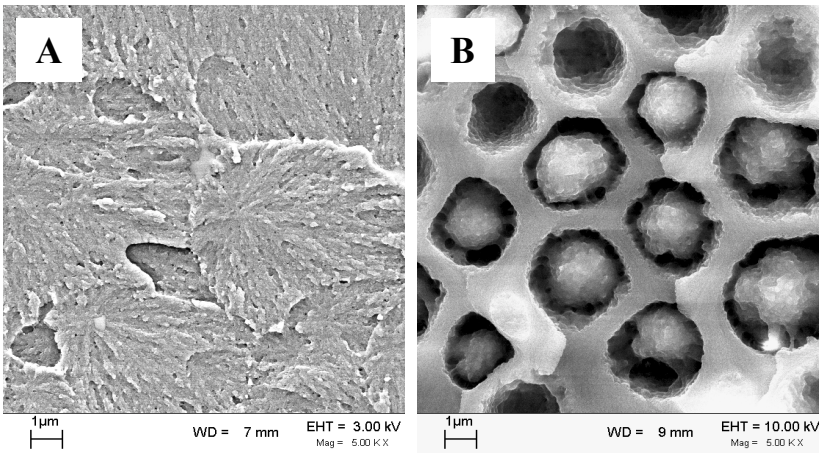

Figure 6. 12 SEM imaging the fracture surface of the 3 point bend samples tear mechanism of networks comprised of 20 %styrene/ 20 % m4200 PPO/ 60% VE (1000) cured at A) RT for 16 hr followed by 100 °C for 1 hr and B) 150 °C for 1 hour.

et al. obtained by a phase inversion is not observed in these networks due to what appears to be a distinct separation in the location of the polymerization of the methacrylated PPO and the styrene/dimethacrylate components above the mixtures LCST.

Adhesive strengths of the networks were investigated by single lap shear analysis. All of the adhesives contained 20 wt. % styrene, 20 wt. % mPPO (4200 g/mol), and 60 wt. % vinyl ester oligomer (700 or 1000 g/mol). The adhesives were bonded to aluminum-aluminum, steel-steel and vinyl ester-based composites and cured by the same cure methods previously described. The adhesives containing the 1000 g/mol vinyl ester oligomer cured with BPO at 150 °C exhibit structural strength on aluminum and composite substrates (3400 and 2600 psi, respectively) (Figure 6.13). In addition, the adhesives containing the lower M_n vinyl ester oligomer (700 g/mol) were reacted at room temperature following two different cure schedules: 1) room temperature cured for 1 week without a postcure, and 2) room temperature cured for 16 hours

followed by a postcure at 100 °C for one hour. Both cure schedules yielded adhesive bonds with similar strengths (~2000 psi) (Figure 6.13).

The low adhesives value of the 1000 g/mol VE cured at room temperature is a result of the high viscosity of that particular resin. This resin did not appear to wet the composite surface and resulted in interfacial failure. All other adhesives bonded to the vinyl ester/glass fiber weave composite substrates resulted in failure in the composite surface. These investigations help to suggest that the methacrylated poly(propylene oxide) modified styrene/vinyl ester resins display structural strength when cured at room temperature, with the appropriate viscosity. The relatively high fracture toughness of the room temperature cured networks may also enhance the performance of these materials as structural adhesives designed for polymer composite substrates.

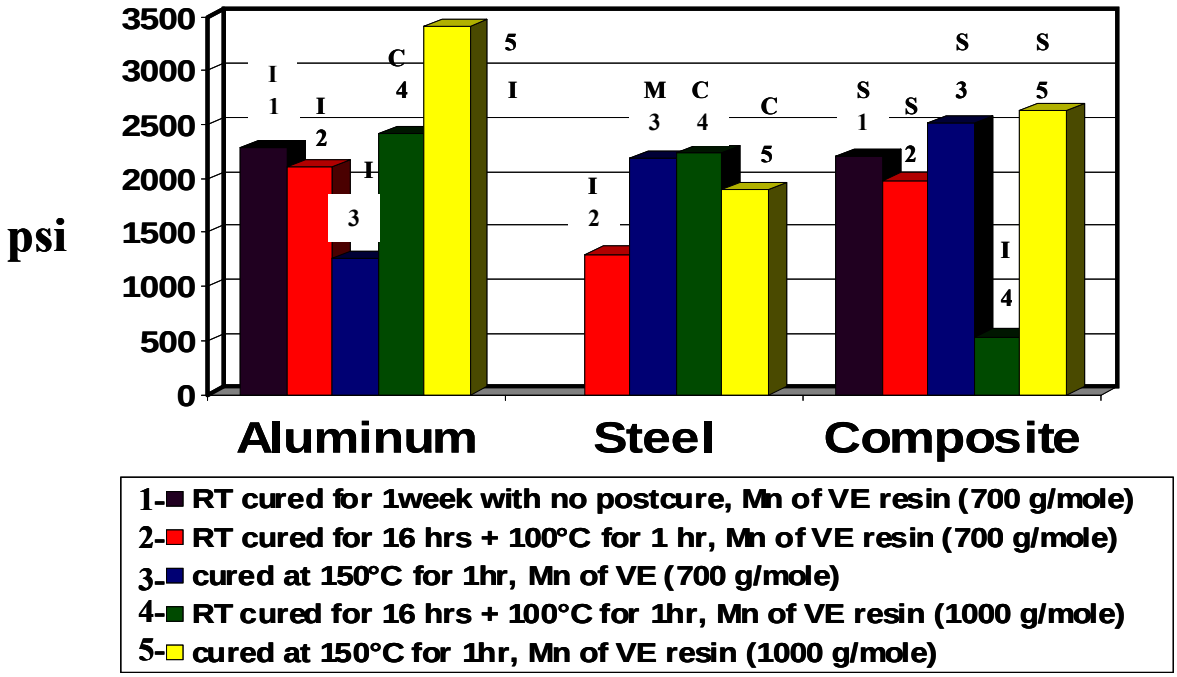

Figure 6. 13 Lap shear strength of 20% styrene/20% m4200/ 60% VE(700 or 1000g/mol) bonded aluminum-to-aluminum, steel-to-steel and composite-to-composite structures (I = interfacial failure, C = cohesive/adhesive failure, M = mixed mode failure and S = failure in the composite).

6.4 Conclusions

Cloud point analysis of the PPO modified resins confirmed LCST behavior, probably as a result of hydrogen bonding between the vinyl ester hydroxyl groups and the PPO ether oxygens. The room temperature cure conditions were well below the cloud points which allowed for good incorporation of the rubber toughener into the networks. Phase separation did not occur during the 100 °C postcure because the PPO was already locked into the networks. These rubber modified room temperature cured networks (followed by a postcure), were single phase and had high fracture toughness. By contrast, the resins cured above their cloud points phase separated prior to or early in the polymerization and hence the PPO modifier was not well incorporated into the vinyl ester/styrene. The spacing between the phase separated domains of the rubber toughened resin cured at 150 °C containing 1000 g/mol VE oligomer was calculated to be ~4.2 μm using Braggs Equation and the SALS pattern, which compared well to the TEM images of that network. The interdomain spacing increased as a function of time at constant temperature, indicative of spinodal decomposition. Unfortunately, these phase separated networks did not improve the fracture toughness. Instead these multiphase networks were flexible and had low fracture toughness.

Lap shear adhesive strengths of all of the adhesives, which had appropriate viscosities on composite substrates were in the structural regime (~2000 psi). Both room temperature cure schedules (with and without a postcure) resulted in good adhesive strength on the composite and aluminum substrates (~2200 psi). The fact that the adhesive resins cured solely at room temperature (without an elevated temperature postcure) showed similar adhesive strengths to

those finished at higher temperatures is significant. This is important to the potential use of such adhesives in the construction industry since they will be applied at the construction site.

In order to optimize the structure property relationships it may be necessary to cure these rubber modified networks at higher temperature, yet below the LCST of the resin compositions. Elevating the cure of the resins, while maintaining a single phase may further increase the fracture toughness performance of these systems. However, the FT-IR analysis and swelling experiments suggest that the room temperature cured networks that were postcured for 1 hour at 100 °C display significant conversion.

6.5 Acknowledgements

The authors would like to thank the National Science Foundation Science and Technology Center under contract number DMR-9120004 at Virginia Tech for funding, and Dow Chemical, Bayer and Witco Chemicals for materials.

List of Abbreviations II:

Instrumentation:

FT-IR	Fourier Transform Infrared Spectrometer
DMA	Dynamic Mechanical Analyzer
TEM	Transmission Electron Microscopy
FE-SEM	Finite Element Scanning Electron Microscopy
SALS	Small Angle Light Scattering

Materials:

MEKP	Methyle ethyl ketone hydroperoxide
DMA	Dimethylaniline
CoNap	Cobalt napththenate
BPO	Benzoyl peroxide
Sty	Styrene
mPPO	Methacrylated terminated poly(propylene oxide)
VE	Vinyl ester resin

Other Terminology Used

RT	Room temperature
T_g	Glass transition temperature
M_n	Number average molecular weight
LCST	Lower critical solution temperature
I	Lap shear interfacial failure
C	Lap shear cohesive/adhesive failure
M	Lap shear mixed mode failure
S	Lap shear failure in the composite surface veil

References II:

[1] A. J. Kinloch, *Structural Adhesives: Developments in resins and primers*, Elsevier Applied Science Publishers, New York, **1986**.

[2] F. J. McGary, A. M. Wilner, *Organic Coating and Plastic Chemistry* **1968**, *28*, 512.

[3] C. K. Riew, E. H. Rowe, A. R. Siebert, in *Advances in Chemistry Series, Vol. 154(Toughness and Brittleness Plast., Symp. 1974)*, **1976**, pp. 326.

[4] J. C. Hedrick, N. M. Patel, J. E. McGrath, in *ACS Advances in Chemistry Series No. 233: Toughened Plastics I: Science and Engineering* (Eds.: C. K. Riew, A. J. Kinloch), ACS, **1993**, pp. 293.

[5] T. H. Yoon, D. B. J. Priddy, G. D. Lyle, J. E. McGrath, *Macromolecular Symposium* **1995**, *98*, 673.

[6] A. J. Kinloch, *Polymer Materials Science and Engineering* **1987**, *57*, 311.

[7] R. E. Young, in *Unsaturated Polyester Technology* (Ed.: P. F. Bruins), Gordon & Breach, New York, **1976**, pp. 315.

[8] E. Dreerman, M. Narkis, A. Siegmann, R. Joseph, H. Dodiuk, A. T. Dibenedetto, *Journal of Applied Polymer Science* **1999**, *72*, 647.

[9] F. Liao, N. Chu, *Journal of Applied Polymer Science* **1988**, *35*, 797.

[10] J. S. Ullett, University of Dayton (Dayton), **1992**.

[11] P. Burchill, P. J. Pearce, in *Polymeric Materials Encyclopedia* (Ed.: J. C. Salamone), CRC Press, **1996**, pp. 2204.

[12] J. S. Ullett, R. P. Chartoff, *Polymer Engineering and Science* **1995**, *35*, 1086.

[13] A. R. Siebert, C. D. Guiley, A. J. Kinloch, M. Fernando, E. P. L. Heijnsbrock, in *Advances in Chemistry Series, Vol. 252(Toughened Plastics II)*, **1996**, pp. 151.

[14] P. J. Pearce, A. R. Siebert, D. R. Egan, C. D. Guiley, R. S. Drake, *Journal of Adhesion* **1995**, *49*, 245.

[15] J. S. Riffle, J. J. Lesko, P. M. Puckett, in *2nd International Conference on Composites in Infrastructure* (Eds.: H. Saadatmanesh, M. Ehsani), **1998**, pp. 23.

[16] B. Brailsford, S. M. Milkovich, D. W. Prine, J. M. Fildes,,, Northwestern University BIRL Project, **1995**, pp. 93.

[17] A. H. Zureick, B. Shih, E. Munley, *Structural Engineering Review* **1995**, *7*, 257.

[18] K. Dunker, B. Rabbat, *Scientific American* **1993**, *274*, 66.

[19] G. C. Mays, A. Hutchinson, *Adhesives in civil engineering*, Cambridge University, New York, **1992**.

[20] D. L. Hunston, J. L. Bitner, J. L. Rushford, J. Oroshnik, *Journal of Elastomers and Plastics* **1980**, *12*, 133.

[21] H. Li, E. Burts, K. Bears, Q. Ji, J. J. Lesko, D. A. Dillard, J. S. Riffle, P. M. Puckett, *Journal of Composite Materials* **2000**, *34*, 1512.

[22] H. Li, A. C. Rosario, S. V. Davis, T. Glass, T. V. Holland, R. M. Davis, J. S. Riffle, J. J. Lesko, J. Florio, *Journal of Advanced Materials* **1997**, *28*, 55.

[23] D. A. Dillard, P. R. McDaniels, J. A. Hinkley, *Journal of Material Science* **1993**, *12*, 1258.

[24] E. Burts, Dissertation, Virginia Tech (Blacksburg), **2000**.

[25] H. D. Stenzenberger, W. Roemer, P. M. Hergenrother, B. F. Jensen, W. Breitigam, *Advances in Materials: Challenge Next Decade* **1990**, *35*, 2175.
[26] A. J. Mackinnon, S. D. Jenkins, P. T. McGrail, R. A. Pethrick, *Polymer* **1993**, *34*, 3252.
[27] S. A. Srinivasan, J. E. McGrath, *Polymer* **1998**, *39*, 2415.
[28] T. H. Yoon, J. E. McGrath, *Journal of Applied Polymer Science* **2001**, *80*, 1504.
[29] ASTM Standard, *Annul Book of ASTM Standards* **1995**, *14.02*.

Vita

Linda A. Harris, daughter of Floyd and Carol Harris, was born on April 1, 1972 in Waupaca, Wisconsin. Linda is the third of four children. She grew up in Waupaca, a rural Midwest town in central Wisconsin. As an undergraduate she studied chemistry at the University of Wisconsin-Stevens Point (UW-SP). In the summer prior to her junior year she started an undergraduate research project in polymer chemistry under the advisement of Dr. John Droske. At the end of her junior year she was selected as a National Science Foundation (NSF) Summer Undergraduate Research Program (SURP) participant at Virginia Tech working with Dr. Judy Riffle. In 1996, Linda graduated *cum laude* from UW-SP with a Bachelor of Science in Chemistry (ACS certified) with a polymer emphasis and mathematics minor. After graduation she obtained a summer industry internship at the 3M Company in St. Paul, MN in the Adhesion division. Linda accepted an NSF fellowship to attend graduate school at Virginia Tech in 1997. In 2002 she graduated from Virginia Tech with a Ph. D. in Organic Polymer Chemistry. Linda successfully submitted a proposal to the NSF International Postdoctoral Research Fellowship Program to work in the biophysics department at the University of Western Australia in Perth. During her postdoctoral position she will be working with Dr. Tim St. Pierre (Dept. of Physics at UWA) and collaborating with Dr. Sue Berners-Price (Dept. of Chemistry at UWA), Dr. Jon Dobson (Dept. of Physics at Keele University, UK) and Dr. Judy Riffle (Dept. of Chemistry at Virginia Tech).

Linda A. Harris